TUDelft

Delft University of Technology

Recent advances in understanding the flow over bluff bodies with different geometries at moderate Reynolds numbers

Lekkala, Malakonda Reddy; Latheef, Mohamed; Jung, Jae Hwan; Coraddu, Andrea; Zhu, Hongjun; Srinil, Narakorn; Lee, Byung Hyuk; Kim, Do Kyun

Recent advances in understanding the flow over bluff bodies with different geometries at moderate Reynolds numbers

Malakonda Reddy Lekkala [a], Mohamed Latheef [a], Jae Hwan Jung [b], Andrea Coraddu [c], Hongjun Zhu [d], Narakorn Srinil [e], Byung-Hyuk Lee [f], Do Kyun Kim [g,h,1,*]

[a] Department of Civil and Environmental Engineering, Universiti Teknologi PETRONAS, Seri Iskandar, Perak, Malaysia
[b] Korea Research Institute of Ships and Ocean Engineering, Busan, South Korea
[c] Faculty of Mechanical, Maritime and Materials Engineering, Delft University of Technology, Mekelweg 2, Delft, 2628 CD, the Netherlands
[d] State Key Laboratory of Oil and Gas Reservoir Geology and Exploitation, Southwest Petroleum University, Chengdu, China
[e] Group of Marine, Offshore and Subsea Technology (MOST), School of Engineering, Newcastle University, Newcastle Upon Tyne, UK
[f] Advanded Research Center, Korea Shipbuilding & Offshore Engineering Co., Ltd., Ulsan, South Korea
[g] Department of Naval Architecture and Ocean Engineering, College of Engineering, Seoul National University, Seoul, South Korea
[h] Institute of Engineering Research & Research Institute of Marine Systems Engineering, Seoul National University, Seoul, South Korea

A R T I C L E   I N F O

A B S T R A C T

The application of unsteady incompressible flow phenomenon over the bluff bodies has received the attention of many researchers due to the rich and complex physics underpinning these flows, and thus requiring special attention in their modelling and numerical simulations. The wake that forms at the leeside of the bluff body is of particular interest. Reynolds number and geometry are in turn two prominent parameters that govern the formation and subsequent behaviour of this wake. This paper reviews the wake formations for different cylindrical bluff bodies cross-sections such as circular, elliptical, helically twisted elliptical, symmetric wavy, asymmetric wavy, and harbor seal vibrissae cylinders. Alongside the Reynolds number and geometrical shape, the impacts of rotational rate, aspect ratio, angle of attack, and gap ratio between the cylinder and the bottom wall on the hydrodynamic coefficients, Strouhal number, recirculation length and suppression of vortex shedding in the cylinder wake are investigated. In addition, the variation of hydrodynamic coefficients for different cylindrical shapes are compared. Finally, concluding remarks are drawn based on recent advances in understanding the flow features and predictions with CFD methods.

1. Introduction

Bluff bodies have been extensively investigated due to their common applications in different industries related to aerospace, civil, mechanical, and offshore engineering. These bluff bodies can be found either as a single or in a group that serves as structures for the designed purpose, such as offshore structures, heat-exchanger tubes, bridge cables, chimneys, etc. However, these structures are prone to flow-induced forces and vibrations in both air and water, which are adverse and may impact the life of the structure. Investigation regarding flow over bluff bodies can be traced back to classical works done by Karman (1911), Thom (1933), and Howarth (1935). Since then, many authors have researched the flow around bluff bodies. Majority of these can be found in the

detailed reviews by Zdravkovich (1981), Bearman (1984), Griffin and Hall (1991), Williamson (1996a), Schewe (2001), Sumner (2010), Bearman (2011), Wu et al. (2012), Bhattacharya and Gregory (2018), Derakhshandeh and Alam (2019), Wang et al. (2020) and Ma et al. (2022).

The main features of the typical flows over bluff bodies are provided in Fig. 1. The flow remains attached to the surface of the body when the Reynolds number (Re) is very low. However, when the velocity increases, the flow separates from the body, leading to the formation of vortex shedding or shear layer, which is a thin region of flow where the velocity gradient or shear exists). Typically, the boundary layer continues to be laminar from the upstream stagnation point to the point where it separates, resulting in the flow pattern as shown in Fig. 1. The
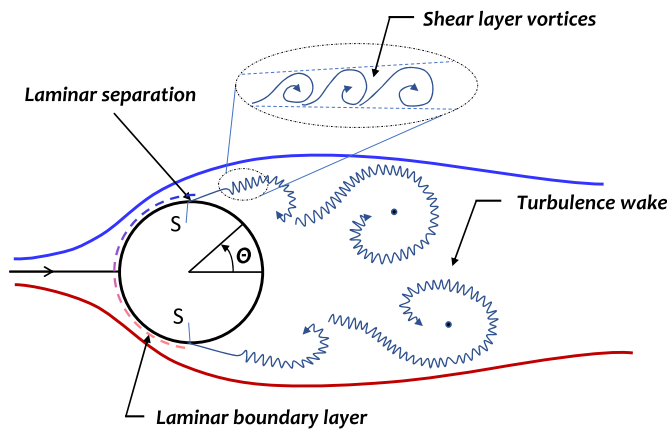
Fig. 1. Flow features behind the bluff body (Borgoltz et al., 2020).

separated flow from the body quickly becomes unstable and forms a wake downstream. These wakes roll up into vortices that shed from either side of the body anti-symmetrically at periodic intervals. This type of wake formation is known as 'Kármán Vortex Street' which is responsible for flow-induced vibrations (FIV) in many engineering problems. The main flow characteristics required for the detailed understanding of fluid dynamics over the cylinder includes:

(i) separation point of the fluid (the separation point is defined by the wall shear stress profile along with the flow, and the location along the surface where the wall shear stress becomes zero, which is regarded as the separation point. At this point, the local velocity gradient approaches zero. Beyond this point owing to the local flow reversal, the wall shear stress changes direction with the relatively low-pressure region behind the body is referred to as a wake. Flow separation over a body induces wakes behind bluff bodies. The interaction between these forward and reverse flows in the region generates fluid rotation or vortex structures. Depending upon Re and the shape of the body, the flow will have laminar or turbulent vortices),

(ii) boundary layer (the boundary layer is termed as the adjacent layer to the bluff body where the viscous effects are significant, and the fluid velocity gradually increases from zero at the boundary surface to the free stream velocity),

(iii) stagnation point (the stagnation point represents the fluid flow in the immediate neighbourhood of the cylinder where the local flow speed of the fluid is zero),

(iv) dynamics of the vortex patterns,

(v) wake formations, and

(vi) shedding frequency.

These characteristics are further governed by parameters such as the Reynolds number (*Re*),

$$\mathrm{Re} = \frac{\rho U D}{\mu} \tag{1}$$

where *U* is the flow velocity (m/s), *D* the diameter of the cylinder (m), ρ the fluid density (kg/m^3) and μ the dynamic viscosity of the fluid (Ns/m^2), turbulence level, surface roughness, etc.

The most common shapes of the cylindrical structures used in applications are categorised into three broad categories based on the cross-sectional form and surface curvature, as shown in Fig. 2. The three categories are (i) incessant and finite curvature (circular and elliptic cylinders); (ii) sharp edge curvature (rectangular, square, and triangular cylinders and flat plate etc.); and (iii) combination of earlier two types such as semi-circular cylinders. For type (i), the flow oscillates around the surface of a cylinder. The flow features are highly dependent on the surface roughness, Re, turbulence intensity, etc. For type (ii), the flow separation point around the cylinder is fixed and the flow characteristics of these cylinders are insensitive to Re, due to the fact that the separation point is already fixed at sharp edges (Bai and Alam, 2018). Therefore, the flow around circular cylinders has received a greater focus than any other cylinder. Numerous experimental and numerical analyses have been carried out to investigate the flow around circular cylinders in past decades, such as Cantwell and Coles (1983), Williamson and Roshko (1988), Chew et al. (1995), Norberg (2001), Owen et al. (2001), Norberg (2003), Lehmkuhl et al. (2013), Yeon et al. (2016), Law et al. (2017), Ahmed et al. (2020) and Janocha et al. (2022). At low *Re*, the flow around the cylinder is governed by viscous effects, and the force exerted on the body is mainly contributed by the skin friction. However, once *Re* exceeds the critical number (defined as *Re* at which the fluid flow changes from the laminar flow to the turbulent flow), it may result in a significant pressure drop downstream of the cylinder due to the vortex shedding in the cylinder wake. The vortex shedding occurs over a wide range of *Re* which may cause structural vibration, acoustic sound and resonance, and a substantial increase in drag and lift forces. Hence, the efficient control of vortex shedding is vital in engineering applications. In this study, the flow over smooth circular, elliptical, and cylinders developed based on the bio-mimetic principle are reviewed. It is suggested to refer to Xu et al. (2017) for flow features over the polygonal cylinder, Lysenko and Ertesvåg (2021) and Lysenko et al. (2021) for flow over the triangle and semi-circular cylinders, respectively.

Flow control methods around bluff bodies are classified into three categories: (i) passive, (ii) active open-loop, and (iii) active closed-loop control methods (Choi et al., 2008). The passive control method requires
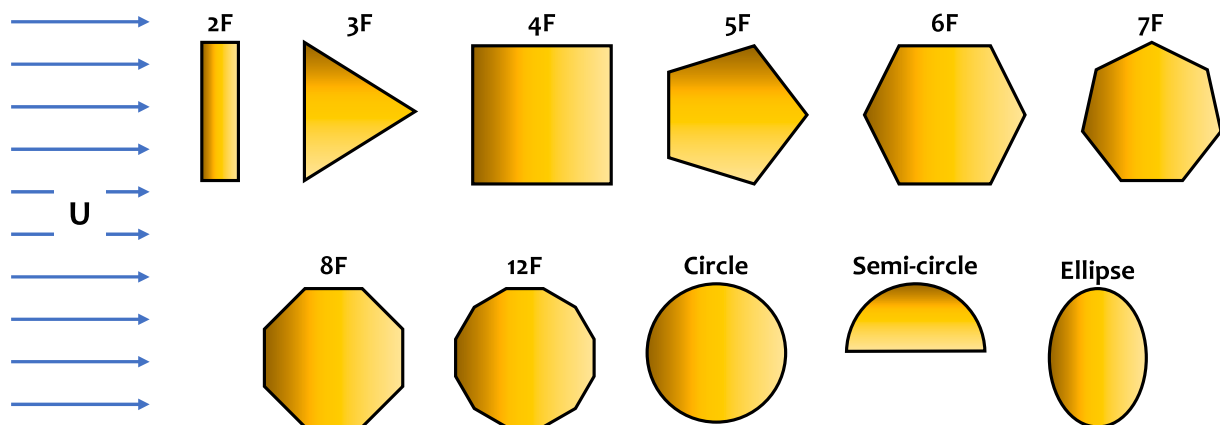

Fig. 2. Schematic of different shapes of bluff bodies (Xu et al., 2017; Lysenko et al., 2021; Lysenko and Ertesvåg, 2021). NF: N and F are the number of sides and the flat surface of polygon normal to the flow respectively.

no control loop or auxiliary power but comprises the use of vortex generators, geometry modifications, and placement of longitudinal riblets on cylinder surfaces. The active open-loop method requires an actuator with pre-determined commands to monitor the flow motion, while the active closed-loop is dependent on an actuator with sensors for real-time monitoring of flow motion. Passive control methods include guiding vanes (Grimminger, 1945), splitter plates (Wang et al., 2019b), surface protrusions (Nebres and Batil, 2012; Li et al., 2016), staggered buoyancy modules (Lekkala et al., 2020), grooves (Lim and Lee, 2002; Derakhshandeh and Gharib, 2020), strings (Baek et al., 2018; Lim et al., 2019), fairings (Wang et al., 2015; Zheng and Wang, 2021), and they are developed to reduce the drag/lift oscillations, and to suppress the vortex shedding. In contrast, active control methods include forced oscillations or rotating cylinders, application of electro-magnetic force, plasma actuators, suction, or blowing using synthetic jets (Oruc, 2017; Bhatta-charya and Gregory, 2020). It is challenging to execute active control methods in real-time due to the significantly complex actuators and extra cost functions involved. Apparently, passive control methods for flow over bluff bodies are more straightforward and significantly cheaper than the active control methods available, which can be more effective for improved flow suppression.

This work aims to present a detailed review of passive control flow methods for bluff bodies and their vortex patterns in the wake of a single cylinder for a broad range of *Re*. Apart from classical shapes for the cylinder such as circular and elliptical cylinders, the present review was extended to flow past bio-inspired cylinders such as wavy, helically twisted, and harbor seal vibrissae cylinders. A comparison was made between circular, elliptical, and helically twisted cylinders in terms of hydrodynamic coefficients to present an overview of their behaviours on the vortex dynamics and shedding process. In Section 2, the advancement of flow behind the circular cylinder is presented, while Sections 3 and 4 present the flow around the elliptical and bio-inspired cylinders, respectively. Section 5 provides the comparison of hydrodynamic coefficients of circular, elliptical, and bio-inspired cylinders. Conclusions are presented in Section 6.

2. Flow behind circular cylinder

Complexity of the flow around a cylinder increases as *Re* is varied for different flow conditions. When Re is varied, different vortex shedding formations and patterns can be observed downstream of the cylinder. In this section, we review flow characteristics, dynamics of vortex shedding, wake formations for various flow conditions and regimes around circular cylinders. For a broad range of Re, the wake formations including the Strouhal number (*St*), hydrodynamic coefficients (drag coefficient-C_D, lift coefficient-C_L, pressure coefficient-C_P), vortex formation lengths, recirculation lengths (L_r), separation angles (Θ) are examined.

The drag (C_D), lift (C_L), and pressure coefficients (C_P) are defined as:

$$C_D = \frac{2F_D}{\rho U_\infty^2 D_m L} \tag{2}$$

$$C_L = \frac{2F_L}{\rho U_\infty^2 D_m L} \tag{3}$$

$$C_P = \frac{2(P - P_\infty)}{\rho U_\infty^2} \tag{4}$$

where F_D and F_L are the total drag and lift forces, respectively, U_∞ is the free stream velocity, ρ is the fluid density, D_m is the mean diameter, L is the spanwise length of the cylinder, P is the pressure and P_∞ is the far-field pressure.

The non-dimensional Strouhal number, defining the vortex shedding frequency (F_s), reads

$$St = \frac{F_s D_m}{U_\infty} \tag{5}$$

The recirculation length (L_r) is defined as the length of the flow separation bubble. In the recirculation zone, the velocity vectors are in the opposite direction to the incident flow; however, at the end of this zone, the velocity vector change direction again towards the incident flow direction. The location of the separation point on the cylinder surface is known as the separation angle (Θ).

2.1. Flow regimes according to Reynolds numbers

Flow around the circular cylinder is categorised into eight regimes based on the visual assessment as presented in Table 1, as a function of Re (Zdravkovich, 1990). The significant difference between these regimes prevails in the transition of wakes and vortex shedding from one regime to the other. When the transition takes place between the regimes, it affects the hydrodynamic coefficients, vortex shedding patterns, separation point and recirculation length. For better understanding, the regimes are further simplified into three broad categories based on the variation of *St* as shown in Fig. 3: (i) laminar (Re < 300) (ii) sub-critical ($300 < \text{Re} < 1.4 \times 10^5$), and (iii) critical and super-critical (Re ≥ 1.4×10^5). The *St* value rises to 0.2 in the laminar region and then remains in the range of 0.2–0.23 for the sub-critical region. Then, *St* increases in critical and super-critical regions attaining a maximum value of ~0.47. Tables 2 and 3 summarises some of the significant experimental and numerical studies, respectively.

The wake behind a two-dimensional (2D) circular cylinder becomes complex due to the interaction of boundary and shear layers. This wake interaction becomes complex when the extra length (spanwise ratio (SR) = ratio of the length in spanwise direction (L_Z) to the diameter of the cylinder (D) = L_Z/D) is added in the spanwise direction for a three-dimensional (3D) cylinder. Hence, the wake formations behind the cylinder depend upon Re, *SR*, surface roughness and the blockage ratio (BR = frontal area of the cylinder over the cross-section of the wind tunnel). Prasanth and Mittal (2008) and Lekkala et al. (2021) revealed that all these parameters have a substantial impact on C_D, C_L, C_P, vortex shedding frequency and Θ.

The effect of Re, L_Z/D, and blockage ratio on the fluctuating lift force of the circular cylinder in cross flow (*CF*) was experimentally investigated by Norberg (2001). The author have showed the root mean square (RMS) of the lift coefficient ($C_{L, RMS}$) as a function of Re within the 2D laminar regime, which may be expressed as $\sqrt{(\varepsilon/30) + (\varepsilon^2/90)}$ where $\varepsilon = (\text{Re} - 47)/47$. $C_{L, RMS}$ significantly decays when Re is increased to a critical regime. The experimental work by Desai et al. (2020) obtained similar results.

The flow around the circular cylinder forms the primary wake and loses its stability when Re ≥ 47. For Re ≥ 110, a secondary wake is formed, leading to the formation of von Karman vortex street shedding (Verma and Mittal, 2011). The variation of the time-averaged drag coefficient ($\overline{C}_D$) in the laminar regime ($40 \leq \text{Re} \leq 180$) was studied by Chopra and Mittal (2019), who concluded that as Re increases, $\overline{C}_D$

Table 1
Flow regimes around the circular cylinder as a function of Re (Zdravkovich, 1990).

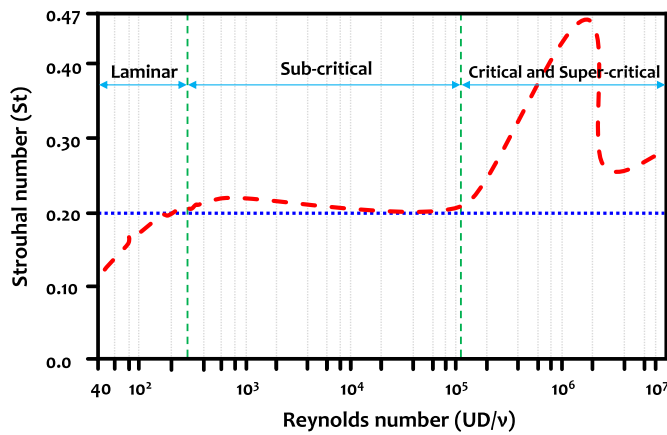| Category	**Re** range	Flow regime
i	Re < 1	Creeping flow
	$3.5 < \text{Re} < 30 - 40$	Steady separation flow
	$30 - 40 < \text{Re} < 150 - 300$	Laminar periodic shedding
ii	$150 - 300 < \text{Re} < 1.4 \times 10^5$	Subcritical (transitional)
iii	$1.4 \times 10^5 < \text{Re} < 1.0 \times 10^6$	Critical
	$1.0 \times 10^6 < \text{Re} < 5.0 \times 10^6$	Supercritical
	$5.0 \times 10^6 < \text{Re} < 8.0 \times 10^6$	Trans-critical
	Re ≥ 8.0×10^6	Post-critical

Fig. 3. Variation of Strouhal number versus Reynolds number for circular cylinder (Blevins, 1977).

behaves non-monotonically. When Re > 180, a wake transition occurs from 2D to 3D, which was observed by Williamson (1996b), Barkley and Henderson (1996), and Behara and Mittal (2010). Akbar et al. (2011) stated that the onset of 3D hysteresis interval is likely to be between $170 \leq Re \leq 189$. According to Williamson (1996b), when Re is increased beyond a critical value (Re_{cr}), the mode of wake instability emerges and undergoes a transition as (i) the instability of the primary wake emerges at Re ~ 47, (ii) dislocations of large-scale vortex shedding for the onset of mode A (mode A*) instability occurs at Re ~ 190, (iii) for $230 < Re < 250$, mode A* is switched to mode B, and (iv) for Re > 260, the disordered mode B structure increases gradually. Re_{cr} from other experimental works is 150 by Roshko (1954) and Tritton (1959), 178 by Williamson (1988, 1989), 165 by Norberg (1994), 205 by Miller and Williamson (1994), 190.2 by Posdziech and Grundmann (2001) and 190.5 by Rao et al. (2013a). Based on nonlinear stability analysis, the transition of mode A* to mode B takes place in the Re range of 230–265 and 230–260 as predicted by Barkley et al. (2000) and Sheard et al. (2003), respectively. This shows a good agreement with experimental work by Williamson (1996b) for the Re range of 230–250. Fig. 4 presents the fully developed wake flow structures of Mode A and Mode B.

On the other hand, Behara and Mittal (2010) investigated the energy transition from mode A* to mode B and found $Re_{cr} \sim 270$ by using power spectra of the velocity signal. This Re_{cr} is slightly higher than that reported by Williamson (1996b). Two different vortex shedding frequencies were noticed by Williamson (1996b) during the transition regime. Saha et al. (2003) found that the transition from periodic vortex shedding to mode A takes place due to the discontinuity in the $Re - St$ relationship at Re = 190. The switch of mode A to mode B was observed at Re ≈ 250 which was characterised by the second discontinuity in the Strouhal law. Jiang et al. (2016) found that the progressive wake shift process from mode A* to mode B was perfectly seized at Re in the range of 230–260. Fig. 5 presents the probability of incidence of mode A* and mode B vortex patterns as a function of Re. It can be seen that as Re increases, the probability of incidence of mode A* and mode B displays the monotonous fall and rise, respectively. Mode B becomes dominant beyond Re ~ 253, as shown in Fig. 5. Jung et al. (2019) studied the flow around a curved circular cylinder at $Re = 100$ and found that the flow features of the curved cylinder is different from straight cylinder due to its large radius of curvature. The authors found that the vortices are completely suppressed when the incident angle approached to 180° from 90°.

Kumar et al. (2016) investigated the lock-in phenomenon of a circular cylinder in uniform flow at Re = 100. The authors have observed a new wake-lock-in criterion for which (i) the most dominating frequency in the power spectrum of lift coefficient matches with the oscillation frequency of the cylinder and (ii) other peaks in power spectrum are present only at super-harmonic oscillation frequency. Behara et al. (2011) solved Navier-Stokes equations using a second-order finite difference fractional step methodology to study the impact of Re and V_r on the VIV phenomenon. The authors have observed two distinct vortices shedding, namely: (i) hairpin and (ii) spiral vortices. Jeong et al. (2020) investigated the effect of wave run-up of a circular cylinder using non-linear numerical wave tank techniques. The authors have concluded that the maximum wave run-up occurred at 0° and minimum occurred at 135°. Wong and Kim (2018) investigated the fatigue damage of riser subject to vortex-induced vibrations and developed a simplified method to predict fatigue damage based on data training. Kim et al. (2019) conducted a parametric study of riser subjected to currents. The authors have concluded that current flow speed, diameter of the cylinder

Table 2
Summary of experimental studies of flow around circular cylinders.

Researchers	Re	Test Facility	L_Z/D	BR	Measurement
Yokuda and Ramaprian (1935)	$1.0 \times 10^4 \sim 1.0 \times 10^5$	Wind tunnel	0.91	–	$\overline{C}_P$, and C_{DF}
Roshko (1954)	$0.5 \times 10^5 \sim 4.5 \times 10^5$	Low turbulence wind tunnel	0.281	–	C_D and St
Tritton (1959)	$0.5 \sim 100$	Wind and Water tunnel	–	–	C_D
Achenbach (1968)	$6.0 \times 10^4 \sim 5.0 \times 10^6$	Wind tunnel	3.33	–	C_D, C_P, C_F, C_{DP}, and C_{DF}
Son and Hanratty (1969)	$5.0 \times 10^3 \sim 1.0 \times 10^6$	Water tunnel	–	–	St and Velocity gradients
Kacker et al. (1974)	$1.40 \times 10^4 \sim 2.5 \times 10^5$	Suction wind tunnel	$0.25 \sim 9$	4.7%	C_D, C_L, and St
Bruun and Davies (1975)	$0.6 \sim 6.0 \times 10^5$	Wind tunnel	10	13	C_D, and C_L
Cantwell and Coles (1983)	1.4×10^5	Wind tunnel	10	10%	C_D, C_{pb}, and St
Schewe (1983)	$2.3 \times 10^4 \sim 7.1 \times 10^6$	Wind tunnel	0.6	0.4%	C_D and St
Norberg (1987)	$50 \sim 2.0 \times 10^5$	Wind tunnel	$0.1 \sim 50$	1.6%	St, $\overline{C}_P$ and $C_{P,\ RMS}$
Szepessy and Bearman (1992)	$8.0 \times 10^3 \sim 1.4 \times 10^6$	Low-speed wind tunnel	$0.25 \sim 12$	7.7%	C_D, C_L, C_P, and vortex patterns
Shih et al. (1993)	$3.0 \times 10^5 \sim 8.0 \times 10^6$	Pressurized wind tunnel	8.0	11	C_D, C_P, C_{pb}, and Θ
West and Apelt (1993)	$1.0 \times 10^4 \sim 2.5 \times 10^5$	–	–	–	C_D, and C_L
Ong and Wallace (1996)	3.9×10^3	Hot-wire anemometry	84	–	Velocity spectrum
Rajagopalan and Antonia (2005)	$740 \sim 1.48 \times 10^4$	Hot wire	2.2	3%	$\langle \overline{u} \rangle / U_\infty$
Dong et al. (2006)	$3.9 \times 10^3, 4.0 \times 10^3, 1.0 \times 10^4$	PIV	8.78	8.3%	C_D, C_L, C_{pb}, St, Shear layer length and power spectral density
Perrin et al. (2007)	1.4×10^5	PIV	4.8	20.8%	C_D, and C_L
Parnaudeau et al. (2008)	3.9×10^3	Wind tunnel PIV	20	4.3%	St, L_r, and $\langle \overline{u} \rangle / U_\infty$
Adaramola et al. (2012)	2.3×10^4	Low-speed wind tunnel	9	–	$\langle \overline{u} \rangle / U_\infty$ and $\langle \overline{v} \rangle / V_\infty$
Molochnikov et al. (2019)	3.9×10^3	Wind tunnel with SIV	10	13%	$\langle \overline{u} \rangle / U_\infty$ and $\langle \overline{v} \rangle / V_\infty$
Desai et al. (2020)	$1.49 \times 10^5 \sim 5.0 \times 10^5$	PIV	22	3.4%	C_D, C_L, C_P, and L_F

Table 3

Summary of numerical studies of flow around the circular cylinders.

Researchers	**Re**	Method	Grid	L_Z/D	Convection Term	Turbulence model	Measurement
Norberg (1987)	$500 \sim 5.0 \times 10^3$	LES 3D	–	$8.83 \sim 1912$	–	–	C_{Pb}
Beaudan and Moin (1994)	3.9×10^3	LES (2D and 3D)	–	–	upwind	–	C_D and C_L
Koumoutsakos and Leonard (1995)	$400 \sim 9.5 \times 10^3$	–	–	–	–	Biot-Savart law	C_D
Breuer (1998)	3.9×10^3	LES (2D and 3D)	O-type	–	–	–	C_D, C_L, C_P, and C_{pb}
Fröhlich et al. (1998)	$350 \sim 2.0 \times 10^5$	LES	–	$0.2 \sim 25$	LUST	Dynamic, SMAG	C_D, C_{pb}, St, Θ, L_r and $\langle \bar{u} \rangle/U_\infty$
Breuer (1999)	1.4×10^5	LES (3D)	O-type	$0.336 \sim 0.654$	–	–	C_D, C_{pb}, St, and Θ
Kravchenko and Moin (2000)	3.9×10^3	LES	O-type grids	–	–	Dynamic, SMAG	C_D, C_{pb}, St, Θ, $\langle \bar{u} \rangle/U_\infty$ and Reynolds stresses
Ma et al. (2000)	$500 \sim 5.0 \times 10^3$	LES and DNS	cartesian grid	–	–	SMAG	C_D, C_L, and St
Travin et al. (2000)	5.0×10^4, $1.4 \times 10^5, 3.0 \times 10^6$	DES (3D)	cartesian grid	–	upwind	–	C_D, C_P and St
Fröhlich et al. (2001)	$3.9 \times 10^3, 1.4 \times 10^5$	LES (3D)	O-grid	8	upwind	SMAG	Correlation length, wall shear stress, Reynolds stress
Salvatici and Salvetti (2003)	2.0×10^4	LES	–	3	–	Dynamic	C_D, C_L, C_{pb}, St, and Θ
Kim and Choi (2005)	≤ 40	–	–	$3 \sim 12$	–	–	C_P, C_{DF}, and C_{LF}
Dong et al. (2006)	$3.9 \times 10^3, 4.0 \times 10^3$, 1.0×10^4	DNS (3D)	cartesian grid	8.78	upwind	–	C_D, C_L, C_{pb}, St and Shear layer length, power spectral density
Perrin et al. (2007)	1.4×10^5	DES	–	4.8	hybrid	–	C_D and C_L
Xu et al. (2007)	3.9×10^3	LES and DES	O-type grid	–	–	Dynamic, Spalart-Allmaras, SST	C_D, C_L, and C_P
Parnaudeau et al. (2008)	3.9×10^3	LES	cartesian grid	20	upwind biased	–	St, L_r, and $\langle \bar{u} \rangle/U_\infty$
Wissink and Rodi (2008)	3.3×10^3	DNS	O-grid	$4 \sim 8$	–	–	St, Θ and $\langle \bar{u} \rangle/U_\infty$
Mani et al. (2009)	$3.9 \times 10^3, 1.0 \times 10^4$	LES	staggered	–	Runge–Kutta	Dynamic	C_D, C_{pb}, St, Θ, and $\langle \bar{u} \rangle/U_\infty$
Afgan et al. (2011)	3.9×10^3	LES	cartesian grid		upwind	Dynamic, SMAG	C_D, C_L, C_{pb}, St, and Θ
Lysenko et al. (2014)	2.0×10^4	LES	O-grid	π	–	SMAG, k-equation	C_L, C_{pb}, St and L_r
Rodríguez et al. (2015)	$2.5 \times 10^5 \sim 8.5 \times 10^5$	LES	cartesian grid	$0 \sim 0.5\pi$	–	WALE	C_D, C_P, C_L, L_r, and L_F
D'Alessandro et al. (2016)	3.9×10^3	DES	O–H type grid	–	–	SMAG	C_P and C_D
Guo et al. (2016)	3.9×10^3	LES	–	–	–	–	C_P and $\langle \bar{u} \rangle/U_\infty$
Lloyd and James (2016)	$1.26 \times 10^5, 6.13 \times 10^4 \sim 5.06 \times 10^5$	LES (3D)	–	–	–	–	C_D, C_L, C_P, and St
Yeon et al. (2016)	$6.31 \times 10^4, 7.57 \times 10^5$	3D	curvilinear grid	$2 \sim 8$	QUICK WENO	–	C_D, C_{pb}, C_L, St, and Θ
Cheng et al. (2017)	$3.9 \times 10^3 \sim 8.5 \times 10^5$	LES	O-grid	$\pi \sim 2\pi$	–	Stretched vortex	C_L, C_P, C_{DF} and $\langle \bar{u} \rangle/U_\infty$
Qiu et al. (2017)	$6.31 \times 10^4, 7.57 \times 10^5$	2D/3D URANS, DES and LES	H-type grid	$2, \pi, 12$	upwind, hybrid, QUICK	SST k-ω, Dynamic, k-ε	C_D, C_L, and St
Wen and Qiu (2017)	$6.31 \times 10^4, 7.57 \times 10^5$	2-D/3-D	H-type	6	upwind	k-ε, SST k-ω, SST-LCM	C_D, C_L, and St
Ye and Wan (2017)	$6.31 \times 10^4, 7.57 \times 10^5$	RANS	overset grid	–	upwind	SST k-ω	$\overline{C}_D$, $\overline{C}_L$, $C_{L, RMS}$, and St
Wang et al. (2018a)	1.07×10^3, 2.0×10^4, 3.0×10^5	RANS (2D) and LES (3D)	H-type grid	–	–	k-ω, SMAG	C_D and $\langle \bar{u} \rangle/U_\infty$
Garcia et al. (2019)	1.0×10^4	2D and 3D	cartesian grid	0.1–1, π and 10	QUICK	Dynamic	C_D and C_L
Sarwar and Mellibovsky (2020)	2.0×10^3	DNS	H-type grid	2.5	–	–	C_D, C_{pb}, L_r and Θ
Tian and Xiao (2020)	3.9×10^3	LES	H-type grid	–	–	SMAG, k-equation, WALE	$\langle \bar{u} \rangle/U_\infty$, C_{pb}, and L_r
Jiang and Cheng (2021)	$400 \sim 3.9 \times 10^3$	LES	O-type	–	–	SMAG	C_D, $C_{L, RMS}$, and L_r

Note: Reynolds number (Re), the method used, type of grid, L_Z/D is spanwise length ratio, Convection term, and Turbulence model. C_D, C_L, and C_P represent drag, lift, and pressure coefficients, respectively. C_{DP} and C_{DF} are coefficients of drag due to pressure and friction, respectively. θ and St are separation angle and Strouhal number. L_r is recirculation length. $\langle \bar{u} \rangle/U_\infty =$ streamwise velocity.

have significant effect on the fatigue damage of the riser.

For the flow past the cylinder, its velocity profile changes behind the cylinder due to the wake shielding effect. The flow velocity is significantly reduced near the cylinder, and it is restored to the free stream velocity away from the cylinder in the transverse direction. Further downstream of the cylinder, the velocity profile is restored as well. The flow around the circular cylinder was investigated by Parnaudeau et al.

(2008) experimentally and numerically using the hot-wire anemometry with the particle image velocimetry (PIV) and Large Eddy Simulations (LES) at Re $= 3.9 \times 10^3$, respectively. They found that the results from LES have produced a good agreement with experimental results with an uncertainty of $\pm 10\%$. The authors have observed a U-shaped streamwise velocity profile in the wake of a cylinder with a strong velocity shortfall in the recirculation zone, and it developed into a V-shape further
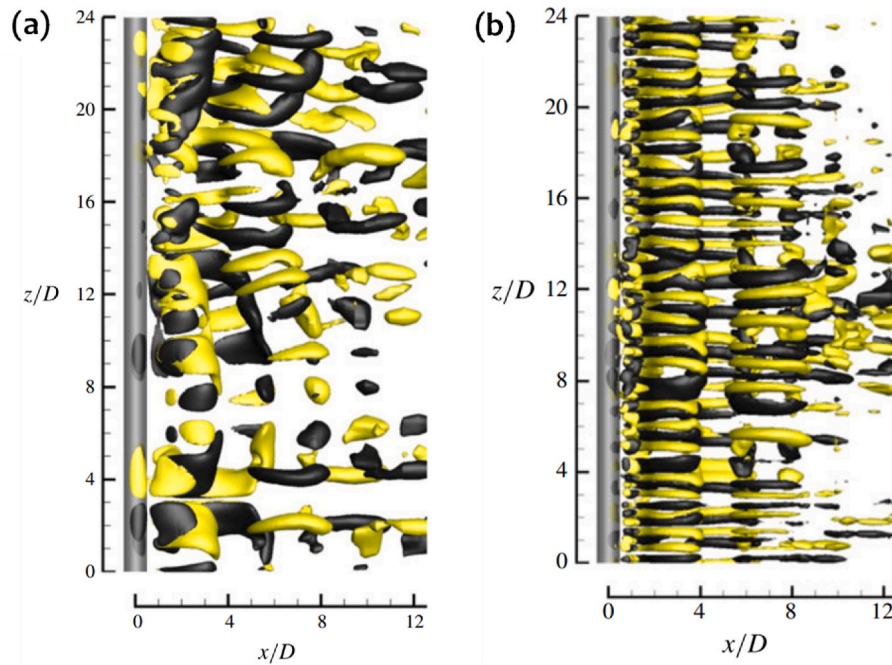
Fig. 4. Fully developed wake flow structures of (a) Mode A and (b) Mode B. Dark grey and light-yellow present the positive and negative values of the vortices, respectively (Jiang and Cheng, 2017). Mode A and Mode B are defined as small-scale instabilities of vortex dislocations. (For interpretation of the references to colour in this figure legend, the reader is referred to the Web version of this article.)

downstream as shown in Fig. 6. Lysenko et al. (2012) used an O-type curvilinear grid to study the effect of Smagorinsky (SMAG) and dynamic k-equation (TKE) sub-grid-scale (SGS) models at $Re = 3.9 \times 10^3$ on flow features behind the cylinder. They reported the existence of flow bifurcation in U and V-shaped profiles for TKE and SMAG SGS models, respectively, at $x/D = 1.06$ behind the cylinder. For mean streamwise velocity profiles ($\langle u \rangle / U_\infty$), Lysenko et al. (2012) observed a strong velocity deficit in the recirculation zone for LES-dynamic k-equation (TKE), which agreed well with Parnaudeau et al. (2008) and Kravchenko and Moin (2000). The velocity profile obtained using LES-TKE showed a U-shaped profile close to the cylinder ($x/D = 1.06$), which evolved as a V shape further downstream ($x/D = 2.02$) as shown in Fig. 6, while the LES-Smagorinsky (SMAG) model showed a V-shaped profile at x/D = 1.06. The velocity profiles obtained from Lysenko et al. (2012) using LES-SMAG agreed well with experiments by Lourenco and Shih (1994) and numerical simulations by Ma et al. (2000). The abnormal behaviour of mean transverse velocity profiles ($\langle v \rangle / U_\infty$) observed by Lourenco and Shih (1994) shown in Fig. 6 (right) can be attributed to the disturbances from the experimental setup. The $\langle v \rangle / U_\infty$ profiles by Lysenko et al. (2012) using SMAG and TKE agreed well with Lourenco and Shih (1994) and Parnaudeau et al. (2008). Lysenko et al. (2012) concluded that SMAG and TKE SGS models led to V- and U-shaped velocity profiles.

Mittal and Balachandar (1997) and Kravchenko and Moin (2000) performed LES and predicted U-shaped velocity profile near the wake of the cylinder, whereas Lourenco and Shih (1993) measured V-shaped velocity profile at the same location. Ma et al. (2000) performed DNS and LES with spectral FEM and reported two converged states based on the shear layers and spanwise length (L_Z) in the wake of flow field. They have observed the U-shaped mean velocity at $L_Z/D = \pi$ and the V-shaped mean velocity at $L_Z/D = 2\pi$. At $Re = 3.9 \times 10^3$, Dong et al. (2006) observed U-shaped and V-shaped velocity profiles for $L_Z/D = \pi$ and 1.5π, respectively. The U-shaped wake is 11–16% longer than the V-shaped wake for $Re = 3.9 \times 10^3$. Beaudan and Moin (1994), Kravchenko and Moin (2000), and Mahesh et al. (2004) observed that doubling the domain size in the spanwise direction does not significantly impact the results. This observation is contrary to that reported in Ma

et al. (2000).

Lysenko et al. (2012) observed the influence of shear-layer resolution on the bifurcation of the flow near the wake of the cylinder. This means that the SGS model has a significant effect on the flow bifurcation. The process of formation of free shear layers for TKE and SMAG SGS models are presented in Fig. 7. Don et al. (2006) reported that the flow at $Re = 1.0 \times 10^4$ has a 30% shorter shear layer when compared to the shear layer at $Re = 3.9 \times 10^3$. D'Alessandro et al. (2016) employed OpenFOAM to simulate the flow near the wake of a cylinder using Direct Numerical Simulation (DNS) and have demonstrated that U-shaped and V-shaped streamwise velocity profiles were observed at $x/D = 1.0$ depending upon the meshing technique and discretization schemes. In contrast, Khan et al. (2019) stated that the coarse and refined grids yield V- and U-shaped flow velocity profiles, respectively. They also proved that the computational domain size and mesh resolution in the spanwise direction significantly affect results from the analysis when compared to the spanwise length. Molochnikov et al. (2019) conducted experiments for $Re = 3.9 \times 10^3$ through the Smoke Image Velocimetry (SIV) and observed the U-shaped streamwise velocity component profile directly behind the cylinder. This profile transforms to a V shape as the distance increases downstream of the cylinder: This is in good compliance with PIV experimental results by Parnaudeau et al. (2008). A similar study was carried out by Sarwar and Mellibovsky (2020) at $Re = 2.0 \times 10^3$ and found that the U-shaped streamwise velocity profile evolves at $x/D = 1.0$ and this profile transforms to a V-shaped profile near the wake of the cylinder at $x/D = 2.0$.

The iso-surfaces from the TKE SGS model are long and 2D in nature. The free shear layers are extended twice the diameter of the cylinder in a streamwise direction. At the same time, for the SMAG model, a transition of iso-surfaces from 2D to 3D takes place very close to the cylinder surface, which increases the drag and lift forces. LES with SMAG was used by Prsic et al. (2014) to simulate the flow around the cylinder at $Re = 1.31 \times 10^4$ to investigate the effect of various numerical parameters such as the cylinder spanwise length (L_Z), mesh refinement, and time step on C_D, C_L, pressure distributions, St, L_r and Θ. It was found that (i) the recirculation length (L_r) decreases as Re is increased, (ii) the high
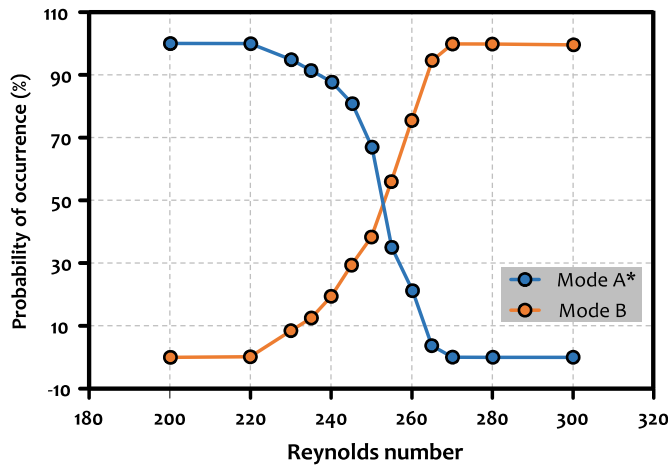
Fig. 5. Probability of occurrence of mode A* and mode B (recreated from Jiang et al., 2016). Mode A* is defined as Mode A with large-scale vortex dislocations.

mesh refinement in the spanwise direction does not show a substantial impact on the results, (iii) the time step does not impact on the results as long as a low Courant number is maintained, and (iv) $L_Z/D = 4$ is sufficient to capture the 3D effects of the flow. Stringer et al. (2014) established a high-resolution methodology to evaluate the flow around the cylinder for a wide range of Re (40 to 1.0×10^6) using the Unsteady Reynolds Averaged Navier-Stokes (URANS) model in the open-source code (OpenFOAM) and a commercial CFD (ANSYS) package. For Re < 1.0×10^3, the predicted results by the two solvers produced highly accurate results to achieve good correlation with experiments. For subcritical flow regime (Re < 1.0×10^5), the OpenFoam solver predicted significantly better results than ANSYS when compared with the experiment. For the critical flow regime ($1.0 \times 10^5 <$ Re < 1.0×10^7), the prediction from ANSYS achieved good agreement with experimental results but failed to capture the realistic wake. It was demonstrated that URANS is proficient in predicting the flow characteristics for Re ≤ 1.0×10^3 and Re > 1.0×10^3. The results showed large variations from experiments, including C_D and C_L. Ong et al. (2009) utilised 2D URANS equations with the $k - \varepsilon$ turbulence model to solve the flow at high Re = 1.0×10^6, 2.0×10^6, and 3.6×10^6. Ong et al. (2009) compared the results with the experiment and LES analysis where the shedding frequencies showed a good agreement while the shear stress and pressure distribution showed divergence.

The effectiveness of RANS method with $k - \omega$ SST turbulence model

was investigated by Rosetti et al. (2012) and found that the method does not deliver an adequate resolution of flow around the cylinder, particularly at high Re. This was due to the even Reynolds stresses, and inherent characteristics of uniform eddy viscosities. To overcome this issue, Rosetti et al. (2012) suggested a hybrid approach based on the URANS method, which was able to enhance the consistency of prediction of flow properties by numerical analysis at higher Re. Despite the observations by Rosetti et al. (2012), Khan et al. (2017) stated that RANS with $k - \omega$ SST turbulence model at high Re = 1.0×10^4 has the ability and precision to predict VIV. DNS has been found to predict accurate VIV phenomenon results, superior to the URANS approach, for a fixed and oscillating circular cylinder at $Re = 3.0 \times 10^3$ to 3.0×10^4 (Nguyen and Nguyen, 2016).

An Adaptive Local 2D convolution Method (ALDM) SGS model with cartesian grids was used in the implicit LES by Meyer et al. (2010) to assess the flow around a circular cylinder at Re = 3.9×10^3 to control the truncation error and maintain the discretization accuracy near the boundaries. The assessment of four SGS models and dynamics of the turbulent kinetic energy in the wake of a circular cylinder at the sub-critical Re = 3.9×10^3 was carried out by Tian and Xiao (2020). From this study, they found that different SGS models did not show a substantial impact on the mean flow and turbulence properties. Chapelier et al. (2014) assessed the accuracy of the Discontinuous Galerkin (DG) method of DNS flow around a circular cylinder and found that higher-order DG simulations predicted accurate results on a coarse mesh, leading to the reduction of the computational cost. Wornom et al. (2011) used the Variational Multi-Scale Large Eddy Simulations (VMS-LES) concept from Hughes et al. (2000) to study the flow around the circular cylinder for different Re to investigate the effect of Re on flow quantities.

A hybrid strategy was developed by Moussaed et al. (2014) to blend the Reynolds Averaged Navier Stokes and VMS-LES to investigate the flow around a circular cylinder. They confirmed that this method is more suitable at High Re to the reduced use of exceptionally refined grids and led to a reduction in the computation time and cost. de la Llave Plata et al. (2018) demonstrated the effectiveness of the DG solver in capturing the scale-resolving capabilities based on VMS by conducting LES of the flow around a circular cylinder at Re = 2.0×10^4 and 1.4×10^5. Ahmadi and Yang (2020) investigated the turbulent flow behind the circular cylinder at a supercritical Re using LES. They have investigated the flow properties using four different sub-grid scale turbulence models. They have addressed the importance of mesh resolution at the top and bottom of the shear layers along with the high-resolution mesh near the cylinder wall.
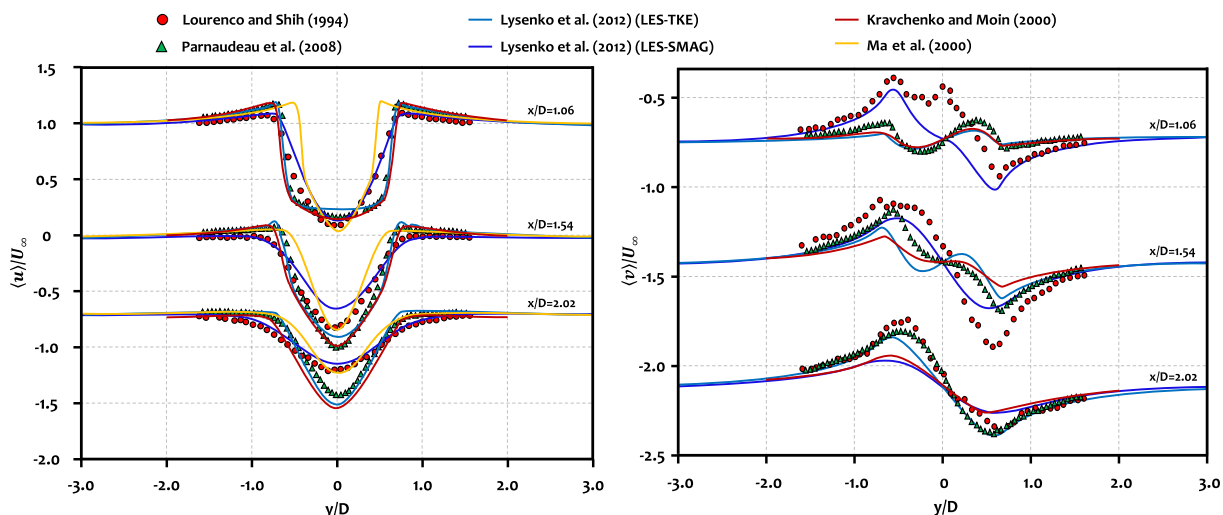

Fig. 6. Mean streamwise and transverse velocity profiles at three locations in the wake of a circular cylinder at $Re = 3.9 \times 10^3$.
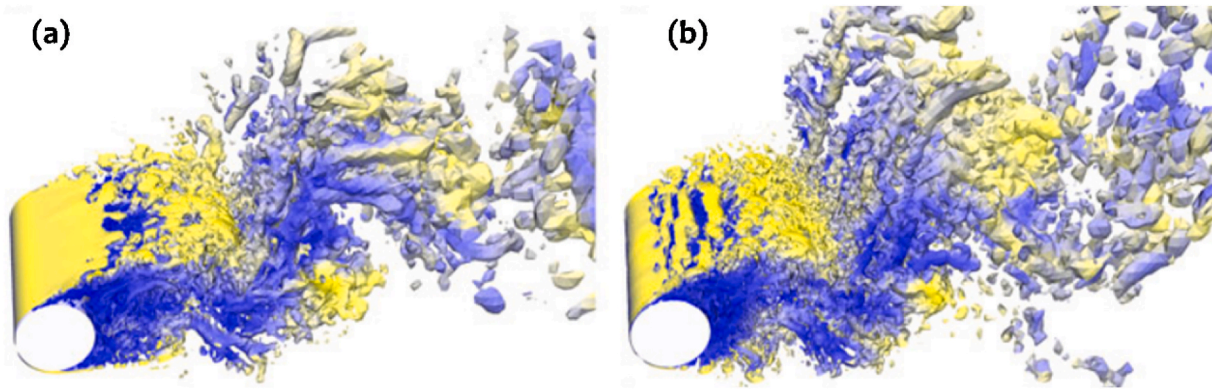
Fig. 7. Iso-surfaces of (a) TKE and (b) SMAG SGS models (Lysenko et al., 2012).

2.2. Effect of spanwise length ratio (L_Z/D)

The effect of spanwise length ratio (L_Z/D) on the flow around a circular cylinder at Re = 100 was investigated by Lei et al. (2001) who concluded that the results are significantly improved with the 3D analysis when $L_Z/D > 2$. Ma et al. (2000) investigated the effect of L_Z/D by increasing L_Z/D from π to 2π and observed the 30% decrease in the recirculation length (L_r). However, Lehmkuhl et al. (2013) observed only 10% and 0.2% changes in L_r when doubling L_Z/D from π to 2π. Lei et al. (2001) presented the 3D DNS results based on the Finite difference method (FDM) at Re = 1.0×10^3 and $L_Z/D = 0$ to 6.0. They concluded that the hydrodynamic force and pressure coefficients over the circular cylinder converge for $L_Z/D \geq 2.0$. Gioria et al. (2011) investigated the effects of computation domain size and L_Z/D on the flow around a circular cylinder at Re = 400 based on the spectral element method (SEM). They have observed the development of 3D flow features at $L_Z/D = 0.35$, which converge at $L_Z/D \geq 6.0$. The authors have also recommended that 3D flow characteristics are fairly captured when L_Z/D exceeds 6.0 while Mittal (2013) and Kondo (2012) suggested L_Z/D at 4.0 and 9.6, respectively. The effect of span length (L_Z/D) on the flow properties was investigated numerically by Zhao and Cheng (2014) at Re = 300, $m^* = 2.0$, and uniform flow conditions using 3D Navier-Stokes equations. When the cylinder was fixed, the authors observed no vortex shedding for $L_Z/D < 2$; however, the vortex shedding was observed at $L_Z/D = 1$ and 2 for the oscillating cylinder. The iso-surfaces of the vortex flow and contours of axial vorticity behind the stationary cylinder are presented in Figs. 8 and 9, respectively, for different L_Z/D. It can be observed that, for $L_Z/D = 1.0$ and 2.0, the separated shear layers from both sides of the cylinder extended further downstream without any interactions between them, as shown in Fig. 9 (a) and (b). At $L_Z/D = 5.0$, the shear layers bend and form weak vortices far from the cylinder, which does not have a strong impact on the lift fluctuations, as presented in Fig. 9(c). For $L_Z/D = 10.0$, the vortices are formed closer than for $L_Z/D = 5.0$, and for $L_Z/D = 20.0$ the vortices are closer than $L_Z/D = 10.0$. It was observed from Figs. 8 and 9 that as the L_Z/D increases, the vortex shedding moves closer to the cylinder.

Yeon et al. (2016) found that C_D decreased from 1.20 to 0.92 when Re increases from the sub-critical regime (Re = 6.31×10^4) to the critical regime (Re = 2.52×10^5). They also observed that the large and small L_Z/D values produce the best results for sub-critical and super-critical Re, respectively, whereas the results are less dependent on L_Z/D for the critical regime. Experiments in a recirculating water channel were carried out by Gonçalves et al. (2015) at higher Re ranges between 1.0×10^4 to 5.0×10^4 to study the low aspect ratio ($0.1 \leq L_Z/D \leq 2.0$) effect on the flow around a circular cylinder. They found that, as L_Z/D increases, the drag coefficient decreases from $C_D \approx 0.75$ for $L_Z/D = 0.3$ to $C_D \approx 1.0$ for $L_Z/D = 2.0$. However, $C_L \approx 0.06 \pm 0.01$ remains constant for $0.75 \leq L_Z/D \leq 2.0$. The variation of Strouhal number follows a

similar trend to that of C_D. The vortex shedding disappears as L_Z/D decreases, and the dominance of von Karman vortex shedding was observed at $L_Z/D = 2.0$. Jiang et al. (2017a) used DNS to study the effect of spanwise length and the boundary conditions on flow properties behind the cylinder. They have recommended that $L_Z/D > 10$ is sufficient to obtain the hydrodynamic forces and wake structures without any effect from the computational domain setup restrictions. Jiang and Cheng (2021) recommended $L_Z/D = 6.0$ for Re = 400 to 2.0×10^3 and $L_Z/D = 3.0$ for Re = 2.5×10^3 to 3.9×10^3. Sarwar and Mellibovsky (2020) also demonstrated that the length of the computational domain less than 2.5D in a spanwise direction failed to reproduce first and second-order turbulent statistics in the cylinder wake. This is possibly due to the presence of unaccounted for large-scale motions hindered by the limited domain size in the spanwise direction. The effect of span on the turbulence of the flow behind the cylinder was studied by Garcia et al. (2019) at Re = 1.0×10^4. The authors have summarised that the turbulence behind the cylinder is similar for $L_Z/D = \pi$ and 10.0, and the Strouhal number converges to St = 0.2. For $L_Z/D \geq \pi$, the turbulence kinetic energy and lift force are less affected, meaning that the 3D turbulence dominates.

2.3. Effect of rotational rate (α)

In this section, the effect of rotation rate (α) along with Re on the flow characteristics of the circular cylinder is reviewed. The non-dimensional rotation rate is defined as the ratio of the surface speed of the cylinder and the flow speed. The non-dimensional α with respect to flow speed is given as $\alpha = r\omega/U$ where r is radius, ω is angular velocity of the cylinder about its own axis and U is the flow speed.

A 2D laminar study was carried out by Stojković et al. (2002) to investigate the effect of Re ($0.01 - 45$) and rotational rates ($0 \leq \alpha \leq 6.0$) on C_D and C_L of the cylinder. For low Re, C_D was not impacted by α while the variation of C_L was linearly proportional to α. For higher Re, C_D decreased with an increase in α, eventually leading to negative values, but C_L was a linear function of α until $\alpha < 2.0$ beyond which it increased considerably. They proposed a quadratic relation to calculate C_L ($\approx m + n.\alpha^2$) where $m = 1.322$ and $n = 0.994$ for α in the range of 2.0 to 5.0. Rao et al. (2013b) studied the flow behind the rotating cylinder for $\alpha \leq 2.5$ and Re ≤ 400, and they observed the 3D wake formations identical to the non-rotating cylinder for $\alpha \leq 1.0$. A 2D and 3D numerical simulation to investigate the effect of rotational rates was carried out by Bourguet and Jacono (2014) at Re = 100. It was observed that the rotating cylinder experiences the flow-induced instability for $\alpha \leq 4.0$. The maximum amplitude (A/D) stimulated by the oscillations experienced by the rotating cylinder was near to 1.9 times the diameter of the cylinder. A new wake T + S pattern (a trio of vertices and a single vortex shedding for each cycle) was identified during the oscillations of a rotating cylinder as shown in Fig. 10. Zhao et al. (2014) examined VIV

of one and two degrees of freedom (DoF) rotating cylinder at Re = 150 for $\alpha = 0.5$ and 1.0. For the one DoF case, the frequency and amplitude of the oscillating cylinder in CF direction followed a similar trend to that of a non-rotating cylinder, at $\alpha = 0.5$ and 1.0. As α was increased, the oscillation A/D of the cylinder increased, and the lock-in range became wider. They have noticed a 2S vortex shedding pattern in the lock-in range at all rotational rates and reduced velocities. For the two DoF case, a P + S vortex shedding pattern was observed for V_r that corresponds to the higher boundaries of the initial branch and a 2S pattern for all other V_r in the lock-in range.

The flow behind the circular cylinder was investigated by Lam (2009) using the flow visualisation and PIV experiments for $3.6 \times 10^3 \leq Re \leq 5.0 \times 10^3$ and $\alpha \leq 2.5$. It was discovered that as α increases, the wake formations become narrow, and vortices formation length diminishes, which led to the rise in the Strouhal frequency. Seyed-Aghazadeh and Modarres-Sadeghi (2015) investigated VIV of the rotating cylinder in a recirculating water tunnel for $350 \leq Re \leq 1.0 \times 10^3$ and $0 \leq \alpha \leq 2.6$. When $\alpha < 1.4$, the lock-in region turns into a narrow regime, and the vibration of the cylinder terminates at $\alpha < 2.4$. Seyed-Aghazadeh and Modarres-Sadeghi (2015) did not observe a substantial increase in the lock-in range, whilst Bourguet and Jacono (2014) and Zhao et al. (2014) observed a wider lock-in range. Munir et al. (2018) observed a wide lock-in range of rotating cylinders than the non-rotating cylinder for $0 \leq \alpha \leq 1.0$ at Re = 500, reduced velocity $(V_r) = 1$ to 13 and $m^* = 11.5$. The vortex shedding of the cylinders is suppressed when $\alpha = 2.5$ for $V_r = 5.0$ and $\alpha > 2.5$ for $V_r = 6.0$ and 7.0. It was found that the rotating cylinder's vortex shedding pattern resembles a stationary cylinder for $\alpha \leq 1.0$ which agrees with Rao et al. (2013b). The authors also observed the hairpin vortices when α is greater than the critical value. For $1.1 \times 10^3 \leq Re \leq 6.3 \times 10^3$, $m^* = 7.8$ and $\alpha = 2.0$, the maximum oscillation amplitude of the rotating cylinder was increased by 76% when compared to the non-rotating cylinder (Wong et al., 2017). Cheng et al. (2018) used the well-resolved LES with the stretched-spiral SGS to investigate the effect of Re and α on the lift crisis (defined as a sudden drop in the C_L as the designed parameter changes). They observed the lift crises when α is ranged from 0.48 to 0.6 for Re = 6.0×10^4.

Chen and Rheem (2019) concluded that the hydrodynamic forces of the cylinder are strongly dependent on the rotation rate and Re from the experiments investigating the flow with a rotating cylinder at a range of $1.0 \times 10^5 \leq Re \leq 1.59 \times 10^5$, $0 \leq \alpha \leq 8$. A 2D discrete vortex simulation method was used by Chen et al. (2020) to investigate the flow around a rotating circular cylinder with Re = 1.0×10^5 and the rotation rate from 0 to 19. The authors have observed four wake formations for different rotational rates, namely: (a) vortex shedding, (b) weak vortex shedding, (c) wake formation, and (d) formation of rotating wake. The variation of mean hydrodynamic coefficients with the rotation rate is presented in Fig. 11. It was concluded that the mean lift increases with α until it reached a certain value and then remains steady even though the rotation rate is further increased. In contrast, $\overline{C}_D$ initially decreases, then increases and ultimately attains a constant value. These observations agree well with experimental work by Chen and Rheem (2019). At $\alpha \approx 3.5$, the vortex shedding disappeared, and the Strouhal frequency was initially stable and then decreased when the rotation rate was increased. Aljure et al. (2015) analysed the effect of rotational rates on C_L, St, and separation point of the flow around a cylinder using DNS at Re = 5.0×10^3 and $0 < \alpha < 5.0$. The vortex shedding was suppressed at $\alpha \leq 2.0$. The rotation of the cylinder results in the shear layer shrinking, and the wake deflected to the tangential direction is permitted to form different shear layer lengths on the sides of the cylinder. Karabelas (2010) used LES to investigate the flow at Re = 1.4×10^5 and $0 < \alpha < 5.0$. The author stated that the wake formation patterns are strongly affected by the rotational rates: as α is increased, the stagnation point and the point of transition to turbulence are shifted towards greater the azimuthal angles and upstream, respectively. C_D decreases as α is increased whereas C_L is increased linearly.

The vortex shedding weakens and disappears in initial and increasing areas in Fig. 11. C_D attains a minimum value at the boundary line of the initial area which represents that the weak vortex shedding area acts as a transition zone between the initial and increasing areas. The hydrodynamic coefficients gradually increase in the wake area and remain steady in the equivalent area because the rotating wakes dominate the flow. The effect of incoming flow is neutralised, which stabilizes the hydrodynamic coefficients in the rotating wake area.
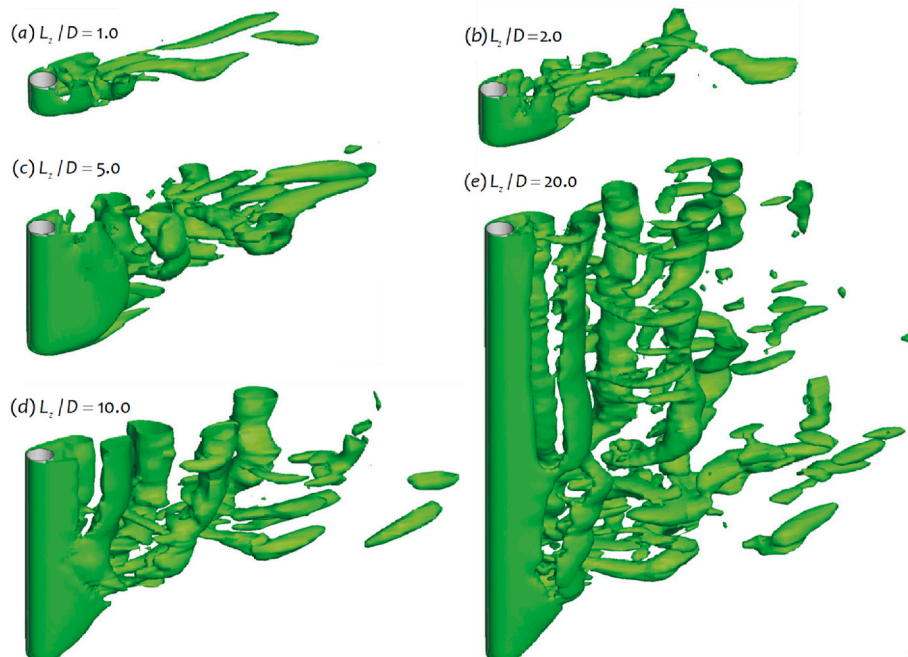

Fig. 8. The iso-surfaces of vortex formation behind the stationary cylinder for different L_Z/D (Zhao and Cheng, 2014).
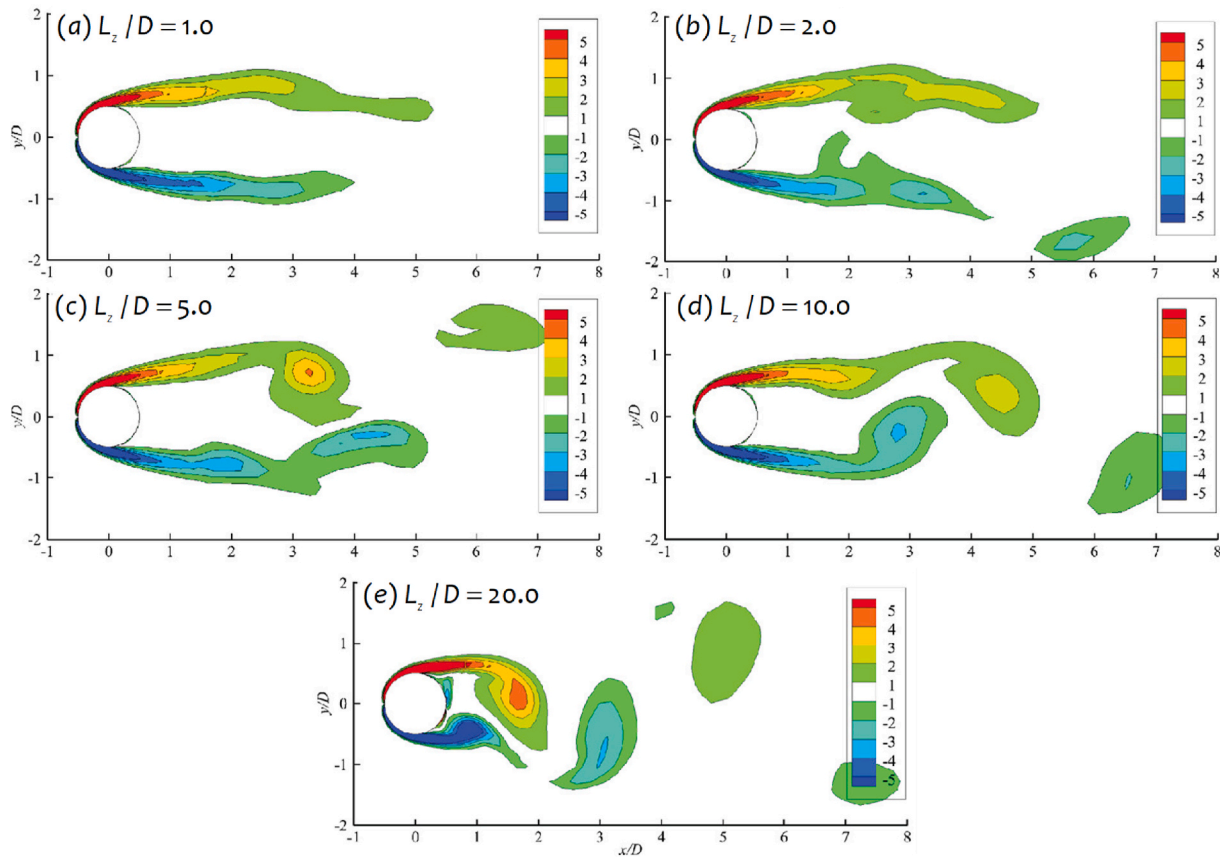
Fig. 9. Contours of vorticity in spanwise direction at the top end of the stationary cylinder for different L_Z/D (Zhao and Cheng, 2014).

2.4. Relationship between Reynolds number and hydrodynamic parameters

A quantitative analysis was carried out by Qu et al. (2013) to investigate the flow around the circular cylinder at low Re (50 − 200) using the fractional step method. The authors found that the base C_P (C_{Pb}) and $C_{L,\,RMS}$ are most sensitive to the domain size, while θ and the wake bubble size were not adversely affected by the domain size. The effect of grid density is more on C_D, followed by $C_{L,\,RMS}$ and the wake bubble size. The C_D value was increased by 16% when the time step was increased from 0.005 to 0.04 s. The authors have found that the frictional component from the total drag reduces with the increase in Re and this may be roughly estimated as $C/\sqrt{Re}$, where $C = 3.21$ and 3.51 for $Re = 50$ and 200, respectively. Similarly, the ratio of the frictional $C_{L,\,RMS}$ to the total C_L decreases as Re is increased roughly as $1.3/\sqrt{Re}$ ($50 \leq Re \leq 200$). Cao et al. (2010) studied the effects of Re and shear parameter (velocity shear flow - β) on St, C_D, C_L, and wake formations. They reported that the Strouhal frequency was constant despite the change in the shear parameter at $Re = 60$ to 1.0×10^3; this agrees well with Sumner and Akosile (2003). The C_D value was nearly unchanged with an increase in the shear parameter for $Re = 60$ to 1.0×10^3 in which C_L is defined as $|C_L| = C_D \times \tan(\theta_0)$ where θ_0 is defined as the degree of motion of the stagnation point.

For $270 \leq Re \leq 10^5$, where progressively more disturbed mode B turns into the only wake pattern, Jiang (2020) proposed a relationship between Re and the time-averaged separation angle ($\overline{\theta}_S$) as $\overline{\theta}_S = 78.88 + 505Re^{-1/2}$ for $270 \leq Re \leq 10^5$. Wu et al. (2004) carried out experiments and numerical simulations to study the separation angles for laminar flow (Re < 280) and proposed an empirical equation for $\overline{\theta}_S-$ Re relationship $\overline{\theta}_S = 95.7 + 267.1Re^{-1/2} - 625.9Re^{-1} + 1046.6Re^{-3/2}$ ($7 \leq Re \leq 200$) and an equation for a marginally small range of Re: $\overline{\theta}_S = 101.5 + 155.2Re^{-1/2}$
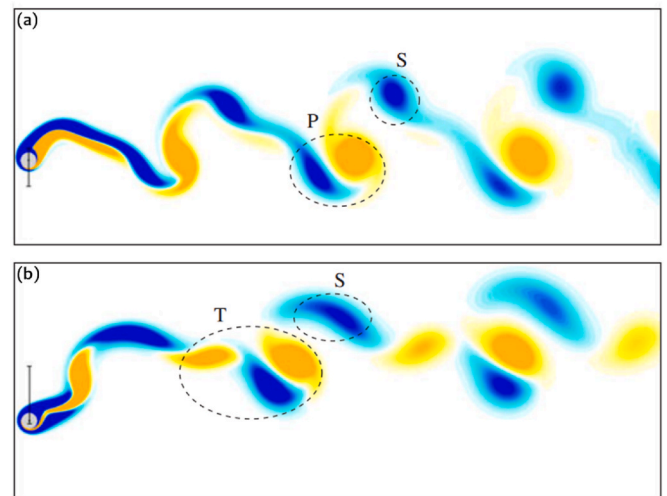

Fig. 10. Iso-contours of vorticity: (a) P + S pattern and (b) T + S pattern. At higher rotational rates, the region of intermediate reduced velocities is dominated by a pattern composed of a pair (P) of vortices couples to a single (S) vortex, and this pattern is referred to as the P + S pattern. A fourth vortical structure appeared at each shedding cycle for intermediate reduced velocities and $\alpha > 2.5$, and as an extension of the P + S pattern, this pattern is referred to as T + S by regrouping the three vortices to form triplet (T) (Bourguet and Jacono, 2014).

($10 \leq Re \leq 200$). Table 4 lists C_D, C_{Pb} and St from some of the recent experimental and numerical results at $Re = 3.9 \times 10^3$. Gerrard (1966a, 1966b) observed periodic oscillations of the vortex shedding at $Re > 100$, which relates to the generation of Karman vortex street.

2.5. Formation of separation bubble behind the cylinder

Lehmkuhl et al. (2014) and Rodríguez et al. (2015) investigated the flow in the range of $2.5 \times 10^5 \leq Re \leq 8.5 \times 10^5$. Wake asymmetries have been discovered in the critical regime, but the wake regains its symmetry and alleviates in the supercritical regime. The asymmetries in critical regimes were due to the formation of a tiny recirculation bubble on one side of the cylinder. As the Re is increased to a sub-critical regime, a similar bubble is formed on the second side of the cylinder, which regains the symmetric pattern. The latest experimental work by Cadot et al. (2015) investigated the dynamics of wake bubble reattachments for the duration of drag crisis (phenomenon in which the C_D drops off suddenly as the Re increases). The authors have reported four highly likely states of the flow around a cylinder in the critical Re regime: (i) no Laminar Separation Bubble (LSB) (#0) (ii)LSB on the bottom side of the cylinder (#1b) (iii) LSB on the top side of the cylinder (#1t) (iv) LSB on the bottom and top sides of the cylinder (#2). #0 denotes no reattachment, #1b and #1t denote reattachment on the bottom and top sides of the cylinder, respectively, and #2 denotes reattachment on either side of the cylinder as shown in Fig. 12. The existence of these states, either on one side or either side, is highly unpredictable. In the critical Re regime, Desai et al. (2020) reported that C_D gradually decreases as Re increases while C_L decreases monotonically as Re increases. They have also observed a two-state (#2) drag crisis in the critical Re regime. The first transition occurs when Re is increased beyond 3.79×10^5, and the flow alternates between #0 and #1b. At Re $= 3.89 \times 10^5$, the flow stabilizes at #1b, and when Re $= 4.10 \times 10^5$, the sporadic LSB arises at the top side of the cylinder, and the flow fluctuates between #1b and #2. When Re $\geq 4.40 \times 10^5$, the flow is steady at #2 and resultant to a drag crisis completion. The investigations by Cadot et al. (2015) and Desai et al. (2020) are in good agreement with Lehmkuhl et al. (2014).

C_D has nearly remained constant throughout several orders of Re, but at the critical Re, C_D drops to almost 1/5th of its earlier value. This phenomenon is called a drag crisis due to the boundary layer reattachment past the cylinder. The experiments by Deshpande et al. (2017) revealed that the reduction in C_D with an increase in Re is not only due to a rise in the base pressure coefficient (C_{Pb}) but also due to the rise in the suction in the upstream shoulder of the cylinder. The incidence of drag crisis was categorised into three sub-regimes: (i) gradual reduction on C_D due to an increase in Re (due to an increase in C_{Pb}, and suction), (ii) rapid decrease in C_D due to an increase in Re (primarily due to a rise in C_{Pb}), and (iii) C_D continuous to decrease with increasing Re (solely due to the rise in the suction). Behara and Mittal (2011) observed a single-stage drag crisis for smooth cylinders while a two-stage drag crisis for a rough cylinder. A positive and negative C_L was observed in the first and second stages of the drag crisis, respectively, for a rough cylinder. The mechanism of C_D reduction during the drag crisis was investigated by Chopra and Mittal (2017) for flow around a circular cylinder at $1.0 \times 10^4 \leq Re \leq 4.0 \times 10^5$. The authors found that the shift of the boundary layer from being laminar to turbulent and the development of LSB are responsible for the drag crisis. It was found that LSB is missing in the sub-critical regime, and as Re increased, the LSB appearance frequency increases. They have proposed an equation to estimate $\overline{C}_D$ in terms of the intermittency factor (I_f) and the mean drag coefficient equivalent to the laminar state ($\overline{C}_{D,Lam}$) and to the turbulent region ($\overline{C}_{D,Turb}$): $\overline{C}_D = I_f \overline{C}_{D,Turb} + (1 - I_f)\overline{C}_{D,Lam}$.

2.6. Effect of gap ratio (G/D) and boundary layers thickness to diameter ratio (δ/D)

The effect of plane boundary in the proximity of circular cylinders has been the topic of intense study. The wall proximity close to the cylinder interferes with the flow properties across the cylinder and alters the related hydrodynamic forces. Insight into these fundamental characteristics is vital in structural design in offshore industry applications. When the cylinder is positioned near the plane boundary, the flow properties over the cylinder are governed by parameters such as the gap-to-diameter ratio (G/D), and the boundary layers thickness to diameter ratio (δ/D), where G is the distance between the plane boundary and bottom surface of the cylinder and δ is the boundary layer thickness where the cylinder center locates.

The effects of the bottom wall on the formation of vortex shedding, wake patterns, and hydrodynamic coefficients have been studied both experimentally and theoretically by many researchers such as Lei et al. (1999), Wang and Tan (2008), Ong et al. (2010), Rao et al. (2013a),
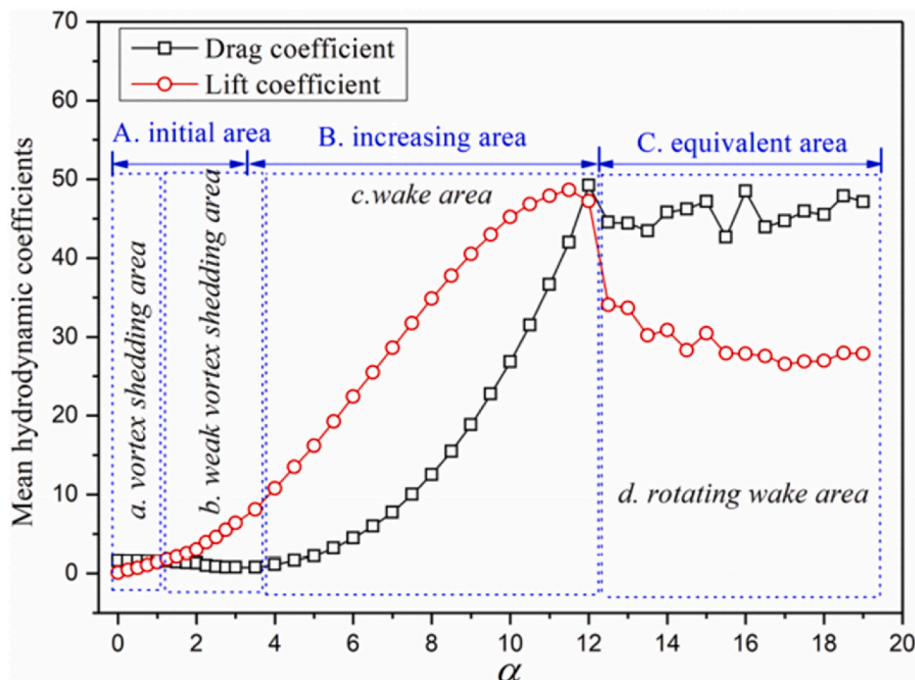

Fig. 11. Variation of mean hydrodynamic coefficients with the rotational rate (Chen et al., 2020).

Zhao (2020), and Zhou et al. (2021).

The flow over a circular cylinder at $G/D = 0.005$ to infinity was numerically investigated by Rao et al. (2013a) for $Re \leq 200$. The authors found that the shift from steady 2D flow to steady 3D flow takes place at $G/D \leq 0.25$. While Jiang et al. (2017b) used 3D DNS to study the flow transition over a cylinder at $G/D \geq 0.3$ for Re up to 325. The authors reported that the hydrodynamic coefficients in the 3D wake regime decrease more when compared to those in the 2D wake regime. At $G/D = 0.4$, for $Re \leq 180$, the wake is dominated by mode A which relatively forms a strong three-dimensionality. Wang and Tan (2008) categorised the G/D into three types based on the vortex shedding patterns: (i) wall-effect free region ($G/D \geq 1.0$), (ii) intermediate region ($0.3 \leq G/D < 1.0$), and (iii) vortex suppression region ($G/D < 0.3$). Similar findings were observed by Zhou et al. (2021) for $Re = 1.5 \times 10^3$ and $G/D = 0 - 2.5$. Zhou et al. (2021) also analysed the variation of St dependence on G/D. The St decreased from 0.25 to 0.192 when G/D increased from 0.369 to 2.5. Ong et al. (2010) carried out numerical studies for flow across circular cylinders close to a flat seabed at high Re (3.6×10^6) using the $k - \varepsilon$ model. They have investigated the effects of Re, G/D, δ and flat seabed roughness on flow. C_D increases as G/D increases for a small G/D and C_D achieving the highest value when G/D significantly increases. The mean friction velocity at the seabed is higher for smaller gaps due to velocities being higher when the gap is small and, as a result, the sediment conveyance on the seabed is much greater for smaller G/D.

A series of experimental investigations in a water channel were carried out by Wang et al. (2013) to study VIV of the cylinder near the wall with $G/D = 0.05 - 2.50$, $V_r = 1.53 - 6.62$ and $m^* = 1.0$. The authors found that, when G/D is larger, the vortices are shed from either side of the cylinder; when G/D is smaller, vortices are shed from the outer side of the cylinder leading to a single side vortex shedding formation. Huang and Sung (2007) and Yoon et al. (2010) found that, when Re increases, the critical G/D decreases to lower values. Sarkar and Sarkar (2010) used LES to investigate the vortex formations and concluded that, for $G/D = 0.25, 0.50, and 1.0$, vortices are shed from either side of the cylinder and the vortex shedding frequency decreases as G/D increases. Li et al. (2017) identified four wake modes: (i) W2S(A) – in this mode, vortices are shed from either side of the cylinder; (ii) W2S (B) – vortices from the inner side of the cylinder are weaker than the outer side; (iii) 1S – no vortices from the inner side of the cylinder; (iv) NS – no vortices from either side of the cylinder.

Tham et al. (2015) reported that the width of the lock-in region increases as G/D decreases and the third branch appears between initial and lower branches at $G/D \leq 0.6$. The wall effects were negligible when $G/D > 0.6$. In contrast, Chung (2016) stated that the width of the lock-in region increases as G/D increases even though the maximum amplitude

of the vibration decreases. Yang et al. (2018) noticed a drag crisis at $G/D \geq 0.50$ for $1.90 \times 10^5 \leq Re \leq 2.7 \times 10^5$. For $G/D \leq 0.25$, C_D decreases than what was observed for large G/D. Zhang et al. (2021) investigated the effect of being near the plane boundary on flow properties around a circular cylinder using DNS for $Re = 350$, $G/D = 0.2 - 1.0$ and $\delta/D = 0$, $0.7, and 1.6$. They demonstrated that G/D and δ/D have a significant effect on hydrodynamic coefficients and pressure distribution. The vortex shedding patterns corresponding to G/D and δ/D are displayed in Fig. 13. As G/D increases from 0.2 to 1.0, the vortex shedding growth from being suppressed to fully developed can be observed in Fig. 11. The vortex suppression is primarily triggered by the interaction between the shear layers formed and the wall (Lin et al., 2009). However, the investigations by Zhao and Cheng (2011) showed that VIV was excited even at the lower $G/D = 0.002$ even though the vortex shedding was totally suppressed. Chen et al. (2019) observed a phase jump between hysteresis at the time of initial and lower branch transition and suggested an equation to find the critical G/D as $(G/D)_{CR} = 0.158 + 0.318(\delta/D)$. It is concluded that the wall effect on the vortex formation decreases as G/D increases. Chen et al. (2021) reported that, for a small gap ratio ($G/D = 0.1$), the anticlockwise vortices are suppressed by the shear flow and only the topside vortices are shed downstream. At higher V_r, the authors have observed a regular shedding of vortices from both sides of the cylinder even though the flow was blocked when G/D is small.

3. Flow past elliptic cylinders

In comparison to the investigations on circular cylinders, numerical and experimental studies on elliptic cylinders are relatively rare. The geometry of elliptical cylinders is characterised by its aspect ratio (AR), which is defined as the ratio of the major axis length (a) to the minor axis length (b) as shown in Fig. 14. The geometry of the elliptical cylinder includes a circular cylinder when $AR = 1.0$ and a flat plate when $AR = 0$. These cylinders are proved to have flow and vorticity alternations around the cylinder as studied by Mittal and Balachandar (1996), Badr et al. (2001), Johnson et al. (2004), Sen et al. (2012), and Bhattacharya and Shahajhan (2016). The physical phenomenon of non-circular cylinders in fluid reveals many complex features in comparison to circular cylinders (Sun and Chwang, 1999). The flow characters are substantially altered when the circular cylinder becomes an elliptic cylinder, and the asymmetry was developed considerably sooner than the circular cylinders (Nair and Sengupta, 1996). A summary of some selected experimental and numerical studies by different researchers is listed in Table 5.

3.1. Effect of aspect ratio (AR), angle of attack (AoA), and Reynolds number (Re)

A parametric study was carried out by Kim and Sengupta (2005) and Kim and Park (2006) using a 2D Navier-Stokes flow solver built based on the SIMPLER method to study the effects of AR, AoA, and Re on C_D, C_L and vortex shedding frequency. Sen et al. (2012) investigated the flow around the elliptical cylinder using the stabilised finite-element method for $Re \leq 40$, $0.2 \leq AR \leq 1.0$ and $0^o \leq AoA \leq 90^o$. At low AoA, a thin cylinder forms a separation bubble near the lagging edge of the cylinder, and as the AoA increases, the location of the separation bubble moves in the direction of the leading edge non-monotonically. For thick cylinders, the effect of AoA is insignificant, and the bubble forms for all AoA, just above the cylinder centre. The authors have concluded that, as Re is increased, the separation bubble of the symmetric cylinder moves upstream whereas, for asymmetric cylinder, the separation bubble moves in the direction of the leading edge.

Faruquee et al. (2007) investigated the effect of AR on the flow features around the elliptic cylinder at $Re = 40$. The wake size was increased as AR increased. C_D also increased with the increase in AR.

Table 4
Literature survey of available numerical results for C_D, C_{Pb} and St for flow over a circular cylinder at $Re = 3.9 \times 10^3$.

Researcher	Methodology	C_D	C_{Pb}	St
Dong et al. (2006)	DNS	—	0.93	0.208
Parnaudeau et al. (2008)	Experiment	1.03	—	0.210
Meyer et al. (2010)	LES	1.05	-0.92	0.210
Ouvrard et al. (2010)	LES	0.94	0.83	0.220
Wornom et al. (2011)	LES	0.99	0.88	0.210
Lysenko et al. (2012)	LES -TKE	0.97	0.91	0.209
	LES - SMAG	1.18	0.80	0.190
Lehmkuhl et al. (2013)	DNS	1.02	-0.93	—
Jee and Shariff (2014)	DES	1.00	0.93	0.214
Luo et al. (2014)	PANS	1.06	0.96	0.201
	DES	1.01	0.89	0.203
Prsic et al. (2014)	LES	0.99	0.88	0.210
Chen et al. (2016)	ILES	0.95	-0.73	—
Gsell et al. (2018)	DNS	0.92	—	—
Jiang and Cheng (2021)	LES	1.03	0.95	0.211

Note: Lysenko et al. (2012) and Luo et al. (2012) adopted two different methodologies in the same paper.
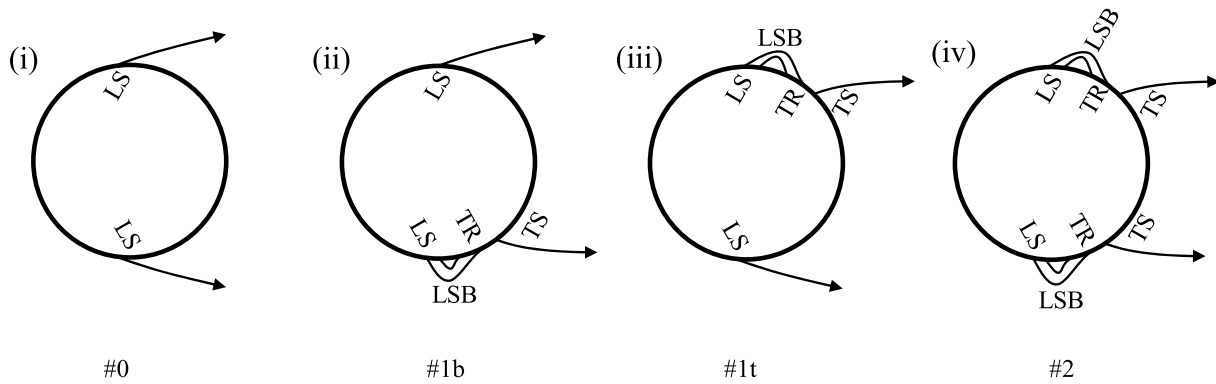
Fig. 12. Representation of flow behind the cylinder displaying (i) no bubble (iii) bubble on the bottom (iii) bubble on top (iv) bubble on both sides of the cylinder. LS, TS, and TR represent Laminar separation, Turbulent Separation, and Turbulent Reattachment, respectively (Desai et al., 2020).

$C_{D,P}$ increased drastically whereas $C_{D,V}$ increased slowly when AR was increased. The author has defined an equation to measure C_D for the variable AR as $C_D = 0.37AR^2 + 0.69AR + 0.465$. Radi et al. (2013) conducted experiments to analyse the variation of St with Re for flow around elliptic cylinders for $100 \leq$ Re ≤ 300 and $0.1 \leq AR \leq 1.0$ where $AR = 0$ *and* 1.0 refer to the flat plat and circular cylinder, respectively. At low Re, Thompson et al. (2014) examined the variation of St for an elliptic cylinder for various ARs as shown in Fig. 15 and determined the vortex shedding frequencies which agreed well with results in Radi et al. (2013). St at the lower ARs values showed different behaviours. The $AR = 0.75$ case has a slightly higher St than the circular cylinder ($AR = 1.0$). Paul et al. (2014) studied the flow properties such as the laminar separation, boundary layer, vortex shedding process, and wake formation behind the elliptic cylinders for varying AoA and ARs. As AR increases, C_L decreases for a given AoA while Re is constant. C_D increases as AR and Re increase when $AoA = 30^o$ but when the AoA is shifted to a higher value, C_D decreases even though AR and Re are increased. It is observed that the vortex shedding frequency increases as Re is increased.

The effect of AR in the range of $0.1 \leq AR \leq 1.0$ for Re $= 100$ on the flow over the elliptic cylinder, which was constrained to move in the CF direction, was investigated by Vijay et al. (2020) using the high-order Spectral/hp element method. The author found that the elliptic cylinder response at $AR = 0.1$ was twice the response exhibited by the circular cylinder and also attained an earlier lock-in. As AR is decreased, the lock-in regimes are found to be gradually moved to smaller V_r. The vortex shedding 2S mode was observed at the beginning of an initial branch where vortices combine near the wake due to the high vibration frequency magnifying the lift force and oscillation response for all AR cases. Yazdi and Khoshnevis (2020) compared the flow wake patterns behind the elliptical cylinder with $AR = 2.0$ for Re $= 3.0 \times 10^4$ versus the circular cylinder. The authors found that the wake characteristics in the near and far wake zones strongly depend upon the axial ratio, and as

the axial ratio rises, the width of the wake shrinks. Rawat (2021) conducted a parametric study to investigate the 2D flow over an elliptical cylinder for $0.5 \times 10^6 \leq$ Re $\leq 3.6 \times 10^6$ and $0.4 \leq AR \leq 1.0$ with three velocity profiles as parabolic, triangular, and plain shear velocities. The authors found that, C_D is reduced by 45% at Re $= 1.0 \times 10^6$ and $AR = 0.6$ for elliptic cylinder compared to a circular cylinder. The maximum C_D was observed for the triangular velocity profile at any AR, followed by the parabolic velocity profile. The plain shear and uniform velocity profiles have almost equal and minimum C_D among the velocity profiles.

Lua et al. (2010) conducted the Digital Particle Image Velocimetry (DPIV) measurements on a 2D elliptical cylinder rotating about its own axis with $\alpha = 0.417, 0.834, 1.67$ *and* 2.5 in a fluid at rest and parallel free stream flow at Re $= 200$ *and* 1.0×10^3. For the cylinder rotating in the stationary fluid, the authors have observed two different vortex shedding patterns depending on the Re. The shed vortices are either disseminated or rotated along with the cylinder, which leads to the vortex suction effect. At low Re, vortices are diffused rapidly, while at high Re, the shed vortices are stronger and are connected to the tip of the cylinder even after a few rotations. As the rotational rate is increased, the cylinder stretches the vortices in the upstream direction leading to the establishment of a hovering vortex. Ruifeng (2015) used the same parameters as Lua et al. (2010) to study the 3D numerical simulations of flow behind the rotating elliptical wing using a quasi-steady model. In addition to rotational rates, the effects of ARs (0.5, 0.25, and 0.167) on the vortex shedding were studied. Ruifeng (2015) observed that at larger ARs, the streamwise vortices are as strong as spanwise vortices. However, at a smaller ARs, the spanwise vortices are attached to the spanwise vortices stemming from the formation of a sophisticated wake structure. As the rotational speed rises, the high-pressure region on the upper side of the cylinder turns into a low-pressure zone at a small ARs. The drawback of the quasi-steady model fails to predict the correct aerodynamic properties at higher rotation speeds due to the loss of
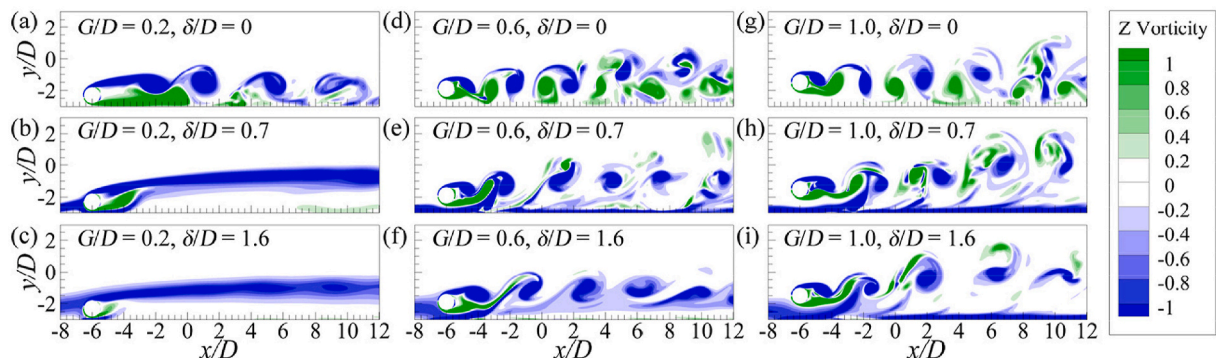

Fig. 13. Time history of non-dimensional spanwise vorticity contours for various G/D and δ/D for Re $= 350$ (Zhang et al., 2021).
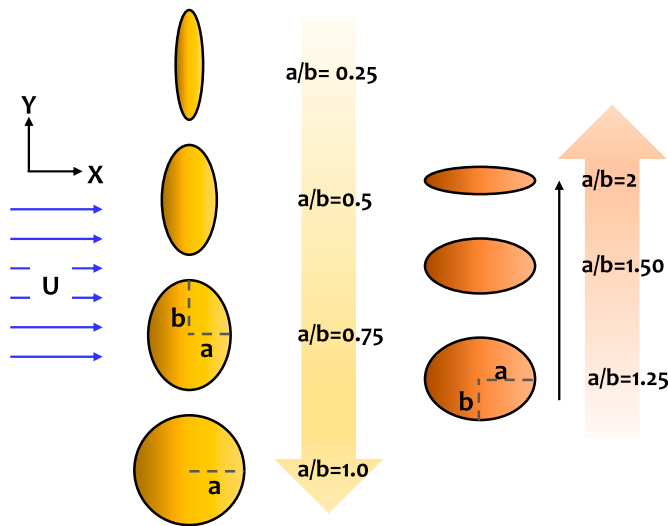
Fig. 14. Examples of elliptic cylinders based on the aspect ratio (*AR*) ranging from 0.25 to 2.0. Two extremity configurations are flat plate and circular cylinder when $AR = 0.001$ and 1.0, respectively.

periodicity in the wake formation. The author attributed that the change of vortex shedding process ultimately led to the creation of hovering vortices at higher rotational rates, as witnessed by Lua et al. (2010). Hargreaves et al. (2014) found that the vortex shedding is easily subsidised at the lower Re = 400 after a few cycles of rotation because of the vortex suction effect. Vortices are defined with the two edges at higher Re = 1.0×10^3 and 2.0×10^3. Vortices at higher Re are rotated with the body. The flow features are highly dependent on the tip-speed ratio (Rossby number-is the ratio between the tangential speed of the tip of a cylinder and the actual free stream speed) and less on Re when the elliptic cylinder is rotating in a uniform flow stream. When the tip speed rises, the vortex shedding pattern converts from a periodic shedding to a quasi-shedding pattern and finally to a hovering vortex.

An experimental investigation was carried out by Lee (2004) to study the flow over the elliptic cylinder. The author has limited the orientation to 0°. However, Subburaj et al. (2018) extended the work of Lee (2004) to study the effect of *AoA* and *AR* proximity to the free surface on flow patterns and hydrodynamic forces for Re = 180. At *AoA* = 45°, the authors found the vortices shedding close to the free surface while they move away for *AoA* = −45° and *AoA* = 90°. It was stated that the elliptic cylinder with *AoA* = 90° experienced the largest C_D while *AoA* = 45° experience the lowest C_D and highest C_L. Akbari and Price (2000) conducted numerical investigations to study the effect of *AoA*, frequency of oscillation, *AR* and location of pitch axis. It was found that the frequency of oscillation has a significant effect on the wake formations. At higher frequency oscillations ($f* = 1.0$), the rotational motion of the ellipse governs the periodic formation of the leading and trailing edge vortices. When the pitch axis is shifted to the quarter chord from the middle chord, the establishment of stronger leading- and trailing-edge vortices leads to much more complex and unsteady wake formations. At the mean *AoA* (0°), a well-organised vortex street formation was observed, whereas for 30°, wide, complex wake formations were observed. Numerical investigations of the rotationally oscillating elliptical cylinder have been studied by Alawadhi (2015) at $50 \le Re \le 150$ with $10° \le AoA \le 60°$. As the *AoA* increases, C_D is increased substantially due to the increased low-pressure region behind the cylinder. When the oscillation frequency matches with the vortex shedding frequency (i.e., as a lock-in occurs), $\overline{C}_D$ and $C_{L, RMS}$ attain their maximum and minimum values, respectively. They found that as Re is increased, $\overline{C}_D$ decreases while $C_{L, RMS}$ increases. The authors have concluded that *AoA* has a significant effect on the formation of vortices behind the cylinder. Leontini et al. (2015) observed three modes (modes A, B, and

QP) as shown in Fig. 16 in the wake of an elliptical cylinder which was observed in the wake of a circular cylinder by Blackburn et al. (2005). Alongside the three modes, another two new relevant modes were found: (i) long-wavelength mode (mode $\widehat{A}$) similar to mode A and (ii) unstable mode (mode $\widehat{B}$) at $AR > 1.75$ with similar time-space symmetries to mode B. Rao et al. (2017) investigated the wake of elliptic cylinder transitions of 2D and 3D at low *AoA* ($\le 20°$) for Re = $100 - 500$ and $AR = 1.0 - 4.0$ with the Floquet stability analysis.

In Fig. 16, the vortex formations of modes A, B, and QP are quite comparable and are in accordance with their equivalents observed in the wake of a circular cylinder. The first two vortices of mode $\widehat{A}$ has the identical structure to Mode A but has a different structure from the third vortex (circled with dashed line) to more downstream. Mode $\widehat{B}$ has a different configuration but shares the same time-space equilibriums to mode B. The modes QP and QPL are shown at a random stage since they have a complex Floquet multiplier (Leontini et al., 2015).

Fonseca et al. (2013) conducted a series of detailed experiments in a vertical hydrodynamic tunnel to determine the Strouhal frequency of the flow past elliptical cylinders with Re being varied up to 2.0×10^3. For Re = 500, the authors have observed that the vortex shedding frequency of the thinner elliptical cylinder is higher than that of the elliptical cylinder with AR close to 1.0 due to the formation of thinner wake downstream of the cylinder. For Re < 500, the vortex shedding frequencies of elliptical cylinders followed a linear correlation whereas for Re < 500, they did not observe any correlation between the vortex shedding frequencies. Experimental work by Zhao et al. (2019) reported a lock-in phenomenon that was dominated by VIV oscillations for an elliptic cylinder $860 \le Re \le 8050$, $1.5 \le V_r \le 14.0$ and $0.67 \le AR \le 1.50$. They also found two separated lock-in regimes for the cylinder at $AR = 0.67$ (first lock-in occurred at $4.0 \le V_r \le 4.4$ when the Strouhal frequency matched with natural frequency and second lock-in occurred at $7.0 \le V_r \le 11.6$ (when the amplitude of the vibration was discovered to be similar to that observed in the lower branch of the circular cylinder) and for $AR \ge 0.80$ lock-in happened only at single reduced velocity $4.6 \le V_r \le 12.0$. While comparing with the circular cylinder, the lock-in occurred substantially at low V_r as *AR* increased above unity. They observed that the vibration responses and on-set lock-in were substantially altered when the *AR* was changed, and the FIV responses are controlled by VIV instead of the transverse galloping. Based on Hall theory (Hall, 1984), Gallardo et al. (2016) reported that flow structures for *AR* greater than 0.67 resemble circular cylinders whereas $AR < 0.34$ exhibit the flattened flow structures instead of 3D flow structures and produced counter-rotating spanwise vortices that occur near the tips of the ellipse.

Raman et al. (2013) have presented the functional relationships between critical *AR*, C_D and, *St* for flow over elliptic cylinders for various *AR* at Re in the range of 50–500. Zhai et al. (2018) established a functional relationship between the separation angle and *AR* for flow around the elliptical cylinder in the laminar flow region. Perumal et al. (2012) investigated the influence of blockage ratio, Re and length of the channel for steady and unsteady flows using the lattice Boltzmann method in the laminar flow regime. Chen and Yen (2011) reported that the axis ratio has an insignificant effect on the resonant frequency, but it has a major effect on the resonant amplitude. The smaller *AR*, greater the incidence of resonant amplitude. Yoon et al. (2016) studied flow properties such as C_D, C_L, *St*, and stagnation point as a function of *AoA* ($0° \le AoA \le 90°$) for Re ($20 \le Re \le 100$) and *AR* using the direct-forcing/fictitious domain (DF/FD) method. As *AoA* increases, the $\overline{C}_D$ increases and the rate at which it increases is higher when Re is increased. The C_L attains a maximum value for *AoA* below 45° for $20 < Re < 60$ and *AoA* above 45° for $70 < Re < 100$. The authors found that the stagnation point was strongly dependent on *AoA* and less dependent on Re. The *St* decreased as the *AR* increased and the rate at which the *St* decreased was faster for higher Re. Yazdi and Khoshnevis (2020) reported larger values of kurtosis and skewness factors due to the existence of vortices in the top and

Table 5

Summary of experimental and numerical studies of flow around the elliptical cylinder including Reynolds number (Re), methodology, Aspect Ratio (AR), Angle of Attack (AoA). C_D, C_L, C_F and C_P represents drag, lift, friction, and pressure coefficients, respectively. C_{DP}, C_{DF} are the coefficient of drag due to pressure and friction, respectively. $\overline{C}_{\overline{C}_P}$ and $C_{P,\ RMS}$ are time-averaged and RMS pressure coefficients, respectively. Θ and St are separation angle and Strouhal number. L_r and L_F are recirculation length and formation length of vortex shedding.

| Researchers	Re	Methodology	AR	AoA	Measurement
Johnson et al. (2003)	$75 \sim 175$	Numerical	0.01, 0.25 and 1.0	0°	C_D, and St
Khan et al. (2004)	$1.0 \times 10^2 \sim 1.0 \times 10^5$	Numerical	$0.01 \sim 1.0$	0°	C_D, C_{DP} $C_{DF,}$ Θ and shear stress
Kocabiyik and D'Alessio (2004)	1.0×10^3	Numerical	0.50	30° and 90°	C_D, and C_L
Kim and Park (2006)	400, 600	Numerical	0.2, 0.4 and 0.6	10°, 20° and 30°	$\overline{C}_D$, $C_{L,RMS}$, and St
Faruquee et al. (2007)	40	Numerical	$0.3 \sim 1.0$	0°	$\overline{C}_{\overline{C}_P}$, $C_{P,\ RMS}$, St
Ibrahim and Gomaa (2009)	$5.6 \times 10^3 \sim 4.0 \times 10^4$	Experimental and Numerical	$0.25 \sim 1.0$	$0^\circ \sim 150^\circ$	C_D
Sarkar and Sarkar (2009)	1440	Numerical	2.0, 3.0, and 4.0	0°	$\overline{C}_D$, $\overline{C}_L$, $\langle \overline{u} \rangle / U_\infty$ and $\langle \overline{v} \rangle / V_\infty$
Fonseca et al. (2013)	$2.0 x 10^3$	Experimental	$0.33 \sim 0.67$	0°	C_D, C_L, St, and mean velocity
Radi et al. (2013)	$100 \sim 300$	Numerical	$0 \sim 1$	0°	St
Paul et al. (2014)	$5 \sim 40$	Numerical	$0.1 \sim 1.0$	$0^\circ \sim 90^\circ$	St, and critical Re
Thompson et al. (2014)	$50 \sim 200$	Numerical	$0 \sim 1.0$	0°	C_D, and St
Leontini et al. (2015)	$250 \sim 550$	Numerical	$1.0 \sim 2.4$	0°	L_F, and transition of modes
Griffith et al. (2016)	200	Numerical	$1.0 \sim 6.0$	0°	$\overline{C}_D$, $\overline{C}_L$, St, and amplitude of vibration
Soumya and Prakash (2017)	$50 \sim 200$	Numerical	$0.5 \sim 1.0$	0°	$\overline{C}_D$, $\overline{C}_L$, St, and L_r
Lua et al. (2018)	200	Numerical	$0.0625 \sim 1.0$	$0^\circ \sim 90^\circ$	C_D, C_L, streamwise and lateral surface pressure distribution
Sooraj et al. (2018)	$240 - 3.4 \times 10^4$	Experiment	–	–	C_D
Subburaj et al. (2018)	180	Numerical	2.0 and 4.0	-45°, 45° 90°	C_D, C_L, and St
Wang et al. (2019a)	150	Numerical	$1.0 \sim 2.5$	$0^\circ \sim 180^\circ$	$\overline{C}_D$, $\overline{C}_L$, and $\overline{C}_M$
Karlson et al. (2020)	$10 \sim 100$	Numerical	$0.4 \sim 1.4$	0°	L_F
Kushwaha et al. (2020)	100	Numerical	1.0, 1.33, and 2.0	0°	$C_{D,\ RMS}$, $C_{L,\ RMS}$, $C_{LP,\ RMS}$, and $C_{LV,\ RMS}$
Shi et al. (2020)	150	Numerical	$0.2 \sim 1.0$	$0^\circ \sim 90^\circ$	$\overline{C}_D$, $C_{L,RMS}$, St, L_F, and wake patterns
Vijay et al. (2020)	100	Numerical	$0.10 \sim 1.0$	0°	$\overline{C}_D$, $\overline{C}_L$, C_P and oscillation amplitude
Durante et al. (2021)	$100 \sim 1.0 \times 10^4$	Numerical	$0.1 \sim 0.40$	$0^\circ \sim 90^\circ$	C_L, St, and flow regimes
Rawat (2021)	$0.5 \times 10^6 \sim 3.6 x 10^6$	Numerical	$0.4 \sim 1.0$	0°	C_D, C_P, and C_F
Wan et al. (2021)	100	Numerical	$0.25 \sim 4.0$	0°	C_D, C_L, and vibrational amplitude
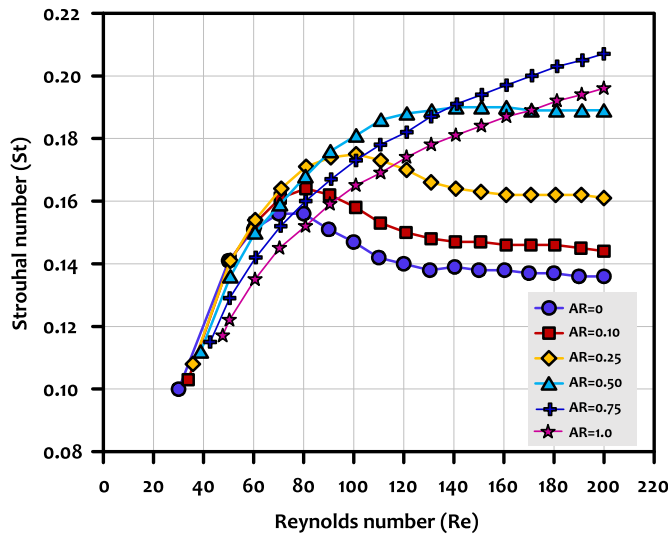
Fig. 15. Variation of Strouhal number with Re for different *AR* with 2D simulations. *AR* = 0 results were taken from 3D simulations (recreated from Thompson et al., 2014).

bottom surfaces of the cylinder. It was concluded that as *AR* increases, the vortices weaken, C_D decreases, and *St* increases.

Lu et al. (2018) carried out numerical investigation on the 2D rotating elliptic cylinder at Re = 200. They stated that the hydrodynamic and moment coefficients are highly non-linear to the rotational rate and *ARs*. The different wake topologies behind the elliptic cylinder were divided into four categories (i) steady, (ii) quasi-steady, (iii) periodic, and (iv) aperiodic flows. Kumar and Tiwari (2021) distinguished the flow wake as four types similar to Lu et al. (2018) for $150 \leq$ Re $\leq$ 250 and $0.5 \leq AR \leq 2.0$. The author has investigated the effect of shear parameters on wake formations using the Hilbert Huang transformation and recurrence analysis. The negative vorticity termed as "hovering vortex" was observed above the elliptic cylinder, which was also found from the studies carried out by Ruifeng (2015) and Naik et al. (2018). Naik et al. (2017) used the immersed boundary method (IBM) to investigate the effects of *AoA* = 0.1 *to* 1.0 and $\alpha = 0.4$, 1.0, *and* 1.5 at Re = 100. It was found that, as the cylinder rotates, the trailing edge

aids the flow while the leading edge deters the flow, which shows a significant effect on the hovering vortex formation. The authors found that the Strouhal frequency is a strong function of rotational rate. The drag force decreased with increasing *AR* up to 0.7 and then increased. As the rotational rate increased, the drag coefficient/force reduced while the lift coefficient/force increased. The C_L decreased with an increase in *AR*. Naik et al. (2018) studied the influence of linear shear flow on the development of the hovering vortex behind the rotating elliptic cylinder. The formation of the hovering vortex is restrained at the modest shear. The authors also noticed that the lift coefficient/force linearly increased with shear, whereas the vortex shedding frequency behaved independently of the shear parameter.

Franzini et al. (2009) experimentally studied the transverse vibrations of an elliptic cylinder at $2.0 \times 10^3 \leq$ Re $\leq 8.0 \times 10^3$ and mass ratio (m^*) of 2.5. The authors have divided the response of the cylinder into three branches as a function of reduced velocity and reported that the peak amplitude of vibration of the elliptical cylinder experiencing VIV was significantly lower than the circular cylinder. A numerical investigation was carried out by Yogeswaran et al. (2014) to study VIV of the undamped elliptic cylinder at $60 \leq$ Re ≤ 140, $m^* = 10$ and $0.7 \leq AR \leq 1.43$. The authors have divided the response of cylinder into seven regimes as (i) steady-state (SS), (ii) desynchronisation I (DSI), (iii) quasi-periodic initial branch, (iv) periodic initial branch, (v) periodic lower branch, (vi) quasi-periodic lower branch, and (vii) desynchronisation II (DSII). In comparison, Wu et al. (2021) used the immersed boundary multi-relaxation-time lattice Boltzmann flux solver proposed by Shu et al. (2014) to investigate VIV of elliptic cylinders for $0.7 \leq AR \leq 1.5$ and $4.0 \leq V_r \leq 10.0$. The authors have divided VIV of the elliptic cylinders into a desynchronisation regime, initial and lower branches. The vibration in the transverse direction dominates VIV of elliptic cylinders (Fang et al., 2009). Hasheminejad and Jarrahi (2015) studied the effects of *AR* (0.5, 1.0, and 2.0) and *AoA* on vibrational characteristics of VIV for two DOF at $60 \leq$ Re ≤ 400 and proposed a quasi-dynamic vibration control method based on vibration mechanism.

Johnson et al. (2001) categorised the flow regimes behind the elliptic cylinder into six regimes based on Re and *AR*, namely (i) steady flow (Re = 40 and *AR* = 0.5), (ii) Karman-type vortex (Re = 75 and *AR* = 0.5), (iii) Symmetric wake (Re = 125 and *AR* = 0.5), (iv) transitional shedding (Re = 150 and *AR* = 0.5), (v) steady secondary shedding (Re = 175 and *AR* = 0.5), and (vi) unsteady secondary shedding (Re = 250 and *AR* = 0.5). They have observed that the formation of
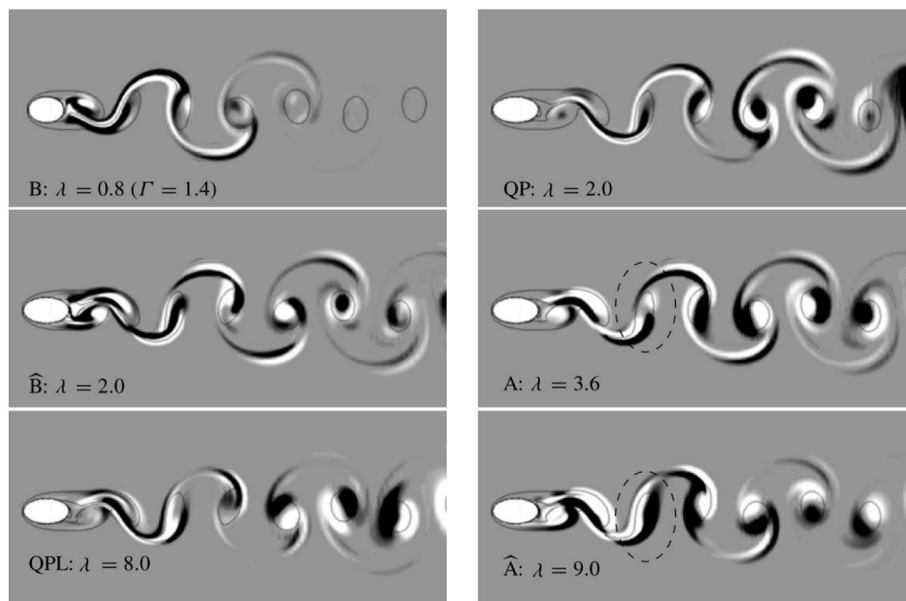

Fig. 16. Contours of vortices for different modes.

secondary shedding results in the change of C_D and *St*. Paul et al. (2016) categorised the flow behind the elliptic cylinder into seven flow regimes based on the relationship between fluid characteristics and *AR*, *AoA* and Re. Leontini et al. (2018) reported various categories of vortex shedding regimes comprising the period-doubling and P + S at different *AoA*. At *AoA* = 90°, they observed a broad scale of the large oscillation amplitude. The effects of *AR* and *AoA* on flow properties were investigated by Shi et al. (2020), based on 2D numerical analysis at Re = 150, *AR* = 0.25 − 1.0 and 0° ≤ *AoA* ≤ 90°. The authors have observed three distinct wake patterns: pattern I: steady wake occurring at *AR* < 0.37 and *AoA* < .2.5°; pattern II: Karman wake followed by steady wake observed at *AR* ≥ 0.35 − 0.67 and for all *AoA*; and pattern III: Karman wake followed by the secondary wake at *AR* ≤ 0.67 and *AoA* > 52° as shown in Fig. 17. The minimum and maximum values of $\overline{C}_D$ were observed for the pattern I and III, respectively, while for pattern II, the $\overline{C}_D$ is identical to that of the circular cylinder. Durante et al. (2021) divided the flow behind the elliptic cylinder into three regimes (i) steady regime as shown in Fig. 18, (ii) periodic regime as shown in Fig. 19, (iii) chaotic regime based on the lift force and vortex shedding patterns in the wake of the cylinder for $100 \leq$ Re $\leq 1.0 \times 10^4$, $0° \leq AoA \leq 90°$ and *AR* = 0.1 *and* 0.4. Furthermore, the periodic regime was divided into monochromatic, non-monochromatic, quasi-periodic, and sub-harmonic regimes based on the formation of vortices behind the cylinder. Fig. 20 presents the vorticity field generated by thick (*AR* = 0.4) and thin (*AR* = 0.1) ellipse at Re = 5.0×10^3. The authors stated that, when Re is increased, the periodic regimes turn into chaotic regimes.

Sourav and Sen (2017) investigated the effects of damped (in the transverse direction) and undamped (in the transverse direction and 2-DoF) free vibrations of rigid elliptic cylinders for $50 \leq$ Re ≤ 180 and *AR* = 1.11. The transverse oscillations are mostly periodic, while the damping of 0.044 removes the quasi-periodicity. A secondary hysteresis is formed by the flow. Sen and Mittal (2017) investigated the far wake topology of an elliptical cylinder for Re = 200, *AoA* = 0° *to* 20°, and *AR* = 0.1, 0.5, *and* 0.8. The associated frequencies along the centreline were studied by using the power spectrum analysis at various points of the transverse velocity. The authors found that the second frequency shows a non-monotonic variation while the primary frequency decays with the incidence. Kumar et al. (2018) carried out similar work to Sourav and Sen (2017) for Re = 100, *AR* = 0.5, and $1.0 \leq V_r \leq 8.0$. The lock-in is initiated at $V_r = 3.5$ and severely shortened at $V_r = 4.2$ with

the frequency of oscillation attaining the maximum and minimum value, respectively. At the onset of lock-in (at $V_r = 3.5$), the vortex shedding takes place with the maximum strength, thus $C_{L,RMS}$ reaches the maximum, and finally, the scale of the maximum transverse displacement becomes the largest (= 0.0653*D*). On the contrary, at the closure of lock-in ($V_r = 4.2$), the strength of vortex shedding decay weakens $C_{L,RMS}$ and the magnitude of the maximum transverse displacement. At $V_r = 4.3$, vortices are suppressed where the free shear layers become straight and the steady state regains as shown in Fig. 21.

3.2. Effect of gap ratio (G/D) and boundary layers thickness to diameter ratio (δ/D)

The elliptic cylinder near the moving wall has several practical applications such as cells in blood vessels, beads in bioreactors, automation industry, oil and gas industry, and others. The walls shear stress, and the insignificant quantity of flow between the wall and the cylinder suppress the vortex shedding that draws the interest of researchers such as Jin et al. (2015) and Zhang and Shi (2016). Yazdi and Khoshnevis (2018) experimentally investigated the interference of wake with the boundary layer and how this interference affects the wake characteristics using the hot-wire anemometry. They found that *St* increases as *G/D* increases and then stays independent of δ/*D*. They also stated that the stream-wise mean velocity profiles and turbulence intensity were strongly reliant on Re and *G/D*.

The effect of *G/D*, *AR* and Re on the flow around the elliptic cylinder in the vicinity of the moving wall on the force coefficient and *St* was analysed by Wang et al. (2018b) for Re = 200 *and* 400 using LES based on LBM. The effects of *AR*, gap ratio and Re on force coefficients, flow filed and Strouhal number were analysed. It was found that decreasing *G/D* and *AR* suppresses the vortex shedding, while an increase in Re effectively eases the complete suppression of vortex shedding as shown in Fig. 22. From Fig. 22(ii), for the small G/D = 0.1, the shear layer of the cylinder combines with the shear layer of the wall surface, rolling altogether. As the flow rate is small in this gap ratio, the time to form vortices at the lower side of the cylinder increases. Thus, the vortices shed from the upper and lower sides of the cylinder are merged further downstream. For Re ≤ 150, Zhu et al. (2020) investigated 2D flow across the elliptic cylinder near the bottom moving wall with G/D = 0.1 *to* 5.0. The authors found a significant effect of near wall on the
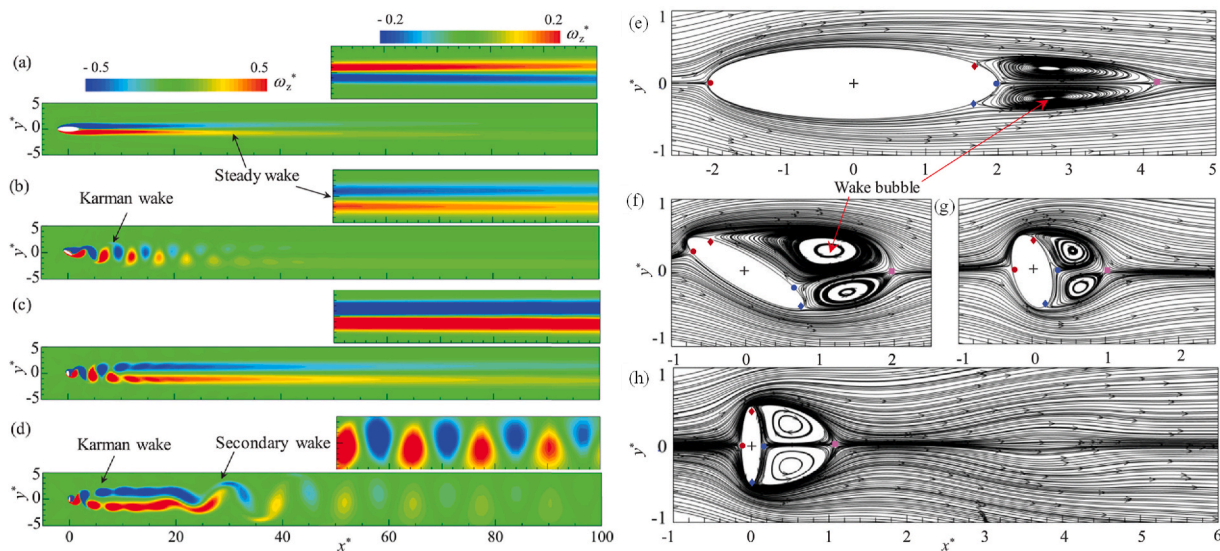

Fig. 17. Instant vorticity contours and time-mean streamlines for (a) and (e) pattern I: Steady wake at *AR* = 0.25 and *AoA* = 0°; (b) and (f), (c) and (g) pattern II: Karman wake followed by steady wake observed at *AR* = 0.25 and *AoA* = 30°, *AR* = 0.50 and *AoA* = 75°; and (d) and (h) pattern III: Karman wake followed by the secondary wake at *AR* = 0.25 and *AoA* = 90° (Shi et al., 2020).
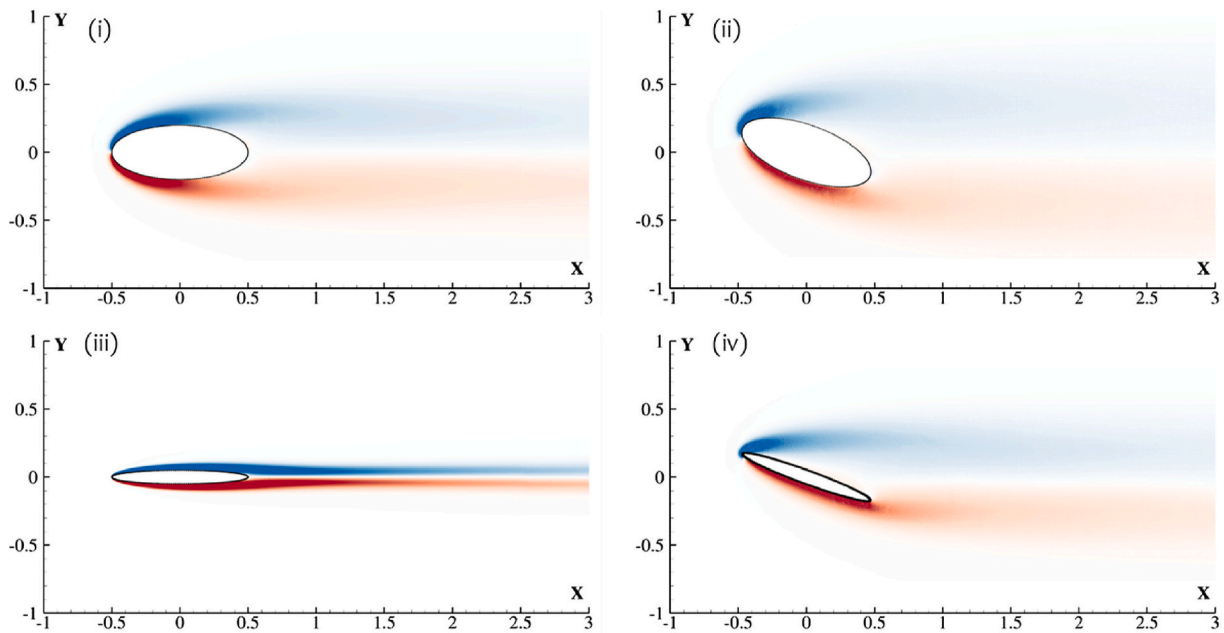
Fig. 18. Contours of vortices for the steady-state regime at (i) Re $= 0.2 \times 10^3$, $AR = 0.4$ and $AoA = 0^o$, (ii) Re $= 0.1 \times 10^3$, $AR = 0.4$ and $AoA = 20^o$, (iii) Re $= 3.0 \times 10^3$, $AR = 0.1$ and $AoA = 0^o$ (iv) Re $= 0.2 \times 10^3$, $AR = 0.1$ and $AoA = 20^o$ (Durante et al., 2021).
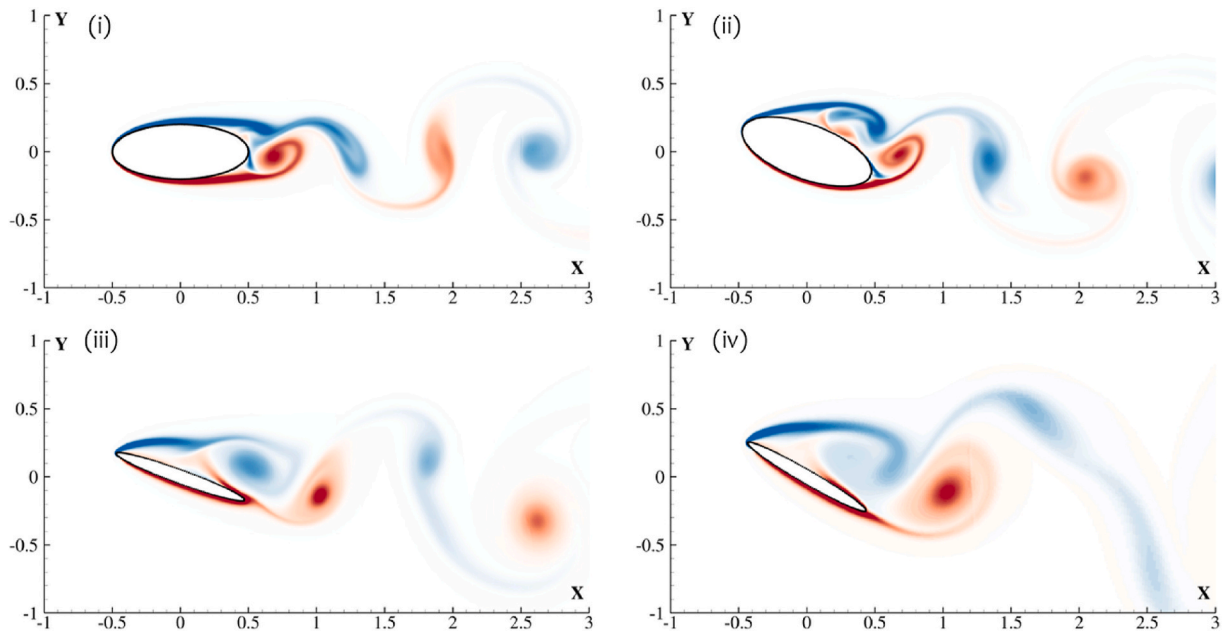

Fig. 19. Contours of vortices for the periodic regime at (i) Re $= 2.5 \times 10^3$, $AR = 0.4$ and $AoA = 0^o$, (ii) Re $= 3.0 \times 10^3$, $AR = 0.4$ and $AoA = 20^o$, (iii) Re $= 1.4 \times 10^3$, $AR = 0.1$ and $AoA = 20^o$ (iv) Re $= 0.9 \times 10^3$, $AR = 0.1$ and $AoA = 30^o$ (Durante et al., 2021).

wake formations at small G/D. Due to the decay of wall suppression effect, $\overline{C}_D$ increases steadily as G/D increases at a given Re. Zhu et al. (2021) investigated 3D flow over the elliptic cylinder with $AR = 0.5$ near the bottom moving wall with gap ratios $G/D = 0.1, 0.2, 0.3$ *and* 0.4 for $100 \leq$ Re ≤ 200. The authors have observed distinct wake conversion circumstances for each case, as summarised in Table 6.

4. Flow past a bio-mimetic cylinder

Numerous researchers have widely studied the flow around the circular cylinders to investigate the flow characteristics causing VIV. The challenging task is to control the vortex shedding. There are two different ways to decrease the effect of FIV on the cylinder: (i) controlling vortex shedding through adding up objects on/close proximity to the cylinder, (ii) altering the geometric shapes of the cylinder. In this paper, the authors have emphasised reviewing the investigations of flow around cylinders with different geometric shapes. These arrangements over the cylinders will increase the complexity of vortex shedding around the cylinder, with the aim of reducing the drag and lift forces, and hence suppressing VIV (Lam and Lin, 2008a). Biomimetic is the scientific method of learning new principles and processes based on a systematic study, observation and experimentation with living animals and organisms, being a source of inspiration and a guide in the development of new techniques to solve engineering problems.
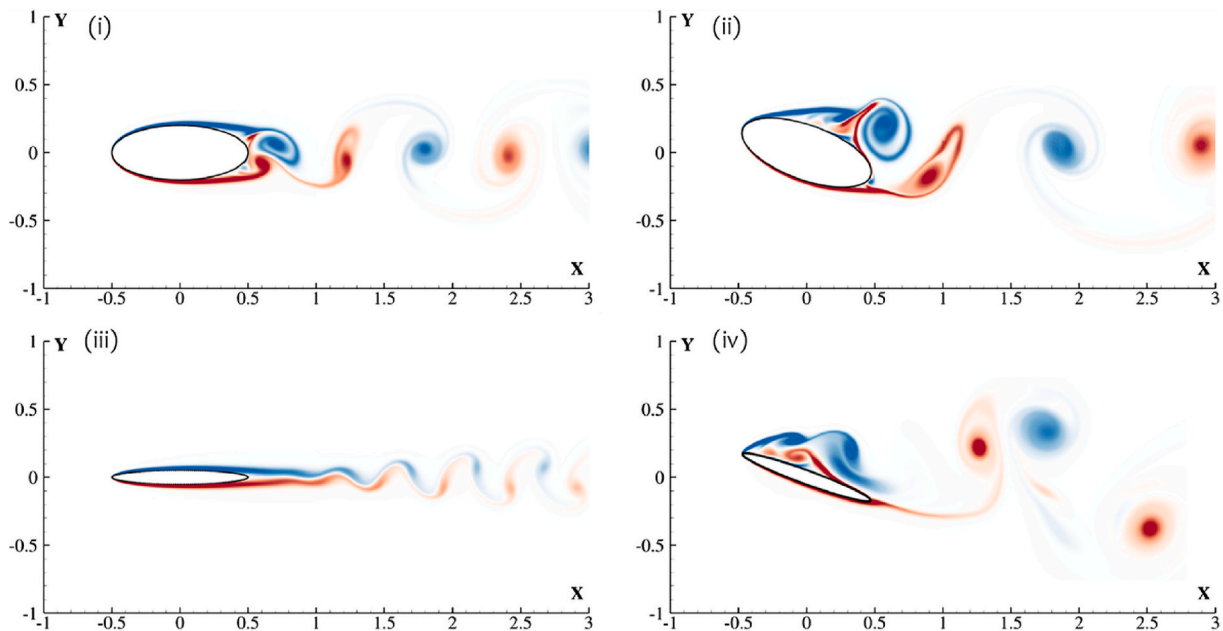
Fig. 20. Effect of *AR* and *AoA* on shear layer interaction at Re $= 5.0 \times 10^3$. (i) *AR* = 0.4 and *AoA* = 0°, (ii) *AR* = 0.4 and *AoA* = 20°, (iii) *AR* = 0.1 and *AoA* = 0° (iv) *AR* = 0.1 and *AoA* = 20° (Durante et al., 2021).
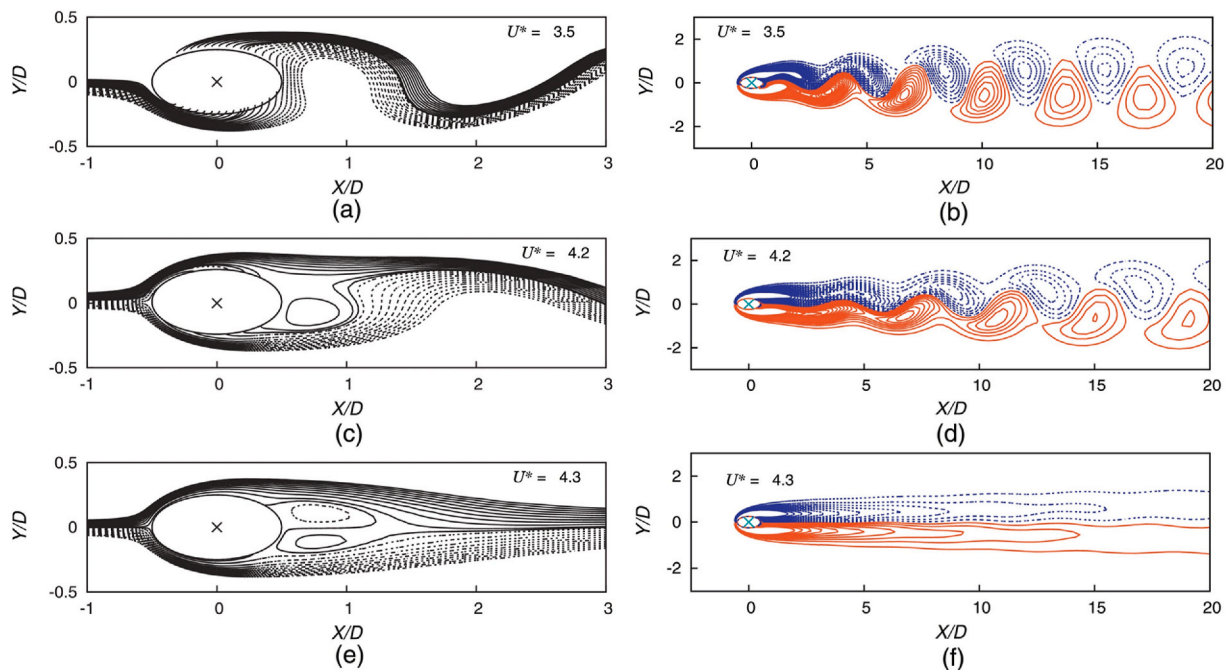

Fig. 21. Transverse oscillations of the elliptic cylinder for Re $= 100$, $m^* = 10$ and *AR* $= 0.5$. (a, c, e) streamlines for $V_r = 3.5$, 4.2, *and* 4.3, respectively, and (b, d, f) vorticity for $V_r = 3.5$, 4.2, *and* 4.3, respectively (Kumar et al., 2018).

The new geometric shapes of the cylinder are generated either by twisting the circular/elliptical cylinder or by using biomimetic principles. The circular or elliptical cylinder, which is twisted along the spanwise direction and whose diameter is varied sinusoidally, is called a symmetric wavy (SW) cylinder. This SW cylinder can be twisted to generate a new shape called Helically Twisted Elliptical Cylinder (HTE), as shown in Fig. 23. Some of the researchers who have carried out experimental and numerical assessments of the wavy and twisted cylinders are Ahmed and Bays-Muchmore (1992), Bearman and Owen (1998), Keser et al. (2001), Lam et al. (2004a), Nguyen and Jee (2004), Zhang et al. (2005), Lam and Lin (2008b), and Naudascher and Rockwell

(2012). The geometric shapes based on biomimetic principles refer to the cylindrical shapes developed based on the nature-inspired designs evolved over time, e.g., the whiskers (vibrissae) of harbor seal (phocids) as these creatures have unique sense and ability to track their prey by minute disturbances using vibrissae instead of visual and aural sense, see, Renouf and Gaborko (1982), James and Dykes (1978), Dehnhardt and Kaminski (1995), Hanke et al. (2010), Choi et al. (2012). The geometry of Harbor Seal Vibrissae (HSV) is presented in Fig. 24.
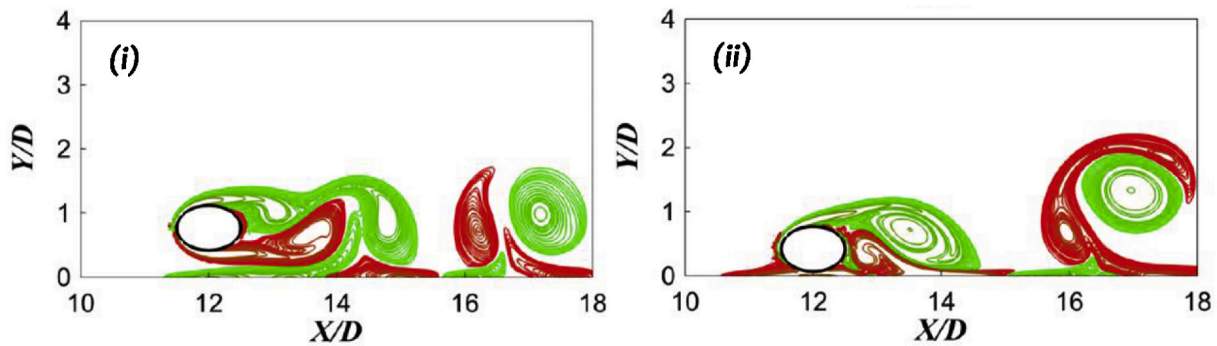
Fig. 22. Instant vorticity fields for (i) Re $= 200$, $AR = 0.7$ and $G/D = 0.6$, (ii) Re $= 400$, $AR = 0.7$ and $G/D = 0.1$ (Wang et al., 2018b).

4.1. Symmetric wavy (SW) cylinder

Experimental research to investigate the behaviour of symmetric wavy (SW) cylinders at the high Re is fairly limited due to difficulties and high costs engaged in executing the experiments. Early in the 1990s, Ahmed and Bays-Muchmore (1992) experimented by examining the flow patterns and pressure field across the SW cylinder at $Re = 2.0 \times 10^4$ based upon the mean diameter (D_m) of the cylinder. Owen et al. (2000) used the flow visualisation technique to study the flow behind the SW cylinder. They concluded that Karman vortex shedding is well suppressed, and the wake width is varied periodically along the span of the cylinder. In addition, Owen et al. (2001) performed experiments over a circular cylinder, SW cylinder and hemispherical bumps on the circular cylinder to gauge the drag and VIV amplitudes. They found that the vortex shedding is suppressed and C_D is reduced up to 47% and 25% for SW cylinder and bumps on the cylinder, respectively, compared to a circular cylinder. The authors have concluded that the sectional C_D at the node is more significant than the saddle, and 3D flow separation was observed due to the spanwise pressure rise.

Experiments were conducted by Lam et al. (2004a) to investigate the effect of surface waviness on C_D and C_L at Re $= 2.0 \times 10^4 - 5.0 \times 10^4$. They found that C_D in comparison to the circular cylinder is reduced by 20% depending upon the degree of obliqueness ($a^2/\lambda D$) of the SW cylinder, where a and λ are amplitude and wavelength, respectively. However, the *St* value remains as 0.2, like a circular cylinder. Lam et al. (2004b) found that the typical vortex formation length of the SW cylinder is greater than that of circular cylinder, which results in the decrease of C_D and suppression of VIV. They noticed that the shear layers are extended along the spanwise direction at saddle points, whereas they are shrunk and accelerated at nodes. Due to the increased turbulent intermingling, the wake reveals traits of incomprehensible turbulence. It was also observed that the spanwise flow is moved to the nodal plane

from the saddle plane. 3D flow characteristics of a SW cylinder at Re $= 3.0 \times 10^3$ were investigated experimentally by Zhang et al. (2005). The near-wake structure and streamwise vortices were substantially modified due to the existence of waviness on the SW cylinder, resulting in the formation of spanwise periodicity behind the cylinder. Lee and Nguyen (2007) investigated the C_D turbulence intensity, mean velocity, and profiles of vortices in the wake of the SW cylinder at Re $= 2.0 \times 10^4 - 5.0 \times 10^4$. It was discovered that the SW cylinder reduces C_D when compared to the circular cylinder. This observation agrees well with Lam et al. (2004a).

The effect of wavelength plays a vital role in controlling the vortex formations behind the cylinder. Besides the wavelength, the cylinder amplitude plays a significant role in regulating the formation of vortices near the wake of SW cylinder. Lam and Lin (2008a) conducted numerical simulations using LES at Re $= 3.0 \times 10^3$ and $1.136 < \lambda/D_m < 3.333$ to investigate the effect of wavelength ratios. The SW cylinders reduced C_D by 18% compared to a circular cylinder at $\lambda/D_m = 1.90$ and C_L was nearly suppressed. They have also observed the formation of 3D free shear layers due to wavy surfaces, which were more stable than 2D free shear layers which rolled up into matured vortices downstream of the cylinder. They found that the wave amplitude to wavelength ratio (a/λ) plays an important role in defining the 3D vortex formation near the wake of the SW cylinder, rendering a considerable impact on suppressing the lift fluctuations and FIV. Fig. 25 compares the free shear layer enhancement disparity and vortex formation lengths for circular and SW cylinders. The spanwise vortices contours of SW cylinders in the saddle and nodal planes are distinctly stretched in the downstream direction compared to the circular cylinder.

Recently, Lin et al. (2016) extended the work of Lam and Lin (2008a) and have taken numerical analysis for large wavelength ratios for the very first time. They found an optimal $\lambda/D_m = 6.06$ in the subcritical regime and a significant decrease in C_D and C_L by 16% and 93%, respectively at $\lambda/D_m = 6.06$ for SW cylinder compared with the circular cylinder at the subcritical regime. Lin et al. (2016) pinpointed the flow regimes into three types based on λ/D_m, namely (i) regime I for $\lambda/D_m < 6.06$, (ii) regime II for $\lambda/D_m = 6.06$, and (iii) regime III for $\lambda/D_m > 6.06$. Recently, Nam and Yoon (2022) investigated the effect of geometry waviness on the elliptic cylinder with $0.5 \leq AR \leq 1.0$ at Re $= 100$ for $1.0 \leq \lambda/D_m < 8.0$. The authors have found that the as AR becomes small, the effect of waviness on in C_D and C_L becomes weak for long λ/D_m. They also observed that the *St* remains smaller than smooth circular cylinder regardless λ/D_m.

Lam and Lin (2008b) investigated the effects of wavelength λ and wave amplitudes (a) on the flow close to the wake of the SW cylinder at Re $= 100$ and 150. The authors observed that the 3D free shear layers from the SW cylinder are harder to roll into the vortex, resulting in a long vortex length formulation than the circular cylinder.

In continuation to Lam and Lin (2008b), a series of 3D numerical simulations with combinations of wave amplitude (a/D_m) and wavelength (λ/D_m) have been carried out by Lam and Lin (2009) at Re $= 100$.

Table 6
Flow regimes patterns for flow over an elliptic cylinder in the vicinity of bottom moving wall for $100 \leq Re \leq 200$, $0.1 \leq G/D \leq 0.4$ and $AR = 0.5$. Wake patterns B, C denotes 2D wake patterns for B, and C. Wake pattern D' denotes 3D wake patterns (Zhu et al., 2021).

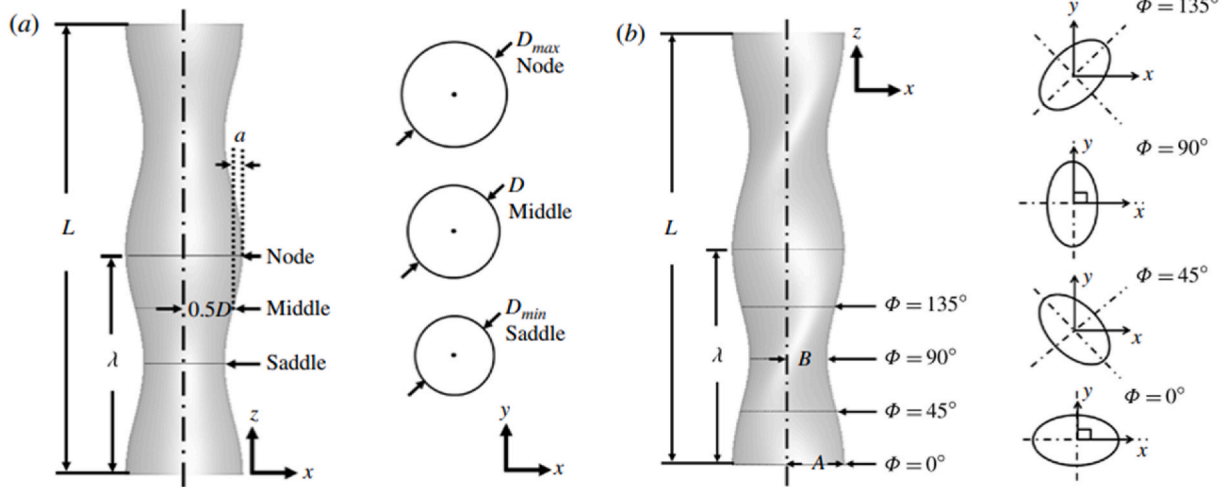| Gap ratio	Reynolds number	Flow regimes
0.1	Re $= 100$	3D steady
	Re ≥ 125	Wake pattern D'
0.2	Re ≤ 120	2D steady
	Re $= 121$	Wake pattern C
	$122 \leq$ Re ≤ 130	Modified mode C
	Re ≥ 140	Chaotic pattern
0.3	Re ≤ 145	Wake pattern C
	$150 \leq$ Re ≤ 155	Travelling Wave mode
	Re ≥ 160	Squiggly Travelling Wave mode
0.4	Re ≤ 125	Wake pattern B
	$135 \leq$ Re ≤ 170	Modified mode A
	Re ≥ 180	Near-wake 2D

Fig. 23. The geometric shape of (a) Symmetric wavy (SW) cylinder, (b) Helically twisted elliptical (HTE) cylinder (Jung and Yoon, 2014).
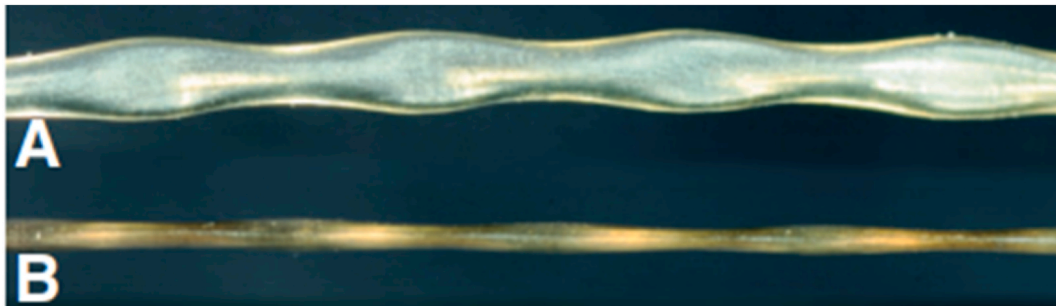

Fig. 24. Harbor Seal vibrissae structure (A) front view (B) side view (Hanke et al., 2010).

The authors presented the optimal λ/D_m for which the maximum reduction in C_D and C_L occurs, and this λ/D_m depends on Re. Three wavelength regimes were identified within a range of $1.0 \leq \lambda/D_m \leq 10.0$ based on the wake formations and force properties, as illustrated in Fig. 26. For Re = 150, the highest possible C_D reduction is about of 21.5% for $a/D_m = 0.175$ and $\lambda/D_m = 2.5$. Xu et al. (2010) investigated the flow behind the SW cylinder with compressible flow conditions using LES at Re = 2.0×10^5. Their results concluded that, due to the
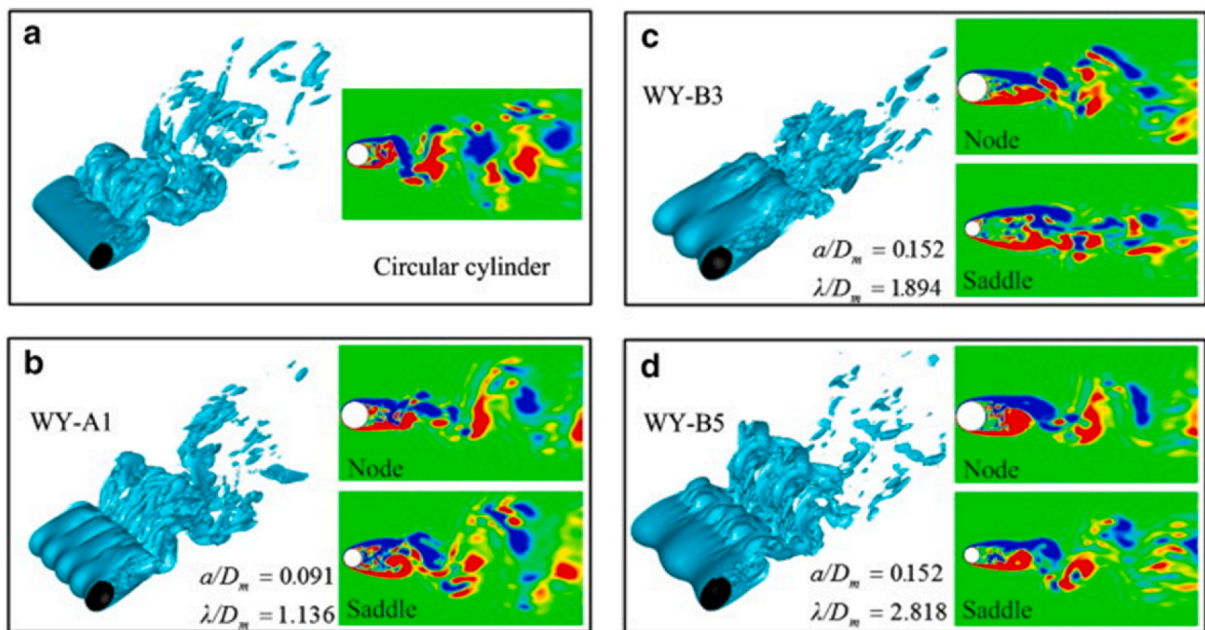
Fig. 25. 3D vortex formations and vorticity along the spanwise direction at the saddle and nodal planes are shown for circular and SW cylinders (Lam and Lin, 2008a).

waviness effect, the hydrodynamic coefficients are reduced when compared to a circular cylinder. The waviness effect of the SW cylinder on the forced convective heat transfer was investigated by Ahn et al. (2009) at $Re = 300$ with three different wavelengths ($\pi/4, \pi/3, \pi/2$). The authors found that the SW cylinder with $\lambda = \pi/2$ has a larger time- and total-surface averaged Nusselt number ($\langle\langle\overline{Nu}\rangle\rangle$) than the circular cylinder. In contrast, $\lambda = \pi/4$ and $\pi/3$ have the smallest Nu number than the circular cylinder. They conclude that the heat transfer rate is higher for SW cylinder than circular cylinder because of the larger surface area exposed to the heat transfer.

4.2. Helically twisted elliptical cylinder (HTE)

The Helically Twisted Elliptical cylinder (HTE), as shown in Fig. 23

(b) is developed by rotating the elliptical cylinder along the spanwise direction. The effect of the HTE cylinder on flow characteristics at subcritical regime ($Re = 3.0 \times 10^3$) using LES was investigated by Jung and Yoon (2014). The free shear layers of the twisted cylinder are elongated more than SW and circular cylinders. Subsequently, the elongated free shear layers from the body of the cylinder and in the wake of vortex shedding form a weak vortical strength that directly reduces C_D and C_L. They found that the HTE cylinder reduces C_D by 5% and 13% to SW and circular cylinders, respectively, and C_L is reduced by 95% when compared to the circular cylinder. The authors also investigated the effect of aspect ratio ($1.25 \leq AR \leq 2.25$) and stated that the mean C_D drops to a minimum value at $AR = 1.44$ and then increases as AR increases. They noted that the HTE cylinder's vortex formation length reduces as Re increases, which is applicable to the circular cylinder as
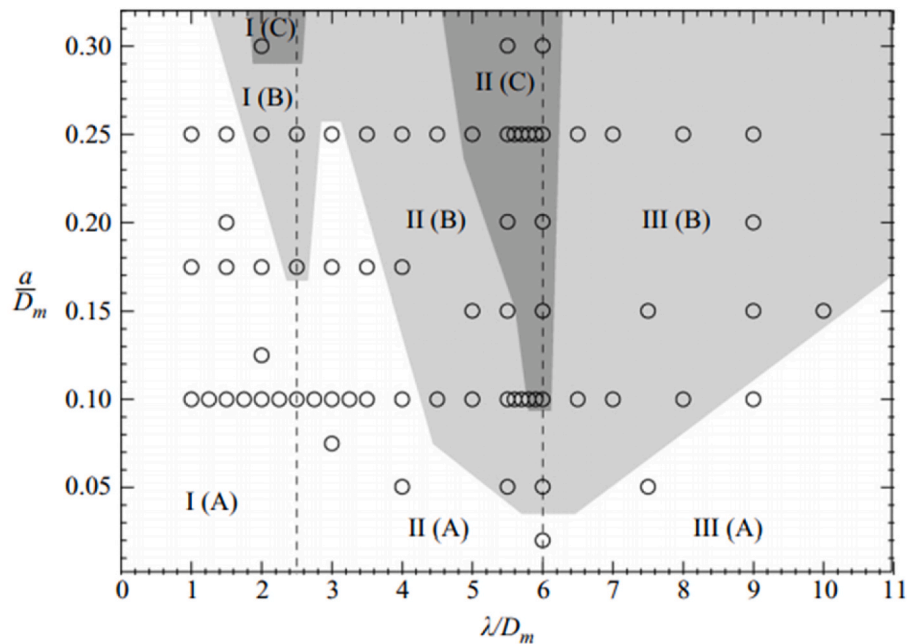
(a)
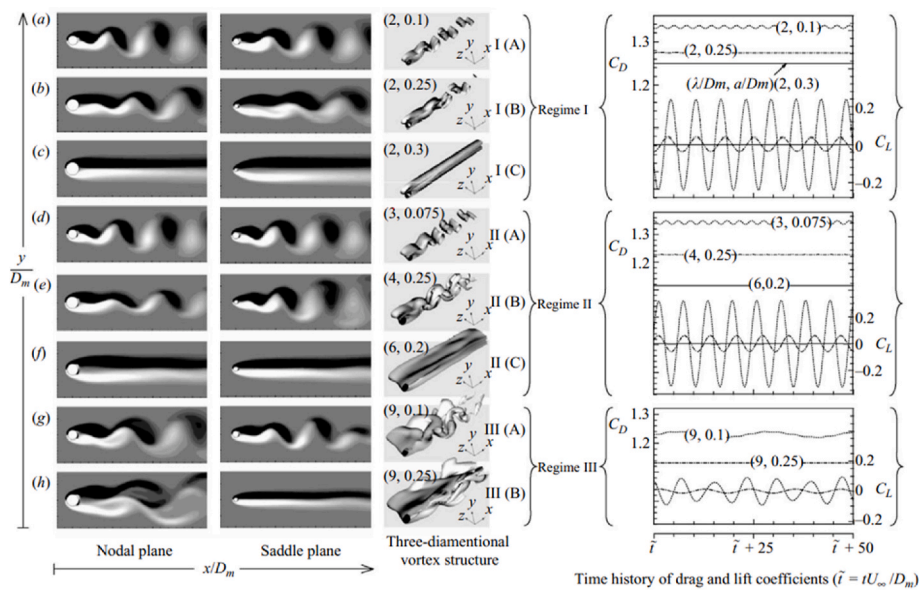
(b)

Fig. 26. Flow patterns (a) Flow pattern regimes (b) Flow patterns for SW cylinders for different a/D_m and λ/D_m at Re = 100 (Note: Symbol ($\circ$) in (a) presents each SW cylinder) (Lam and Lin, 2009).

well. The comparison of flow behind circular, SW, and HTE cylinders is presented in Fig. 27.

Wei et al. (2016) investigated the HTE in the laminar regime (Re = 100) and confirmed the effectiveness of reducing force coefficients due to the twisted shape of the cylinder. They have also observed multi-frequency oscillations from the time history of C_D, which resulted in the harmonic behaviour of power spectra. Interestingly, the HTE cylinder produces a longer vortex formation length in laminar and subcritical regimes, which support suppressing the force coefficients. The flow patterns from these studies agreed well with the findings from Zhang et al. (2005). A parametric study for combinations of AR and helical spanwise wavelength (λ) was carried out by Kim et al. (2016). It was found that at Re = 100, the optimum HTE configuration ($AR = 1.3$ and $\lambda = 3.5D$) reduces C_D by 18%, while at $Re = 3.9 \times 10^3$, the optimum configuration ($AR = 1.4$ and $\lambda = 4.0D$) reduces C_D by 23% more than a circular cylinder. The effect of Re ($3.0 \times 10^3 \leq Re \leq 1.0 \times 10^4$) on the flow properties of HTE was analysed by Yoon et al. (2019). It was found that as Re increases, the HTE shows greater efficacy in reducing C_D and C_L. Yoon et al. (2018) examined the forced convection heat transfer around HTE and the effect of Re in laminar flow regime ($60 \leq Re \leq 150$) and Prandtl number (Pr) = 0.7. In this Re range, the Strouhal number (St) of the HTE cylinder is 4%–7% less than the circular cylinder. The $\langle\langle\overline{Nu}\rangle\rangle$ of the HTE cylinder decreases from 1.2% to 2.8% in the Re range, in comparison with the circular cylinder.

4.3. Asymmetric wavy (ASW) cylinder

Yoon et al. (2017) proposed a new geometrical form by implementing an asymmetry to the symmetric wavy cylinder, as demonstrated in Fig. 28. The flow characteristics of the asymmetric wavy (ASW) cylinder were investigated in the subcritical regime. The authors identified that the ASW disturbances on the cylinder reduce C_D and C_L more than SW and circular cylinders. The vortex formation length by the ASW cylinder was significantly longer than SW and circular cylinder. It was asymmetrically distributed along the spanwise direction. The longer vortex formation length also demonstrates that the ASW disturbances on the cylinder surface also decrease C_D and C_L more than the SW cylinder. The effect of asymmetric waviness on convection heat transfer was studied by Moon et al. (2019) at $Re = 3.0 \times 10^3$ who concluded that the ASW cylinder produces the smallest Nu number than SW and circular cylinders.

In extension to Yoon et al. (2017), a new cylinder with double wavy (DW) disturbance was proposed by Yoon et al. (2020) with two optimal wavelengths $\lambda/D_m = 2.0$ and $\lambda/D_m = 6.06$ from Lam and Lin (2009) and Lin et al. (2016), respectively, for geometry disturbances. The authors have noticed a more reduction in C_D and C_L than SW and circular cylinders. In the near wake region, the circular cylinder forms large Karman vortices, as presented in Fig. 29(a). However, the shear layers from SW and DW cylinders are significantly elongated towards downstream, as shown in Fig. 29(b and c). Consequently, the vortices roll-up of the shear layers delayed downstream, which leads to the suppression of vortex shedding near the wake and recurs in the distant wake of the downstream of SW and DW cylinders.

4.4. Variable pitch helically twisted elliptical cylinder

Another geometric form called the variable pitch helically twisted elliptical (VPHTE) cylinder as illustrated in Fig. 30 was developed by Moon and Yoon (2020) by combining the HTE cylinder proposed by Jung and Yoon (2014) and ASW cylinder proposed by Yoon et al. (2017). Moon and Yoon (2020) conducted a parametric study by varying the variable pitch (VP) of the VPHTE cylinder at $Re = 3.0 \times 10^3$. The vortex formation length of the VPHTE cylinder was longer than the HTE and circular cylinders, which supported lowering the C_D by 4.1% and 16.7% when compared to HTE and circular cylinders, respectively. The $C_{L,RMS}$ of the VPHTE was reduced by 96.2% than the circular cylinder. As the VP of the VPHTE cylinder increases, the difference between the pressure at the front and rear of the cylinder decreases, leading to a greater reduction in C_D. The vortex formation in the wake of circular, HTE, and VPHTE cylinders are shown in Fig. 31. Yoon and Moon (2021) assessed the performance of VPHTE on the forced convection heat transfer at $Re = 3.0 \times 10^3$ by using LES. The VPHTE cylinders produced smaller $\langle\langle\overline{Nu}\rangle\rangle$ than SW and circular cylinders. Based on the temperature contours distribution, the authors have noticed the extended shear layers and delay of the vortex shedding process due to the disruptions from the geometric shape.

4.5. Bio-inspired cylinder

Amongst the flow control methods, the biomimetic principle is widely used in different applications and can be found from Bechert et al. (2000), Fish and Lauder (2006), Bhushan (2009), Wu (2011), Choi
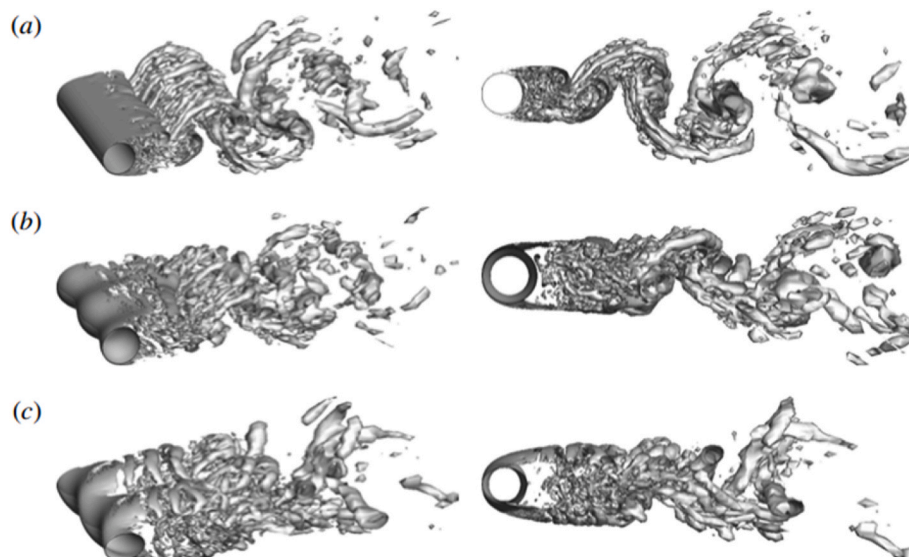

Fig. 27. Top view (left column) and side view (right column) of the vortex formations behind the (a) Circular, (b) SW, and (c) HTE cylinders at $Re = 3.0 \times 10^3$ (Jung and Yoon, 2014).
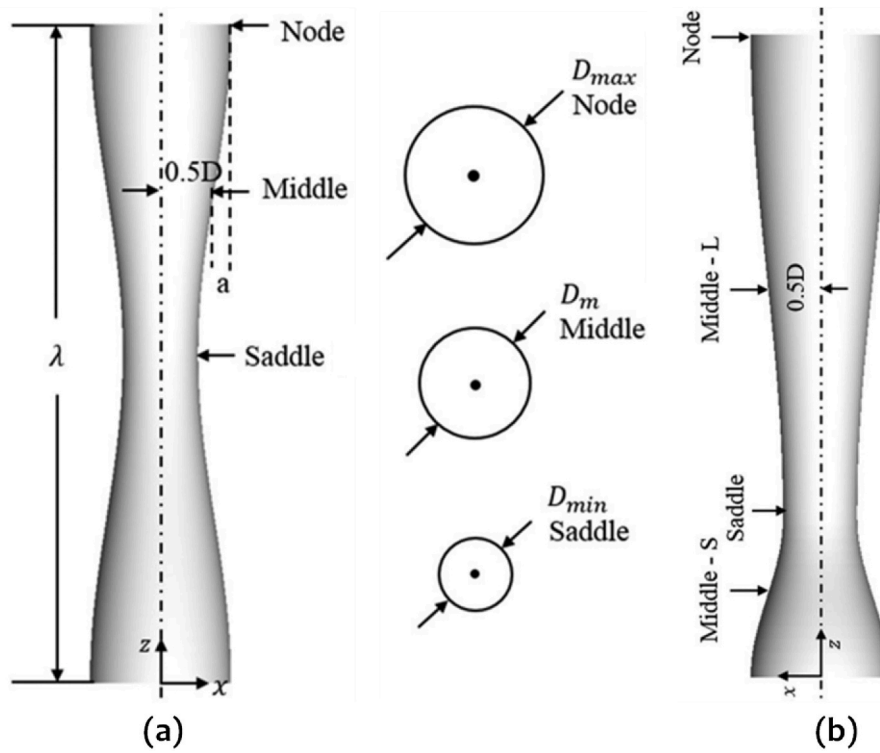
Fig. 28. The geometric shape of (a) Symmetric wavy (SW) cylinder, (b) asymmetric wavy (ASW) cylinder (Yoon et al., 2017).

et al. (2012), Triantafyllou et al. (2016), and Chu et al. (2021). The harbor seals have demonstrated remarkable skill to orient themselves and successfully hunt in turbid sea conditions. Harbor seal whiskers with their distinctive geometry significantly suppress the drag and lift fluctuations. The Harbor seal whiskers morphology can be modelled as elliptical cross-section with periodically replicating the chronological order of peaks and troughs along the spanwise direction (Fish et al., 2008). Schulte-Pelkum et al. (2007) stated that as the seal is near the
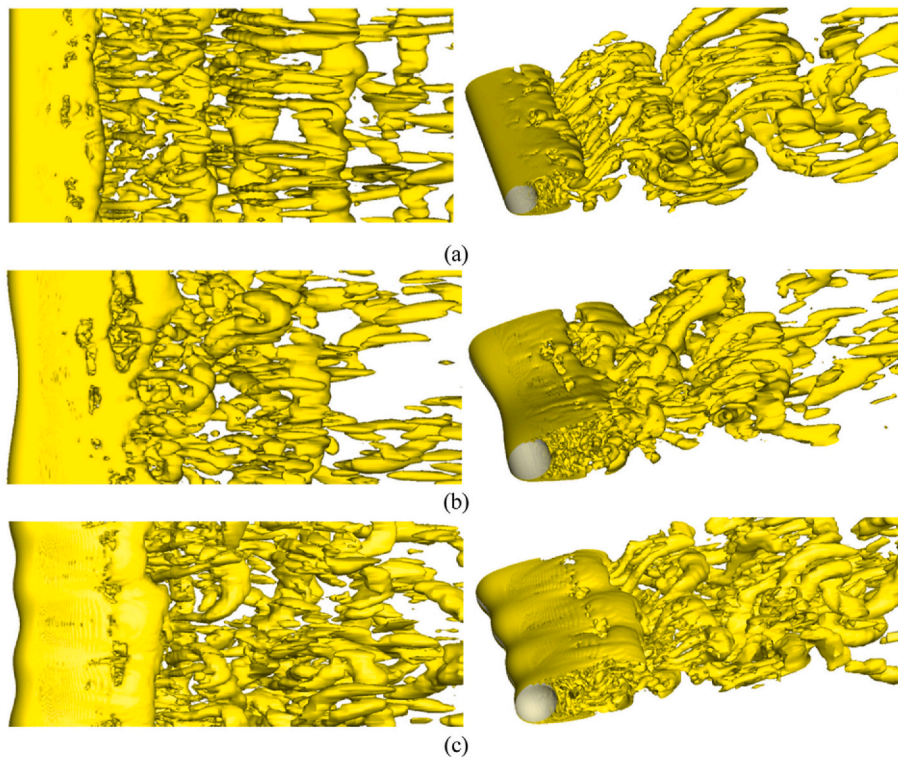

Fig. 29. Left: top view and right: perspective view of the iso-surface vortex shedding around (a) circular cylinder, (b) SW cylinder, and (c) DW cylinder at $Re = 3.0 \times 10^3$ (Yoon et al., 2020).

wake furthest in the wake of its upstream predator, the vibrissae reveal increased structural vibration. Though the vibrissae are exposed to their own VIV, it remains static during the high-speed movement in uniform flow.

Hanke et al. (2010) presented seven parameters to define the undulating 3D form of seal whiskers, as shown in Fig. 32. The peak is exemplified by major, minor axes radius, and angle of incidence as a, b, *and* α respectively. Likewise, the trough major, minor axes radius, and angle of incidence as k, l, *and* β respectively and λ_P represents the wavelength between two peaks or troughs. Witte et al. (2012) constructed a whisker model based on the measurement from 13 adult HSW's and found differences in certain geometric parameters, particularly in the angle of incidence α *and* β. Rinehart et al. (2017) studied the morphology of 27 seal whiskers (Harbor and elephant seals). They stated that the length parameters of whiskers agreed well with the statistical analysis framework by Hanke et al. (2010). Nevertheless, the angle of incidence of elliptical cross-sections falls between -5° to +5° and follows Gaussian distribution with no clear orientation. Asadnia et al. (2015) and Beem et al. (2012) developed a sensor motivated by harbor seal whiskers to detect oncoming vortex frequency and proved the possibility for future use as wake detectors.

Hans et al. (2013) investigated four different HSV cylinders on their force reduction ability and stated that undulation amplitudes on both the axes are required to have the highest possible reduction in C_D and C_L. This is because when undulations are being introduced, the vortex patterns and braids are broken, resulting in a considerable reduction in the hydrodynamic forces. They claimed that the angle of incidence has a comparatively weak impact on C_D reduction. In a recent study, Liu et al. (2019) studied the geometric model that is based upon values for the parameters presented in work performed by Rinehart et al. (2017). Investigation indicates that the undulations in opposite directions must alternate with each other along the spanwise direction to attain the maximum C_D and C_L reduction. Modifying the wavelength and amplitude showed that HSV cylinder morphology suppresses the fluctuating lift to a larger extent. However, the authors did not provide any methodology and significant variations in the undulation of morphology, and this remains vague on which geometric characteristics or combination of characteristics are essential with the hydrodynamic force reduction.

Hanke et al. (2010) investigated the undulated surface of HSV and showed that the structure efficiently changes the vortex shedding pattern in the wake of whiskers and decreases the vibrations. The

authors found that the mean C_D is reduced by 40% and the lift fluctuations by 94% when compared to the circular cylinder. Miersch et al. (2011) examined the hydrodynamics of the HSV cylinder and discovered that the vibrissae could differentiate the vortex shedding frequencies produced upstream by its prey. Experimental and numerical analyses were carried out by Witte et al. (2012) to investigate the flow properties in the wake of the HSV cylinder at $Re = 0.3 \times 10^3$ *and* 0.5×10^3. They found that the vortex core of the HSV cylinder is substantially different from the circular cylinder as it is developed further downstream, and the collapse of the vortex happens quicker than the circular cylinder. Matz and Baars (2012) carried out 3D numerical investigations for HSV, elliptical and circular cylinders at $Re = 0.3 \times 10^3$ *and* 0.5×10^3. They confirmed that no Karman vortex street was observed in the wake of the HSV cylinder. Undulations on the minor axis have a considerable impact on C_D, as it was reduced by 26 %, whereas the major axis has a negligible effect on C_D. The offset angle between the leading and trailing edges affects C_D and C_L. Wang and Liu (2016) investigated the wake dynamics behind HSV, SW, elliptical, and circular cylinders at $Re = 1.8 \times 10^3$. Compared to other cylinders, the HSV cylinder has decreased the recirculation zone in the nodal plane, the presence of highly stable reversed flow, and significant reductions in streamwise and longitudinal velocity fluctuations. Kim and Yoon (2017) inspected the forced heat transfer around HSV, elliptical and circular cylinders at $Re = 0.5 \times 10^3$ and $Pr = 0.7$. The HSV cylinder provided a steady behaviour of heat transfer by inhibiting the instability.

Murphy et al. (2013) investigated the effects of angle of attack (*AoA*) (0°, 45°, and 90°) on FIV of pinniped vibrissae using a laser vibrometer. The analysis shows that *AoA* has the greatest impact on the FIV rather than the surface structure. The authors found that the vortex shedding frequency and velocity rangers were the same for circular and undulated vibrissae. The vortex shedding frequency is highest at 0° and then decreases as the vibrissae are rotated to 90° with respect to the flow direction. Kim and Yoon (2017) investigated the effect of *AoA* (0° *to* 90°) on flow properties around the harbor seal vibrissae (HSV) using LES at $Re = 0.5 \times 10^3$. As *AoA* increases, the vortex shedding frequency of HSV initially increases ($0^o \leq AoA \leq 20^o$) and then decreases ($20^o \leq AoA \leq 90^o$). The authors have compared the flow behind the elliptical and HSV cylinders at different *AoA*, and their instantaneous vortex formations are presented in Fig. 33. Bunjevac et al. (2018) examined the flow properties created by a real elephant seal whisker with an undulating surface and a California seal whisker with a circular surface in the water channel at $Re = 110$ *and* 390. The turbulent intensities are largely suppressed, and the recirculation zone is also reduced past the undulating whisker compared to the circular whisker at $AoA = 0^o$. At $AoA = 90^o$, the power spectral density is higher than that at $AoA = 0^o$. Irrespective of this *AoA*, the power spectral density is 40% lower in the wake of the elephant seal whisker than the California seal whisker.

It was suggested that tubercles on the Humpback whale flipper operate as a lift suppression device (Carreira Pedro and Kobayashi, 2008). Several researchers found that the formation of stream-wise vortices is responsible for the improvement in the hydrodynamic performance (Fish et al., 2011; Fish and Lauder, 2006; Wei et al., 2015). Miklosovic et al. (2004) conducted experiments in the wind tunnel to test the performance of the idealised humpback whale flipper model leading-edge tubercles at $Re = 5 \times 10^5$. The authors have found that the wing with leading-edge tubercles increases C_L by 6% and delays the stall-AoA by 40% compared to the wing without tubercles. Murray et al. (2005) found that the 3D flipper increases C_L by 9% and 4% for 15° and 30° respectively. Hansen et al. (2011) experimentally studied the effect of leading-edge protrusions on NACA airfoils aerodynamic characteristics. The authors have concluded that the tubercles behave similarly to conventional vortex generators. At $Re = 5 \times 10^5$, Pedro and Kobayashi (2008) used DES to simulate the flow filed over a flipper model. The authors have noticed that the tubercles could reduce the flow separation
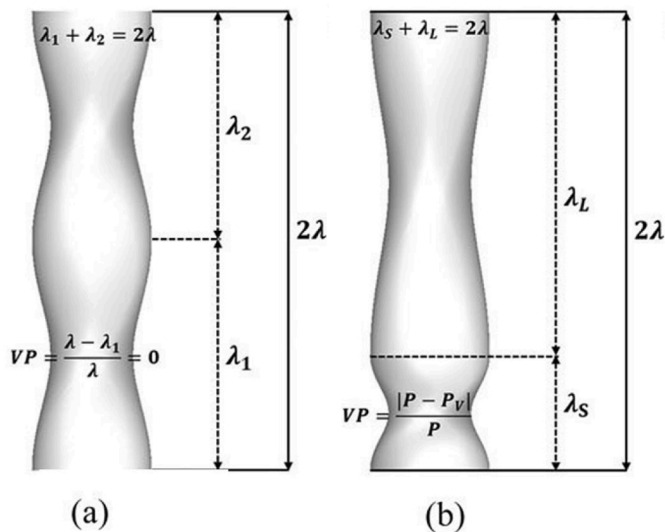

Fig. 30. The geometric shape of (a) HTE and (b) VPHTE, where VP is variable pitch, λ is the wavelength, λ_S *and* λ_L wavelength of short and long pitch parts, respectively. P *and* P_v are the lengths of pitch and pitch varied, respectively (Moon and Yoon, 2020).
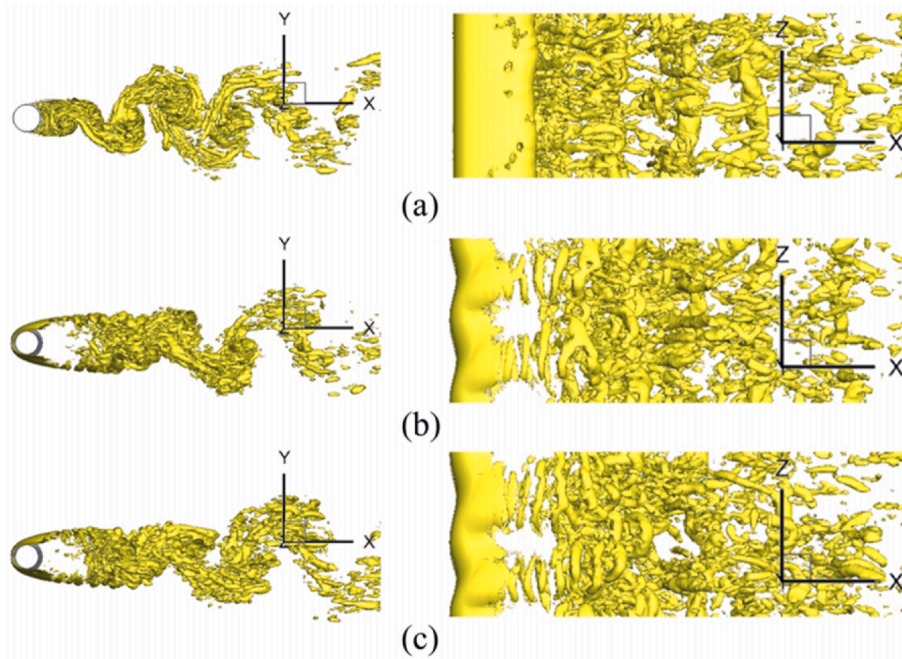
Fig. 31. Left column: side view and right column: top view of the vortex formations behind the (a) circular, (b) HTE, and (c) VPHTE cylinders at $Re = 3.0 \times 10^3$. (Moon and Yoon, 2020).
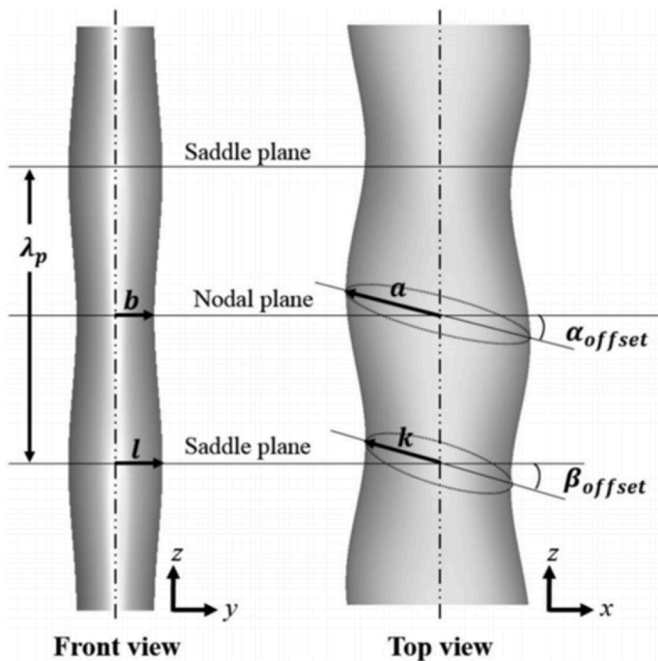

Fig. 32. Schematic of Harbor Seal Vibrissae geometry (Kim and Yoon, 2017).

near the tip of the flipper. At $Re = 1.2 \times 10^5$, Skillen et al. (2015) showed that the spanwise pressure gradient is responsible for the secondary flow behind the trough region. Experimental studies on the swept airfoil wings with tubercle leading edge by Bolzon et al. (2016) and Bolzon et al. (2017) showed that, for AoA between $0°$-$8°$, C_D is reduced by 7–9.5% and C_L is reduced by 4–6%. The wavy leading edge introduces the counter-rotating vortex pairs leading to a downwash effect, resulting in the separation delay. However, the wavy and twisted cylinder produces the transverse vorticity from the 3D separation, suppressing vortex shedding.

5. Comparison of hydrodynamic properties of cylinders with different geometries

In this section, hydrodynamic coefficients of different geometric shapes of cylinders are compared.

The primary wakes around the circular cylinder are found at $Re \geq 47$ and the secondary wake is observed at $Re \geq 110$ which leads to the Karman vortex shedding. The transition of wake from 2D to 3D starts at $Re \geq 180$. As Re increases, C_D is decreased due to an increase in C_{Pb} and upstream suction, leading to a drag crisis. The incidence of drag crisis is categorised into three sub-regimes: (i) gradual reduction on C_D due to the increasing Re (due to an increase in C_{Pb}, and suction), (ii) rapid decrease in C_D due to the increasing Re (primarily due to the increase in C_{Pb}), and (iii) C_D continuous to decrease with an increase in Re (solely due to the rise in the suction).

The wake patterns are strongly affected by rotational rates, and the vortex shedding disappeared at $\alpha \approx 3.5$. The Strouhal frequency is initially stable and then decreased as the rotational rate is increased. As the wake moves downstream of the cylinder, the U-shaped streamwise velocity turns into the V-shaped streamwise velocity. The vortices are shed from either side of the cylinder when G/D is large. As the cylinder approaches the wall, the vortices are shed from the top side of the cylinder leading to a single-side vortex formation. The effect of the gap ratio is negligible when $G/D \geq 1.0$ and the vortex is suppressed for $G/D < 0.3$. The St and width of lock-in decrease as G/D is increased.

The Reynolds number, AR, and AoA have a significant effect on the hydrodynamic coefficients of the elliptical cylinder. C_D is increased as AR and Re increases for $AoA = 30°$ but when the AoA is shifted to a higher value, C_D is decreased even the AR and Re are increased. C_L is decreased as AR is increased and the vortex shedding frequency is increased as Re is increased. The St is increased as G/D is increased and independent of δ/D in the laminar regime. When both the G/D and AR are decreased, and Re is increased, the vortex shedding is completely suppressed near the bottom wall. Flow regimes for flow over an elliptical cylinder in the vicinity of the bottom moving wall for $100 \leq Re \leq 200$, $0.1 \leq G/D \leq 0.4$ and $AR = 0.5$ are presented in Table 6. The elliptical cylinder response at $AR = 0.1$ was twice the response exhibited by the
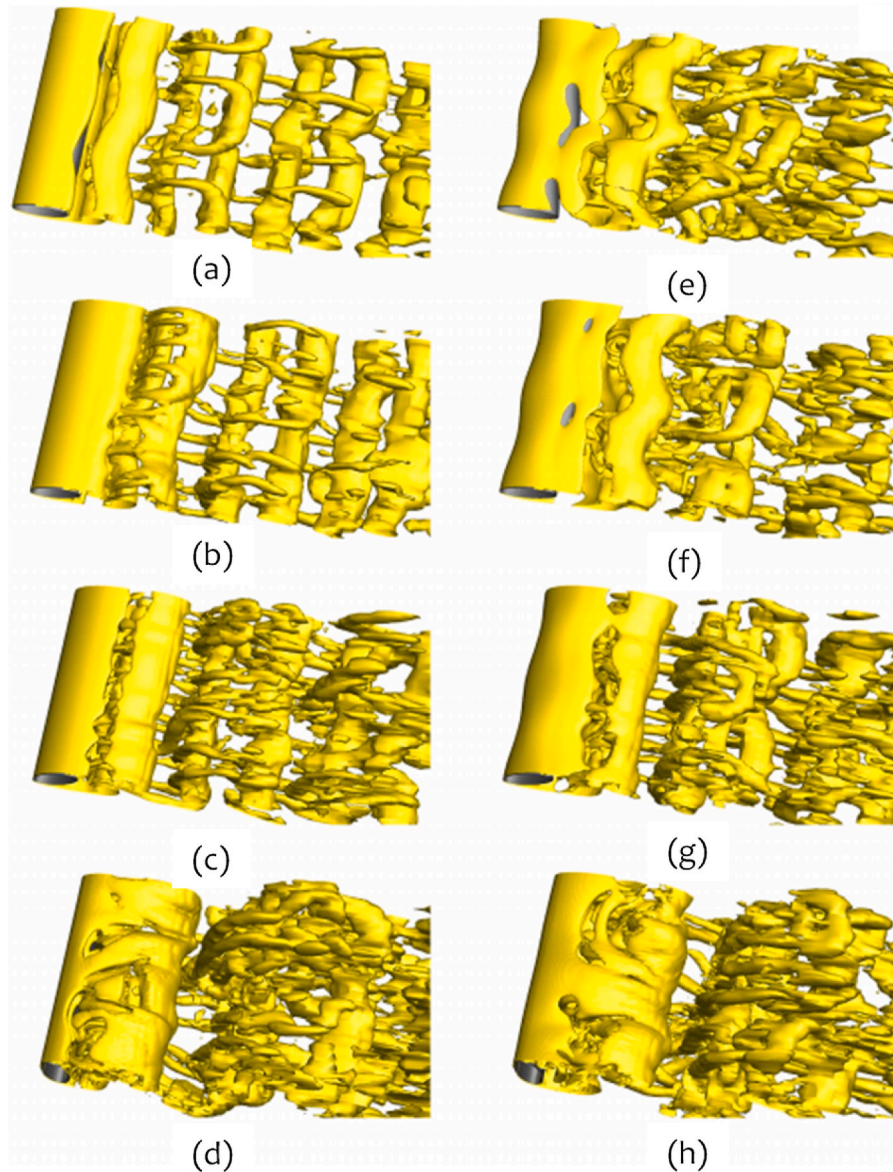
Fig. 33. Formation of vortex shedding behind the elliptical cylinder (left column) and HSV cylinder (right column) for different *AoA* (a) and (e) *AoA* $= 0^o$, (b) and (f) *AoA* $= 15^o$, (c) and (g) *AoA* $= 30^o$, (d) and (h) *AoA* $= 90^o$ (Kim and Yoon, 2017).

circular cylinder and also attained an earlier lock-in. As *AR* is decreased, the lock-in regimes are found to be gradually moved to a smaller V_r.

Apart from conventional geometric shapes of the cylinders, the flow over helically twisted elliptical, symmetric wavy, asymmetric wavy, and harbor seal vibrissae cylinders has also reviewed. The waviness on the SW cylinder modifies the near-wake structure and streamwise vortices, which result in the periodicity formation behind the cylinder. Besides the waviness, the cylinder's wavelength and amplitude play a vital role in regulating the vortices. The SW cylinder reduces the C_D by 18% compared to a circular cylinder at $\lambda/D_m = 1.90$, and C_L is nearly suppressed for Re $= 3.0 \times 10^3$ as shown in Table 7 and 8. The HTE cylinder reduces C_D by 5% and 13% compared to SW and circular cylinders, respectively, and C_L is reduced by 95% compared to the circular cylinder for Re $= 3.0 \times 10^3$. For Re $= 3.0 \times 10^3$, the HTE cylinder reduces C_D by 18% and 23% compared to SW and circular cylinders, respectively, as illustrated in Table 7. It can be concluded that as Re increases, C_D and C_L are effectively reduced for HTE cylinder, which also showed a good performance in heat transfer than a circular cylinder.

VPHTE cylinder has a long vortex formation length than HTE and

circular cylinders. The VPHTE cylinder reduces C_D by 4.1% and 16.7% compared to HTE and circular cylinders, respectively, as shown in Table 7 $C_{L, RMS}$ of the VPHTE cylinder is reduced by 96.2% than the circular cylinder at Re $= 3.0 \times 10^3$ as shown in Table 8. The HSV cylinder reduces the mean C_D by 40% and lifted fluctuations by 90% compared to the circular cylinder, as presented in Tables 7 and 8. Compared to other cylinders, the HSV cylinder has decreased the recirculation zone in the nodal plane and significant reductions in streamwise and longitudinal velocity fluctuations. The DW cylinder significantly reduces C_D and C_L when compared to the circular cylinder and a considerable reduction compared to the SW cylinder as shown in Tables 7 and 8. The turbulent kinetic energy of the DW cylinder near the wake region is smaller than circular and SW cylinders which significantly contributes to the reduction in C_D and C_L. The variation of Strouhal number for various Re for different geometric cylindrical shapes is presented in Table 9.

The general pattern of drag coefficient is summarised as follows for Re $= 3.0 \times 10^3$: $C_{D, CC} > C_{D, SW} > C_{D, ASW} > C_{D, DW} > C_{D, HTE} > C_{D, VPHTE} > C_{D, HSV}$; similarly, the lift coefficient can be summarised as

Table 7

Comparison of drag coefficients for different cylinders from various Reynolds numbers (Yoon et al., 2018 & Moon and Yoon, 2020 adopted more than two Re and drag coefficients in the same paper).

Researchers	Re	Drag Coefficients						
		CC	SW	ASW	DW	HTE	VPHTE	HSV
Lam and Lin (2008)	3.0×10^3	1.09	0.980	–	–	–	–	–
Ahn et al. (2009)	0.3×10^3	1.30	1.280	–	–	–	–	–
Jung and Yoon (2014)	3.0×10^3	0.9934	0.9114	–	–	0.8618	–	–
Kim et al. (2016)	3.9×10^3	1.05	–	–	–	0.856	–	–
Lin et al. (2016)	3.0×10^3	1.08	0.917	–	–	–	–	–
Wei et al. (2016)	0.1×10^3	1.35	–	–	–	1.285	–	–
Yoon et al. (2017)	3.0×10^3	1.0229	0.8926	0.8633	–	–	–	–
Kim and Yoon (2017)	0.5×10^3	1.140	0.801 (EC)	–	–	–	–	0.741
Yoon et al. (2018)	150	1.34	–	–	–	1.200	–	–
	60	1.42	–	–	–	1.420	–	–
Moon et al. (2019)	3.0×10^3	0.9755	0.8831	0.869	–	–	–	–
Yoon et al. (2020)	3.0×10^3	1.0318	0.8972	–	0.8592	–	–	–
Moon and Yoon (2020)	3.0×10^3	0.9936	–	–	–	0.8628	0.8276	–
	0.5×10^3	0.80 (EC)	–	–	–	–	–	0.741

Note: Re- Reynolds number, CC- circular cylinder, EC- elliptical cylinder, SW- symmetric wavy cylinder, ASW- asymmetric wavy cylinder, DW- double wavy cylinder, HTE-helically twisted elliptical cylinder, VPHTE-variable pitch helically twisted elliptical cylinder, and HSV- harbor seal vibrissae cylinder.

Table 8

Comparison of lift coefficients for different cylinders from various Reynolds numbers.
(Yoon et al., 2018 & Moon and Yoon, 2020 adopted more than two Re and lift coefficients in the same paper).

Researchers	Re	Lift Coefficients						
		CC	SW	ASW	DW	HTE	VPHTE	HSV
Lam and Lin (2008)	3.0×10^3	0.177	0.043	–	–	–	–	–
Ahn et al. (2009)	0.3×10^3	0.46	–	–	–	–	–	–
Jung and Yoon (2014)	3.0×10^3	0.115	0.0244	–	–	0.005	–	–
Kim et al. (2016)	3.9×10^3	0.250	–	–	–	0.0052	–	–
Lin et al. (2016)	3.0×10^3	0.456	0.017	–	–	–	–	–
Wei et al. (2016)	0.1×10^3	0.300	–	–	–	0.100	–	–
Yoon et al. (2017)	3.0×10^3	0.1648	0.0148	0.0063	–	–	–	–
Kim and Yoon (2017)	0.5×10^3	0.241	0.0160	–	–	–	–	0.016
Yoon et al. (2018)	150	0.344	–	–	–	0.0832	–	–
	60	0.0686	–	–	–	0.0532	–	–
Moon et al. (2019)	3.0×10^3	0.0836	0.0133	0.0094	–	–	–	–
Yoon et al. (2020)	3.0×10^3	0.1293	0.0152	–	0.0035	–	–	–
Moon and Yoon (2020)	3.0×10^3	0.0922	–	–	–	0.0054	0.0038	–
	0.5×10^3	0.160 (EC)	–	–	–	–	–	0.016

Note: Re- Reynolds number, CC- circular cylinder, EC- elliptical cylinder, SW- symmetric wavy cylinder, ASW- asymmetric wavy cylinder, DW- double wavy cylinder, HTE-helically twisted elliptical cylinder, VPHTE-variable pitch helically twisted elliptical cylinder, and HSV- harbor seal vibrissae.

Table 9

Comparison of Strouhal number for different cylinders from various Reynolds numbers.(Yoon et al., 2018 & Moon and Yoon, 2020 adopted more than two Re and Strouhal numbers in the same paper).

Researchers	Re	Strouhal Number					
		CC	SW	ASW	HTE	VPHTE	HSV
Lam and Lin (2008)	3.0×10^3	0.21	0.21	–	–	–	–
Ahn et al. (2009)	0.3×10^3	–	–	–	–	–	–
Jung and Yoon (2014)	3.0×10^3	0.2112	0.2101	–	0.1904	–	–
Kim et al. (2016)	3.9×10^3	–	–	–	–	–	–
Lin et al. (2016)	3.0×10^3	–	–	–	–	–	–
Wei et al. (2016)	0.1×10^3	0.164	–	–	0.156	–	–
Yoon et al. (2017)	3.0×10^3	0.210	0.180	0.180	–	–	–
Kim and Yoon (2017)	0.5×10^3	0.210	0.297	–	–	–	0.220
Yoon et al. (2018)	150	0.183	–	–	0.174	–	–
	60	0.138	–	–	0.131	–	–
Moon et al. (2019)	3.0×10^3	0.210	0.180	–	–	–	–
Moon and Yoon (2020)	3.0×10^3	0.210	–	–	0.190	0.186	–
	0.5×10^3	0.297 (EC)	–	–	–	–	0.220

Note: Re- Reynolds number, CC- circular cylinder, EC- elliptical cylinder, SW- symmetric wavy cylinder, ASW- asymmetric wavy cylinder, HTE-helically twisted elliptical cylinder, VPHTE-variable pitch helically twisted elliptical cylinder, and HSV- harbor seal vibrissae.
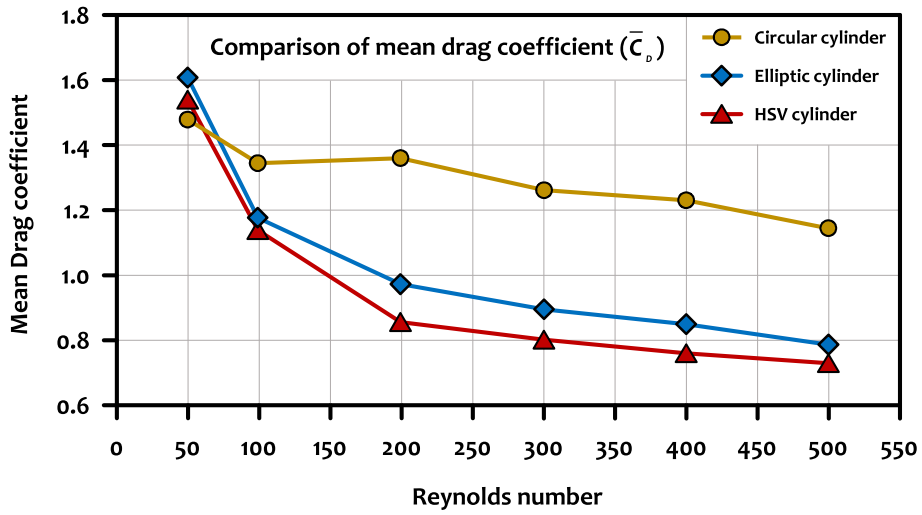
Fig. 34. Comparison of $\overline{C}_D$ between circular, elliptical, and HSV cylinders for $50 \leq Re \leq 500$ (Recreated from Kim and Yoon, 2017).
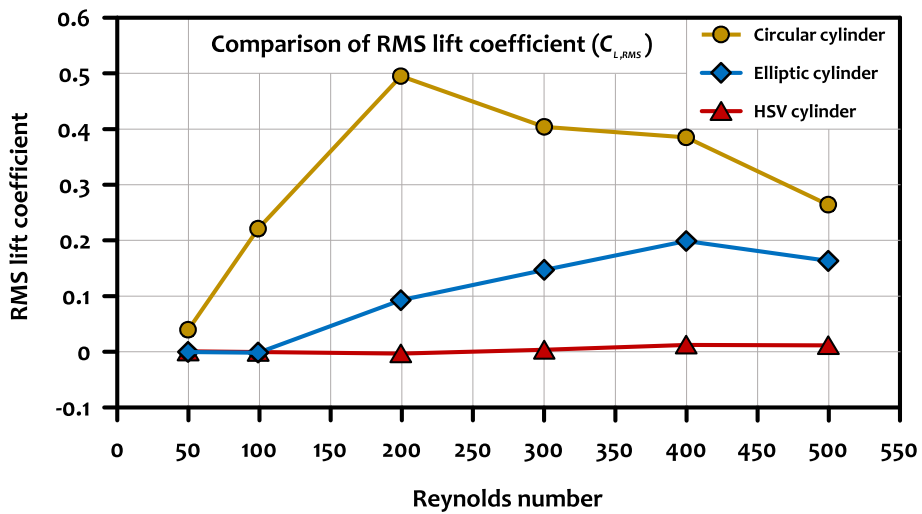

Fig. 35. Comparison of $C_{L,RMS}$ between circular, elliptical, and HSV cylinders for $50 \leq Re \leq 500$ (Recreated from Kim and Yoon, 2017).
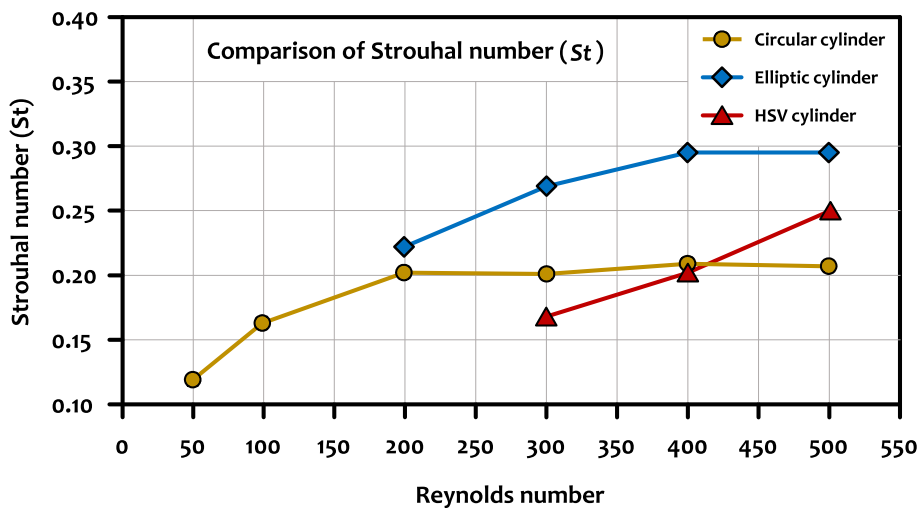

Fig. 36. Comparison of St between circular, elliptical, and HSV cylinders for $50 \leq Re \leq 500$ (Recreated from Kim and Yoon, 2017).

$C_{L,\,CC} > C_{L,\,SW} > C_{L,\,ASW} > C_{L,\,DW} > C_{L,\,HTE} > C_{L,\,VPHTE} > C_{L,\,HSV}$ and the vortex formation length of cylinders can be summarised as: $L_{F,\,CC} < L_{F,\,SW} < L_{F,\,ASW} < L_{F,\,DW} < L_{F,\,HTE} < L_{F,\,VPHTE} < L_{F,\,HSV}$.

From Fig. 34, it can be observed that, at $50 \leq Re \leq 500$, $\overline{C}_D$ of the HSV cylinder is smaller than that of elliptical and circular cylinders. The amount of $\overline{C}_D$ reduction by the HSV cylinder compared to the ellipse is smaller than the circular cylinder. However, in general, all the three cylinders show similar behaviour of $\overline{C}_D$ as Re increases. At Re = 50, $\overline{C}_D$ of HSV and elliptical cylinders are larger than the circular cylinder. HSV and elliptic cylinders have a much bigger decrease for $50 \leq Re \leq 200$. However, $\overline{C}_D$ of the HSV cylinder is always lower than the elliptic cylinder. The reduction of $\overline{C}_D$ by the HSV cylinder ranges between -5% and 36%. $C_{L,\,RMS}$ of the HSV cylinder is increased as Re increases. However, it stays at a lower value than that of circular and elliptical cylinders over the considered Re range, as shown in Fig. 35. For Re ≤ 200, the HSV cylinder reduces $C_{L,\,RMS}$ by 100% and, for Re ≥ 200, $C_{L,\,RMS}$ is reduced by 95% compared to a circular cylinder. This means that the flow over the HSV cylinder is steady for Re up to 200. It is interesting to note that for $50 \leq Re \leq 100$, $C_{L,\,RMS}$ of HSV and elliptical cylinders are almost zero. Hence, it is necessary to identify the critical Re for elliptical and HSV cylinders beyond which the flow becomes unsteady.

The relation between Re and *St* for circular, elliptical, and HSV cylinders is presented in Fig. 36. For the circular cylinder, the *St* gradually increases as Re increases up to 200. Even though Re is increased from 200 to 500, *St* almost remains constant. For the elliptical cylinder, *St* appears from Re = 200 and gradually increases until Re = 400 and then remains constant. For the HSV cylinder, *St* appears when Re = 300. At Re = 300, *St* of the HSV cylinder is smaller than that of elliptical and circular cylinders, but at Re = 500, the *St* is in between the values of elliptical and circular cylinders.

6. Concluding remarks

This paper aims to provide a comprehensive review on recent advances of the wake formations of cylinders such as circular, elliptical, helically twisted elliptical, symmetric wavy, asymmetric wavy, and harbor seal vibrissae cylinders. Comparisons have been made for the hydrodynamic properties and, wake formations for different geometric shapes of the cylinders. A wide range of flow regimes including laminar, sub-critical, critical, and supercritical Reynolds numbers, are considered to investigate the flow characteristics of cylinders.

The effect of spanwise length, rotational rate, gap ratio, boundary layers thickness to diameter ratio, Reynold number are investigated for a circular cylinder. The flow behind the circular cylinder is divided into different regimes based on the parameters and their effects. The drag crisis and formation of separation around the circular cylinder has been examined for a higher Reynolds number and gap ratio. In contrast, the effect of various regimes of Reynolds number, aspect ratio, angle of attack on wake formations, and hydrodynamic coefficients of the elliptical cylinder have been reviewed.

Helically twisted elliptical, symmetric/asymmetric wavy cylinders, and bio-inspired harbor seal vibrissae cylinders have been reviewed in terms of natural flow suppression as well as drag and lift fluctuation reductions. A comparison has been made between the different cylinders at various Reynolds numbers. For example, at Re = 3.0×10^3, the HSV cylinder has reduced the drag force and lift fluctuations to a larger extent when compared to other cylinders. It is expected that bio-inspired cylinders at a high Reynolds number will effectively reduce the hydrodynamic drag and lift forces.

Despite a large amount of research in the literature, the complex nature of the flow over the cylinder will continue to encourage further study. There is limited experimental and numerical work on higher Re for helically twisted elliptical, symmetric wavy, asymmetric wavy, and harbor seal vibrissae cylinders. Some potential areas for future attention can be extended to investigate at high Re along with vortex-, wave and wake-induced vibrations. An extensive study of the Re on these types of cylinders to study the effects of hydrodynamic forces would be beneficial, similar to what has been conducted to circular cylinders. For all cylinders, the effects of subcritical, trans-critical and supercritical Re sensitivity study, surface roughness, freestream turbulence, ground plane, and plane-wall vicinity need more attention because these conditions are often encountered in engineering problems. More investigations are required on bioinspired engineering designs on how these designs can optimize the performance of the structures. We would like to point out that the bioinspired engineering laboratory research need to be transferred into the industrial application to design and operation of bluff bodies. Finally, in order to reduce the computational time and cost, recent advances from the machine learning approach can be adopted to predict the flow characteristics and hydrodynamic responses of the cylinders with different geometries.

Declaration of competing interest

The authors declare that they have no known competing financial interests or personal relationships that could have appeared to influence the work reported in this paper.

Acknowledgements

References

Achenbach, E., 1968. Distribution of local pressure and skin friction around a circular cylinder in cross-flow up to Re= 5×10^6. J. Fluid Mech. 34 (4), 625–639. https://doi.org/10.1017/S002211206800021 20.

Adaramola, M.S., Bergstrom, D.J., Sumner, D., 2012. Characteristics of turbulent flow in the near wake of a stack. Exp. Therm. Fluid Sci. 40, 64–73. https://doi.org/10.1016/j.expthermflusci.2012.02 .001.

Afgan, I., Kahil, Y., Benhamadouche, S., Sagaut, P., 2011. Large eddy simulation of the flow around single and two side-by-s ide cylinders at subcritical Reynolds numbers. Phys. Fluids 23 (7). https://doi.org/10.1063/1.3596267, 075101.

Ahmadi, M.H., Yang, Z., 2020. Large eddy simulation of the flow past a circular cylinder at super-critical Reynolds numbers. Turbo Expo: Power Land Sea Air. https://doi.org/10.1115/GT2020-15393. American Society of Mechanical Engineers, 84089, V02CT35A038.

Ahmed, A., Bays-Muchmore, B., 1992. Transverse flow over a wavy cylinder. Phys. Fluid. Fluid Dynam. 4 (9), 1959–1967. https://doi.org/10.1063/1.858365.

Ahmed, A., Bhattacharya, S., Ahmed, H., Moore, M.H., 2020. On the cylinder wake subjected to in-phase and out-of-phase periodic forcing. Int. J. Heat Fluid Flow 86, 108708. https://doi.org/10.1016/j.ijheatfluidflow.2020.108708.

Ahn, C.T., Yoon, H.S., Ha, M.Y., Lee, H.G., 2009. Waviness effect of a wavy circular cylinder on the heat transfer at a Reynolds number of 300. Int. J. Heat Mass Tran. 52 (1–2), 345–354. https://doi.org/10.1016/j.ijheatmasstransfer.2008.05.032.

Akbar, T., Bouchet, G., Dušek, J., 2011. Numerical investigation of the subcritical effects at the onset of three-dimensionality in the circular cylinder wake. Phys. Fluids 23 (9). https://doi.org/10.1063/1.3626582, 094103.

Akbari, M.H., Price, S.J., 2000. Simulation of the flow over elliptic airfoils oscillating at large angles of attack. J. Fluid Struct. 14 (6), 757–777. https://doi.org/10.1006/jfls.2000.0297.

Alawadhi, E.M., 2015. Numerical simulation of flow past an elliptical cylinder undergoing rotationally oscillating motion. J. Fluid Eng. 137 (3) https://doi.org/10.1115/1.4029323.

Aljure, D.E., Rodríguez, I., Lehmkuhl, O., Pérez-Segarra, C.D., Oliva, A., 2015. Influence of rotation on the flow over a cylinder at Re= 5000. Int. J. Heat Fluid Flow 55, 76–90. https://doi.org/10.1016/j.ijheatfluidflow.2015.07.015.

Asadnia, M., Kottapalli, A.G.P., Haghighi, R., Cloitre, A., y Alvarado, P.V., Miao, J., Triantafyllou, M., 2015. MEMS sensors for assessing flow-related control of an underwater biomimetic robotic stingray. Bioinspiration Biomimetics 10 (3), 036008. https://doi.org/10.1088/1748-3190/10/3/036008.

Badr, H.M., Dennis, S.C.R., Kocabiyik, S., 2001. Numerical simulation of the unsteady flow over an elliptic cylinder at different orientations. Int. J. Numer. Methods Fluid. 37 (8), 905–931. https://doi.org/10.1002/fld.196.

Baek, D.I., Jo, H.J., Lee, M.J., Lim, J.H., Lee, T.K., Kim, J.H., Oh, T.W., 2018. Experimental study on reducing lateral force on circular cylinder using strings. Journal of Ocean Engineering and Technology 32 (4), 237–243. https://doi.org/10.26748/KSOE.2018.6.32.4.237.

Bai, H., Alam, M.M., 2018. Dependence of square cylinder wake on Reynolds number. Phys. Fluids 30 (1). https://doi.org/10.1063/1.4996945, 015102.

Barkley, D., Henderson, R.D., 1996. Three-dimensional Floquet stability analysis of the wake of a circular cylinder. J. Fluid Mech. 322, 215–241. https://doi.org/10.1017/S00221120960 02777.

Barkley, D., Tuckerman, L.S., Golubitsky, M., 2000. Bifurcation theory for three-dimensional flow in the wake of a circular cylinder. Phys. Rev. E 61, 5247–5252. https://doi.org/10.1103/PhysRevE.61.5247.

Bearman, P.W., 1984. Vortex shedding from oscillating bluff bodies. Annu. Rev. Fluid Mech. 16, 195–222. https://doi.org/10.1146/annurev.fl.16.010184.001211.

Bearman, P.W., 2011. Circular cylinder wakes and vortex-induced vibrations. J. Fluid Struct. 27 (5–6), 648–658. https://doi.org/10.1016/j.jfluidstructs.2011.03.021.

Bearman, P.W., Owen, J.C., 1998. Reduction of bluff-body drag and suppression of vortex shedding by the introduction of wavy separation lines. J. Fluid Struct. 12 (1), 123–130. https://doi.org/10.1006/jfls.1997.0128.

Beaudan, P., Moin, P., 1994. Numerical Experiments on the Flow Past a Circular Cylinder at Sub-critical Reynolds Number. Dept. of Mechanical Engineering, Stanford Univ., CA. Thermosciences Div.

Bechert, D.W., Bruse, M., Hage, W., Meyer, R., 2000. Fluid mechanics of biological surfaces and their technological application. Naturwissenschaften 87 (4), 157–171. https://doi.org/10.1007/s00114 005 0696.

Beem, H., Hildner, M., Triantafyllou, M., 2012. Calibration and validation of a harbor seal whisker-inspired flow sensor. Smart Mater. Struct. 22 (1), 014012 https://doi.org/10.1088/0964-1726/22/1/014012.

Behara, S., Borazjani, I., Sotiropoulos, F., 2011. Vortex-induced vibrations of an elastically mounted sphere with three degrees of freedom at Re=300: hysteresis and vortex shedding modes. J. Fluid Mech. 686, 426. https://doi.org/10.1017/jfm.2011.339.

Behara, S., Mittal, S., 2010. Wake transition in flow past a circular cylinder. Phys. Fluids 22 (11), 114104. https://doi.org/10.1063/1.3500692.

Behara, S., Mittal, S., 2011. Transition of the boundary layer on a circular cylinder in the presence of a trip. J. Fluid Struct. 27 (5–6), 702–715. https://doi.org/10.1016/j.jfluidstructs.2011.03.0 17.

Bhattacharya, A., Shahjhan, S.S.S., 2016. Power extraction from vortex-induced angular oscillations of elliptical cylinder. J. Fluid Struct. 63, 140–154. https://doi.org/10.1016/j.jfluidstructs.2016.03.008.

Bhattacharya, S., Gregory, J.W., 2018. Optimum-wavelength forcing of a bluff body wake. Phys. Fluids 30 (1). https://doi.org/10.1063/1.4999091, 015101.

Bhattacharya, S., Gregory, J.W., 2020. The effect of spatially and temporally modulated plasma actuation on cylinder wake. AIAA J. 58 (9), 3808–3818. https://doi.org/10.2514/1.J059269.

Bhushan, B., 2009. Biomimetics: lessons from nature–an overview. Phil. Trans. Math. Phys. Eng. Sci. 367, 1445–1486. https://doi.org/10.1098/rsta.2009.0011, 1893.

Blackburn, H.M., Marques, F., Lopez, J.M., 2005. Symmetry breaking of two-dimensional time-periodic wakes. J. Fluid Mech. 522, 395–411. https://doi.org/10.1017/S0022112004002095.

Blevins, R.D., 1977. Flow-induced Vibration. New York.

Bolzon, M.D., Kelso, R.M., Arjomandi, M., 2016. Formation of vortices on a tubercled wing, and their effects on drag. Aero. Sci. Technol. 56, 46–55. https://doi.org/10.1016/j.ast.2016.06.025.

Bolzon, M.D., Kelso, R.M., Arjomandi, M., 2017. Force measurements and wake surveys of a swept tubercled wing. J. Aero. Eng. 30 (3) https://doi.org/10.1061/(ASCE)AS.1943-5525, 04016085, 0000683.

Borgoltz, A., Intaratep, N., Devenport, W.J., 2020. Experiment 3 - Flow Past a Circular Cylinder. AOE-3054 Course Manual. Department of Aerospace and Ocean Engineering, Virginia Polytechnic Institute and State University.

Bourguet, R., Jacono, D.L., 2014. Flow-induced vibrations of a rotating cylinder. J. Fluid Mech. 740, 342–380. https://doi.org/10.1017/jfm.2013.665.

Breuer, M., 1998. Large eddy simulation of the subcritical flow past a circular cylinder: numerical and modelling aspects. Int. J. Numer. Methods Fluid. 28 (9), 1281–1302. https://doi.org/10.1002/(SICI)1097-0363(19981215)28:9<1281::AID-FLD759>3.0.CO;2-/23.

Breuer, M., 1999. A challenging test case for large eddy simulation: high Reynolds number circular cylinder flow. In: First Symposium on Turbulence and Shear Flow Phenomena. Begel House Inc. https://doi.org/10.1016/S0142-727X(00)00056-4.

Bruun, H.H., Davies, P.O.A.L., 1975. An experimental investigation of the unsteady pressure forces on a circular cylinder in a turbulent crossflow. J. Sound Vib. 40 (4), 535–559. https://doi.org/10.1016/S0022-460X(75)80062-9.

Bunjevac, J., Turk, J., Rinehart, A., Zhang, W., 2018. Wake induced by an undulating elephant seal whisker. J. Visual 21 (4), 597–612. https://doi.org/10.1007/s12650-018-0484-4.

Cadot, O., Desai, A., Mittal, S., Saxena, S., Chandra, B., 2015. Statistics and dynamics of the boundary layer reattachments during the drag crisis transitions of a circular cylinder. Phys. Fluids 27 (1). https://doi.org/10.1063/1.4904756, 014101.

Cantwell, B., Coles, D., 1983. An experimental study of entrainment and transport in the turbulent near wake of a circular cylinder. J. Fluid Mech. 136, 321–374. https://doi.org/10.1017/S0022112 083002189.

Cao, S., Ozono, S., Tamura, Y., Ge, Y., Kikugawa, H., 2010. Numerical simulation of Reynolds number effects on velocity shear flow around a circular cylinder. J. Fluid Struct. 26 (5), 685–702. https://doi.org/10.1016/j.jfluidstructs.2010.03.003.

Carreira Pedro, H., Kobayashi, M., 2008. Numerical study on stall delay on humpback whale flippers. In: In 46th AIAA Aerospace Sciences Meeting and Exhibit, vol. 584. https://doi.org/10.2514/6.2008-584.

Chapelier, J.B., De La Llave Plata, M., Renac, F., Lamballais, E., 2014. Evaluation of a high-order discontinuous Galerkin method for the DNS of turbulent flows. Comput. Fluid 95, 210–226. https://doi.org/10.1016/j.compfluid.2014.02.015.

Chen, L., Dong, Y., Wang, Y., 2021. Flow-induced vibration of a near-wall circular cylinder with a small gap ratio at low Reynolds numbers. J. Fluid Struct. 103, 103247. https://doi.org/10.1016/j.jfluidstructs.2021.103247.

Chen, S.S., Yen, R.H., 2011. Resonant phenomenon of elliptical cylinder flows in a subcritical regime. Phys. Fluids 23 (11), 114105. https://doi.org/10.1063/1.3662003.

Chen, W., Ji, C., Xu, D., Williams, J., 2019. Two-degree-of-freedom vortex-induced vibrations of a circular cylinder in the vicinity of a stationary wall. J. Fluid Struct. 91, 102728. https://doi.org/10.1016/j.jfluidstructs.2019.102728.

Chen, H., Li, Z., Zhang, Y., 2016. U or V shape: dissipation effects on cylinder flow implicit large-eddy simulation. AIAA J. 55 (2), 459–473. https://doi.org/10.2514/1.J055278.

Chen, W., Rheem, C.K., 2019. Experimental investigation of rotating cylinders in flow. J. Mar. Sci. Technol. 24 (1), 111–122. https://doi.org/10.1016/j.ijnaoe.2020.03.004.

Chen, W., Rheem, C.K., Zheng, Y., Incecik, A., Lin, Y., Li, Z., 2020. Discrete-vortex analysis of high Reynolds number flow past a rotating cylinder. AIP Adv. 10 (5) https://doi.org/10.1063/5.0004851, 055104.

Cheng, W., Pullin, D.I., Samtaney, R., 2018. Large-eddy simulation of flow over a rotating cylinder: the lift crisis at $Re_D = 6x10^4$. J. Fluid Mech. 855, 371–407. https://doi.org/10.1017/jfm. 2018.644.

Cheng, W., Pullin, D.I., Samtaney, R., Zhang, W., Gao, W., 2017. Large-eddy simulation of flow over a cylinder with Re_D from $3.9x10^3$ to $8.5x10^5$: a skin-friction perspective. J. Fluid Mech. 820, 121–158. https://doi.org/10.1017/jfm.2017.172.

Chew, Y.T., Cheng, M., Luo, S.C., 1995. A numerical study of flow past a rotating circular cylinder using a hybrid vortex scheme. J. Fluid Mech. 299 https://doi.org/10.1017/S0022112095 003417, 35-35.

Choi, H., Jeon, W.P., Kim, J., 2008. Control of flow over a bluff body. Annu. Rev. Fluid Mech. 40, 113–139. https://doi.org/10.1146/annurev.fluid.39.050905.110149.

Choi, H., Park, H., Sagong, W., Lee, S.I., 2012. Biomimetic flow control based on morphological features of living creatures. Phys. Fluids 24 (12), 121302. https://doi.org/10.1063/1.4772063.

Chopra, G., Mittal, S., 2017. The intermittent nature of the laminar separation bubble on a cylinder in uniform flow. Comput. Fluid 142, 118–127. https://doi.org/10.1016/j.compfluid.2016.06.017.

Chopra, G., Mittal, S., 2019. Drag coefficient and formation length at the onset of vortex shedding. Phys. Fluids 31 (1). https://doi.org/10.1063/1.5075610, 013601.

Chu, S., Xia, C., Wang, H., Fan, Y., Yang, Z., 2021. Three-dimensional spectral proper orthogonal decomposition analyses of the turbulent flow around a seal-vibrissa-shaped cylinder. Phys. Fluids 33 (2). https://doi.org/10.1063/5.0035789, 025106.

Chung, M.H., 2016. Transverse vortex-induced vibration of spring-supported circular cylinder translating near a plane wall. Eur. J. Mech. B Fluid 55, 88–103. https://doi.org/10.1016/j.euromechflu. 2015.09.001.

D'Alessandro, V., Montelpare, S., Ricci, R., 2016. Detached–eddy simulations of the flow over a cylinder at Re= 3900 using OpenFOAM. Comput. Fluid 136, 152–169. https://doi.org/10.1016/j.compfluid. 2016.05.031.

Dehnhardt, G., Kaminski, A., 1995. Sensitivity of the mystacial vibrissae of Harbor seals (Phoca vitulina) for size differences of actively touched objects. J. Exp. Biol. 198 (11), 2317–2323. https://doi.org/10.1242/jeb.198.11.2317.

de la Llave Plata, M., Naddei, F., Couaillier, V., 2018. LES of the flow past a circular cylinder using a multiscale discontinuous Galerkin method. In: The 5th International Conference on Turbulence and Interactions. https://doi.org/10.1007/978-3-030-65820-5_3, 2018.

Derakhshandeh, J.F., Alam, M.M., 2019. A review of bluff body wakes. Ocean Eng. 182, 475–488. https://doi.org/10.1016/j.oceaneng.2019.04.093.

Derakhshandeh, J.F., Gharib, N., 2020. Laminar flow instabilities of a grooved circular cylinder. J. Braz. Soc. Mech. Sci. Eng. 42 (11), 1–16. https://doi.org/10.1007/s40430-020-02657-z.

Desai, A., Mittal, S., Mittal, S., 2020. Experimental investigation of vortex shedding past a circular cylinder in the high subcritical regime. Phys. Fluids 32 (1). https://doi.org/10.1063/1.5124 168, 014105.

Deshpande, R., Kanti, V., Desai, A., Mittal, S., 2017. Intermittency of laminar separation bubble on a sphere during drag crisis. J. Fluid Mech. 812, 815. https://doi.org/10.1017/jfm.2016.827.

Dong, S., Karniadakis, G.E., Ekmekci, A., Rockwell, D., 2006. A combined direct numerical simulation-particle image velocimetry study of the turbulent near wake. J. Fluid Mech. 569, 185. https://doi.org/10.1017/S0022112006002606.

Durante, D., Giannopoulou, O., Colagrossi, A., 2021. Regimes Identification of the Viscous Flow Past an Elliptic Cylinder for Reynolds Number up to 10000. Communications in Nonlinear Science and Numerical Simulation. https://doi.org/10.1016/j.cnsns.2021.105902, 105902.

Fang, P.Z., Du, M.X., Gu, M., 2009. Numerical simulation for vortex-induced vibration of an elliptical cylinder with two degree-of-freedom. J. Vib. Shock 28 (1), 51–56.

Faruquee, Z., Ting, D.S., Fartaj, A., Barron, R.M., Carriveau, R., 2007. The effects of axis ratio on laminar fluid flow around an elliptical cylinder. Int. J. Heat Fluid Flow 28 (5), 1178–1189. https://doi.org/10.1016/j.ijheatfluidflow.2006.11.004.

Fish, F.E., Howle, L.E., Murray, M.M., 2008. Hydrodynamic flow control in marine mammals. Integr. Comp. Biol. 48 (6), 788–800. https://doi.org/10.1093/icb/icn029.

Fish, F.E., Lauder, G.V., 2006. Passive and active flow control by swimming fishes and mammals. Annu. Rev. Fluid Mech. 38, 193–224. https://doi.org/10.1146/annurev.fluid.38.050304.092201.

Fish, F.E., Weber, P.W., Murray, M.M., Howle, L.E., 2011. Marine applications of the biomimetic humpback whale flipper. Mar. Technol. Soc. J. 45 (4), 198–207. https://doi.org/10.4031/MTSJ.45.4.1.

Fonseca, F.B., Mansur, S.S., Vieira, E.D.R., 2013. Flow around elliptical cylinders in moderate Reynolds numbers. Proc. 22nd Int. Cong. Mech. Eng. 3–7.

Franzini, G.R., Fujarra, A.L.C., Meneghini, J.R., Korkischko, I., Franciss, R., 2009. Experimental investigation of vortex-induced vibration on rigid, smooth, and inclined cylinders. J. Fluid Struct. 25 (4), 742–750. https://doi.org/10.1016/j.jfluidstructs.2009.01.003.

Fröhlich, J., Rodi, W., Bertoglio, J.P., Bieder, U., Touil, H., 2001. Large Eddy Simulation of Flow Around Circular Cylinders on Structured and Unstructured Grids, Numerical Flow Simulation II. Springer, Berlin, Heidelberg, pp. 231–249. https://doi.org/10.1007/978-3-540-44567-8_14.

Fröhlich, J., Rodi, W., Kessler, P., Parpais, S., Bertoglio, J.P., Laurence, D., 1998. Large Eddy Simulation of Flow Around Circular Cylinders on Structured and Unstructured Grids. Numerical flow simulation I Springer, Berlin, Heidelberg, pp. 319–338. https://doi.org/10.1007/978-3-540-44437-4_16.

Gallardo, J.P., Andersson, H.I., Pettersen, B., 2016. Three-dimensional instabilities in oscillatory flow past elliptic cylinders. J. Fluid Mech. 798, 371–397. https://doi.org/10.1017/jfm .2016.319.

Garcia, B.F., Weymouth, G.D., Nguyen, V.T., Tutty, O.R., 2019. Span effect on the turbulence nature of flow past a circular cylinder. J. Fluid Mech. 878, 306–323. https://doi.org/10.1017/jfm. 2019.637.

Gerrard, J.H., 1966a. The three-dimensional structure of the wake of a circular cylinder. J. Fluid Mech. 25 (1), 143–164. https://doi.org/10.1017/S0022112066000090.

Gerrard, J.H., 1966. The mechanics of the formation region of vortices behind bluff bodies. J. Fluid Mech. 25 (2), 401–413. https://doi.org/10.1017/S0022112066001721.

Gioria, R.S., Meneghini, J.R., Aranha, J.A.P., Barbeiro, I.C., Carmo, B.S., 2011. Effect of the domain spanwise periodic length on the flow around a circular cylinder. J. Fluid Struct. 27 (5–6), 792–797. https://doi.org/10.1016/j.jfluidstructs.2011.03.007.

Gonçalves, R.T., Franzini, G.R., Rosetti, G.F., Meneghini, J.R., Fujarra, A.L.C., 2015. Flow around circular cylinders with very low aspect ratio. J. Fluid Struct. 54, 122–141. https://doi.org/10.1016/j. jfluidstructs.2014.11.003.

Griffin, O.M., Hall, M.S., 1991. Review-vortex shedding lock-on and flow control in bluff body wakes. J. Fluid Eng. 113 (4), 526–537. https://doi.org/10.1115/1.2926511.

Griffith, M.D., Jacono, D.L., Sheridan, J., Leontini, J.S., 2016. Passive heaving of elliptical cylinders with active pitching–from cylinders towards flapping foils. J. Fluid Struct. 67, 124–141. https://doi.org/10.1016/j.jfluidstructs.2016.09.005.

Grimminger, G., 1945. The Effect of Rigid Guide Vanes on the Vibration and Drag of a Towed Circular Cylinder. DAVID TAYLOR MODEL BASIN WASHINGTON DC.

Gsell, S., Bourguet, R., Braza, M., 2018. Three-dimensional flow past a fixed or freely vibrating cylinder in the early turbulent regime. Phys. Rev. Fluids 3 (1), 013902.

Guo, L., Zhang, X., He, G., 2016. Large-eddy simulation of circular cylinder flow at subcritical Reynolds number: turbulent wake and sound radiation. Acta Mech. Sin. 32 (1), 1–11. https://doi.org/10.1007/s10409-015-0528-0.

Hall, P., 1984. On the stability of the unsteady boundary layer on a cylinder oscillating transversely in a viscous fluid. J. Fluid Mech. 146, 347–367. https://doi.org/10.1017/S00221120840019 07.

Hanke, W., Witte, M., Miersch, L., Brede, M., Oeffner, J., Michael, M., Hanke, F., Leder, A., Dehnhardt, G., 2010. Harbor seal vibrissa morphology suppresses vortex-induced vibrations. J. Exp. Biol. 213 (15), 2665–2672. https://doi.org/10.1242/jeb.043216.

Hans, H., Miao, J., Weymouth, G., Triantafyllou, M., 2013. Whisker-like geometries and their force reduction properties. MTS/IEEE OCEANS-Bergen, IEEE, vols. 1–7. https://doi.org/10.1109/OCEANS-Bergen. 2013.6608113.

Hansen, K.L., Kelso, R.M., Dally, B.B., 2011. Performance variations of leading-edge tubercles for distinct airfoil profiles. AIAA J. 49 (1), 185–194. https://doi.org/10.2514/1.J050631.

Hargreaves, D.M., Kakimpa, B., Owen, J.S., 2014. The computational fluid dynamics modelling of the autorotation of square, flat plates. J. Fluid Struct. 46, 111–133. https://doi.org/10.1016/j. jfluidstructs.2013.12.006.

Hasheminejad, S.M., Jarrahi, M., 2015. Numerical simulation of two-dimensional vortex-induced vibrations of an elliptic cylinder at low Reynolds numbers. Comput. Fluid 107, 25–42. https://doi.org/10.1016/j. compfluid.2014.10.011.

Howarth, L., 1935. Note on the flow past a circular cylinder. In: In Mathematical Proceedings of the Cambridge Philosophical Society, vol. 31. Cambridge University Press, pp. 585–588. https://doi.org/10.1017/S0305004 10001358X, 4.

Huang, W.X., Sung, H.J., 2007. Vortex shedding from a circular cylinder near a moving wall. J. Fluid Struct. 23 (7), 1064–1076. https://doi.org/10.1016/j. jfluidstructs.2007.02.004.

Hughes, T.J., Mazzei, L., Jansen, K.E., 2000. Large eddy simulation and the variational multiscale method. Comput. Visual Sci. 3 (1), 47–59. https://doi.org/10.1007/s0079100 50051.

Ibrahim, T.A., Gomaa, A., 2009. Thermal performance criteria of elliptic tube bundle in crossflow. Int. J. Therm. Sci. 48 (11), 2148–2158. https://doi.org/10.1016/j. ijthermalsci. 2009.03.011.

James, H., Dykes, R.W., 1978. Some experiments on navigation in the Harbor seal, Phoca vitulina. In: Animal Migration, Navigation, and Homing. Springer, Berlin, Heidelberg, pp. 395–404. https://doi.org/10.1007/978-3-662-11147-5_39.

Janocha, M.J., Ong, M.C., Yin, G., 2022. Large eddy simulations and modal decomposition analysis of flow past a cylinder subject to flow-induced vibration. Phys. Fluids 34 (4), 045119. https://doi.org/10.1063/5. 0084966.

Jee, S., Shariff, K., 2014. Detached-eddy simulation based on the v2-f model. Int. J. Heat Fluid Flow 46, 84–101. https://doi.org/10.1016/j.ijheatfluidflow.2013.12.006.

Jeong, H.J., Koo, W., Kim, S.J., 2020. Numerical study on wave run-up of a circular cylinder with various diffraction parameters and body drafts. Journal of Ocean Engineering and Technology 34 (4), 245–252. https://doi.org/10.26748/KSOE.2020.026.

Jiang, H., 2020. Separation angle for flow past a circular cylinder in the subcritical regime. Phys. Fluids 32 (1). https://doi.org/10.1063/1.5139479, 014106.

Jiang, H., Cheng, L., 2017. Strouhal–Reynolds number relationship for flow past a circular cylinder. J. Fluid Mech. 832, 170–188. https://doi.org/10.1017/jfm.2017.685.

Jiang, H., Cheng, L., 2021. Large-eddy simulation of flow past a circular cylinder for Reynolds numbers 400 to 3900. Phys. Fluids 33 (3). https://doi.org/10.1063/5.0041168, 034119.

Jiang, H., Cheng, L., An, H., 2017a. On numerical aspects of simulating flow past a circular cylinder. Int. J. Numer. Methods Fluid. 85 (2), 113–132. https://doi.org/10.1002/fld.4376.

Jiang, H., Cheng, L., Draper, S., An, H., 2017b. Three-dimensional wake transition for a circular cylinder near a moving wall. J. Fluid Mech. 818, 260–287. https://doi.org/10.1017/jfm.2017.146.

Jiang, H., Cheng, L., Draper, S., An, H., Tong, F., 2016. Three-dimensional direct numerical simulation of wake transitions of a circular cylinder. J. Fluid Mech. 801, 353–391. https://doi.org/10.1017/jfm. 2016.446.

Jin, Y., Uth, M.F., Herwig, H., 2015. Structure of a turbulent flow through plane channels with smooth and rough walls: an analysis based on high resolution DNS results. Comput. Fluid 107, 77–88. https://doi.org/10.1016/j.compfluid.2014.10.012.

Johnson, S.A., Thompson, M.C., Hourigan, K., 2001. Flow past elliptical cylinders at low Reynolds numbers. 14th Australasian Fluid Mech. Conf. 343–346.

Johnson, S.A., Thompson, M.C., Hourigan, K., 2004. Predicted low frequency structures in the wake of elliptical cylinders. Eur. J. Mech. B Fluid 23 (1), 229–239. https://doi.org/10.1016/j.euromechflu. 2003.05.006.

Jung, J.H., Oh, S., Nam, B.W., Park, B., Kwon, Y.J., Jung, D., 2019. Numerical study on flow characteristics around curved riser. J. Ocean Eng. Technol. 33 (2), 123–130. https://doi.org/10.26748/KSOE.2018.079.

Jung, J.H., Yoon, H.S., 2014. Large eddy simulation of flow over a twisted cylinder at a subcritical Reynolds number. J. Fluid Mech. 759, 579–611. https://doi.org/10.1017/jfm.2014.581.

Kacker, S.C., Pennington, B., Hill, R.S., 1974. Fluctuating lift coefficient for a circular cylinder in cross flows. J. Mech. Eng. Sci. 16 (4), 215–224. https://doi.org/10.1243/2FJMES_JOUR_1974_016_040_02.

Karabelas, S.J., 2010. Large eddy simulation of high-Reynolds number flow past a rotating cylinder. Int. J. Heat Fluid Flow 31 (4), 518–527. https://doi.org/10.1016/j.ijheat fluidflow.2010.02.010.

Karlson, M., Nita, B.G., Vaidya, A., 2020. Numerical computations of vortex formation length in flow past an elliptical cylinder. Fluid 5 (3), 157. https://doi.org/10.3390/fluids5030157.

Karman, T., 1911. v.: Über den Mechanismus des Widerstandes, den ein bewegter Körper in einer Flüssigkeit erfährt. Nachr. kgl. Ges. Wiss. Göttingen, mat.-phys. Kl 509. http://eudml.org/doc/58812.

Keser, H., Unal, M.F., Bearman, P.W., 2001. Simulation of wake from circular cylinder with spanwise sinusoidal waviness. The Proc. Second Intl Conf. Vortex Methods. 131–137.

Khan, N.B., Ibrahim, Z., Bin Mohamad Badry, A.B., Jameel, M., Javed, M.F., 2019. Numerical investigation of flow around cylinder at Reynolds number= 3900 with large eddy simulation technique: effect of spanwise length and mesh resolution. The Institution of Mechanical Engineers. M J. Eng. Maritime Environ. 233 (2), 417–427. https://doi.org/10.1177/1475090217751326.

Khan, N.B., Ibrahim, Z., Nguyen, L.T.T., Javed, M.F., Jameel, M., 2017. Numerical investigation of the vortex-induced vibration of an elastically mounted circular cylinder at high Reynolds number (Re= 10^4) and low mass ratio using the RANS code. PLoS One 12 (10), e0185832. https://doi.org/10.1371/journal. pone.0185832.

Khan, W., Culham, J.R., Yovanovich, M., 2004. Fluid flow and heat transfer from elliptical cylinder: analytical approach. 37th AIAA Thermophysics Conference, Portland, Oregon, 2272. https://doi.org/10.2514/6.2004-2272..

Kim, D.K., Wong, E.W.C., Lekkala, M.K.R., 2019. A parametric study on fatigue of a top-tensioned riser subjected to vortex-induced vibrations. Struct. Monit. Maint. 6 (4), 365–387. https://doi.org/10.12989/smm.2019.6.4.365.

Kim, H., Yoon, H.S., 2017. Effect of the orientation of the harbor seal vibrissa based biomimetic cylinder on hydrodynamic forces and vortex-induced frequency. AIP Adv. 7 (10), 105015. https://doi.org/10.1063/5.0013735.

Kim, J., Choi, H., 2005. Distributed forcing of flow over a circular cylinder. Phys. Fluids 17 (3), 033103. https://doi.org/10.1063/1.1850151.

Kim, M.S., Park, Y.B., 2006. Unsteady lift and drag forces acting on the elliptic cylinder. J. Mech. Sci. Technol. 20 (1), 167–175. https://doi.org/10.1007/BF02916210.

Kim, M.S., Sengupta, A., 2005. Unsteady viscous flow over elliptic cylinders at various thickness with different Reynolds numbers. J. Mech. Sci. Technol. 19 (3), 877–886. https://doi.org/10.1007/BF02916136.

Kim, W., Lee, J., Choi, H., 2016. Flow around a helically twisted elliptic cylinder. Phys. Fluids 28 (5), 053602. https://doi.org/10.1063/1.4948247.

Kocabiyik, S., D'Alessio, S.J.D., 2004. Numerical study of flow around an inclined elliptic cylinder oscillating in line with an incident uniform flow. Eur. J. Mech. B Fluid 23 (2), 279–302. https://doi.org/10.1016/j.euromechflu.2003.09.001.

Kondo, N., 2012. Three-dimensional computation for flow-induced vibrations in in-line and cross-flow directions of a circular cylinder. Int. J. Numer. Methods Fluid. 70 (2), 158–185. https://doi.org/10.1002/fld.2682.

Koumoutsakos, P., Leonard, A., 1995. High-resolution simulations of the flow around an impulsively started cylinder using vortex methods. J. Fluid Mech. 296, 1–38. https://doi.org/10.1017/S0022112095002059.

Kravchenko, A.G., Moin, P., 2000. Numerical studies of flow over a circular cylinder at Re$_D$= 3900. Phys. Fluids 12 (2), 403–417. https://doi.org/10.1063/1.870318.

Kumar, D., Mittal, M., Sen, S., 2018. Modification of response and suppression of vortex-shedding in vortex-induced vibrations of an elliptic cylinder. Int. J. Heat Fluid Flow 71, 406–419. https://doi.org/10.1016/j.ijheatfluidflow.2018.05.006.

Kumar, P., Tiwari, S., 2021. Effect of axis ratio on unsteady wake of surface mounted elliptic cylinder immersed in shear flow. Fluid Dynam. Res. 53 (4), 045502 https://doi.org/10.1088/1873-7005/ac105e.

Kumar, S., Navrose Mittal, S., 2016. Lock-in in forced vibration of a circular cylinder. Phys. Fluids 28 (11), 113605. https://doi.org/10.1063/1.4967729.

Kushwaha, V., Bao, Y., Zhou, D., Nepali, R., 2020. The effect of axis ratio on the vortex-induced vibration of an elliptical cylinder. IOP Conf. Ser. Earth Environ. Sci. 446 (5), 052042 https://doi.org/10.1088/1755-1315/446/5/052042. IOP Publishing.

Lam, K., Lin, Y.F., 2008a. Large eddy simulation of flow around wavy cylinders at a subcritical Reynolds number. Int. J. Heat Fluid Flow 29 (4), 1071–1088. https://doi.org/10.1016/j.ijheatfluidflow.2009.01.005.

Lam, K., Lin, Y.F., 2008b. Numerical Simulation on the Control of Drag Force and Vortex Formation by Different Wavy (Varicose) Cylinders. The IUTAM Symposium on Flow Control and MEMS. Springer, Dordrecht, pp. 415–419. https://doi.org/10.1007/978-1-4020-6858-4_52.

Lam, K., Lin, Y.F., 2009. Effects of wavelength and amplitude of a wavy cylinder in cross-flow at low Reynolds numbers. J. Fluid Mech. 620, 195–220. https://doi.org/10.1017/S002211200800 4217.

Lam, K.M., 2009. Vortex shedding flow behind a slowly rotating circular cylinder. J. Fluid Struct. 25 (2), 245–262. https://doi.org/10.1016/j.jfluidstructs.2008.04.005.

Lam, K., Wang, F.H., Li, J.Y., So, R.M.C., 2004a. Experimental investigation of the mean and fluctuating forces of wavy (varicose) cylinders in a crossflow. J. Fluid Struct. 19 (3), 321–334. https://doi.org/10.1016/j.jfluidstructs.2003.12.010.

Lam, K., Wang, F.H., So, R.M.C., 2004b. Three-dimensional nature of vortices in the near wake of a wavy cylinder. J. Fluid Struct. 19 (6), 815–833. https://doi.org/10.1016/j.jfluidstructs.2004.04.004.

Law, Y.Z., Jaiman, R.K., 2017. Wake stabilization mechanism of low-drag suppression devices for vortex-induced vibration. J. Fluid Struct. 70, 428–449. https://doi.org/10.1016/j.jfluidstructs.2017.02.005.

Lee, S.J., 2004. POD analysis of near-wake structures of an elliptic cylinder adjacent to a free surface. J. Visual 7 (3), 179–186. https://doi.org/10.1007/BF03181632.

Lee, S.J., Nguyen, A.T., 2007. Experimental investigation on wake behind a wavy cylinder having sinusoidal cross-sectional area variation. Fluid Dynam. Res. 39 (4), 292. https://doi.org/10.1016/j.fluiddyn.2006.06.003.

Lei, C., Cheng, L., Kavanagh, K., 1999. Re-examination of the effect of a plane boundary on force and vortex shedding of a circular cylinder. J. Wind Eng. Ind. Aerod. 80 (3), 263–286. https://doi.org/10.1016/S0167-6105(98)00204-9.

Lei, C., Cheng, L., Kavanagh, K., 2001. Spanwise length effects on three-dimensional modelling of flow over a circular cylinder. Comput. Methods Appl. Mech. Eng. 190 (22–23), 2909–2923. https://doi.org/10.1016/S0045-7825(00)00272-3.

Lehmkuhl, O., Rodríguez, I., Borrell, R., Chiva, J., Oliva, A., 2014. Unsteady forces on a circular cylinder at critical Reynolds numbers. Phys. Fluids 26 (12), 125110. https://doi.org/10.1063/1.4904015.

Lehmkuhl, O., Rodríguez, I., Borrell, R., Oliva, A., 2013. Low-frequency unsteadiness in the vortex formation region of a circular cylinder. Phys. Fluids 25 (8). https://doi.org/10.1063/1.4818641, 085109.

Lekkala, M.R., Latheef, M., Kim, D.K., Wahab, M.B.A., 2021. Numerical assessment of flow around circular cylinder. In: In Proceedings of the International Conference on Civil, Offshore and Environmental Engineering, pp. 289–301. https://doi.org/10.1007/978-981-33-6311-3_34.

Lekkala, M.R., Mohamed, L., Hafiz, M.F.U., Kim, D.K., 2020. A practical technique for hydrodynamic coefficients modification in SHEAR7 for fatigue assessment of riser buoyancy modules under vortex-induced vibration. Ocean Eng. 217, 107760. https://doi.org/10.1016/j.oceaneng.2020.107760.

Leontini, J.S., Griffith, M.D., Jacono, D.L., Sheridan, J., 2018. The flow-induced vibration of an elliptical cross-section at varying angles of attack. J. Fluid Struct. 78, 356–373. https://doi.org/10.1016/j.jfluidstructs.2017.12.013.

Leontini, J.S., Jacono, D.L., Thompson, M.C., 2015. Stability analysis of the elliptic cylinder wake. J. Fluid Mech. 763, 302–321. https://doi.org/10.1017/jfm.2014.671.

Li, S., Zhou, T., Sun, Z., Dong, Z., 2016. External forced convection from circular cylinders with surface protrusions. Int. J. Heat Mass Tran. 99, 20–30. https://doi.org/10.1016/j.ijheatmasstransfer.2016.03.092.

Li, Z., Jaiman, R.K., Khoo, B.C., 2017. Coupled dynamics of vortex-induced vibration and stationary wall at low Reynolds number. Phys. Fluids 29 (9). https://doi.org/10.1063/1.4986410, 093601.

Lim, H.C., Lee, S.J., 2002. Flow control of circular cylinders with longitudinal grooved surfaces. AIAA J. 40 (10), 2027–2036. https://doi.org/10.2514/2.1535.

Lim, J.H., Jo, H.J., Hwang, J.H., Kim, J.H., Lee, T.K., Choi, Y.W., Lee, M.J., Kim, Y.K., 2019. Experimental study on reducing motion of circular cylinder in currents. Journal of Ocean Engineering and Technology 33 (4), 350–357. https://doi.org/10.26748/KSOE.2019.028.

Lin, W.J., Lin, C., Hsieh, S.C., Dey, S., 2009. Flow characteristics around a circular cylinder placed horizontally above a plane boundary. J. Eng. Mech. 135 (7), 697–716. https://doi.org/10.1061/(ASCE)0733-9399(2009)135:7(697).

Lin, Y.F., Bai, H.L., Alam, M.M., Zhang, W.G., Lam, K., 2016. Effects of large spanwise wavelength on the wake of a sinusoidal wavy cylinder. J. Fluid Struct. 61, 392–409. https://doi.org/10.1016/j.jfluidstructs.2015.12.004.

Liu, G., Xue, Q., Zheng, X., 2019. Phase-difference on seal whisker surface induces hairpin vortices in the wake to suppress force oscillation. Bioinspiration Biomimetics 14 (6). https://doi.org/10.1088/1748-3190/ab34fe, 066001.

Lloyd, T.P., James, M., 2016. Large eddy simulations of a circular cylinder at Reynolds numbers surrounding the drag crisis. Appl. Ocean Res. 59, 676–686. https://doi.org/10.1016/j.apor.2 015.11.009.

Lourenco, L.M., Shih, C., 1993. Characteristics of the Plane Turbulent Near Wake of a Circular Cylinder. A Particle Image Velocimetry Study.

Lu, H., Lua, K.B., Lim, T.T., 2018. Flow past a rapidly rotating elliptic cylinder. Eur. J. Mech. B Fluid 72, 676–690. https://doi.org/10.1016/j.euromechflu.2018.08.011.

Lua, K.B., Lim, T.T., Yeo, K.S., 2010. A rotating elliptic airfoil in fluid at rest and in a parallel freestream. Exp. Fluid 49 (5), 1065–1084. https://doi.org/10.1007/s00348-010-0847-7.

Lua, K.B., Lu, H., Lim, T.T., 2018. Rotating elliptic cylinders in a uniform cross flow. J. Fluid Struct. 78, 36–51. https://doi.org/10.1016/j.jfluidstructs.2017.12.023.

Luo, D., Yan, C., Liu, H., Zhao, R., 2014. Comparative assessment of PANS and DES for simulation of flow past a circular cylinder. J. Wind Eng. Ind. Aerod. 134, 65–77. https://doi.org/10.1016/j.jweia.2014.08.014.

Lysenko, D.A., Donskov, M., Ertesvåg, I.S., 2021. Large-eddy simulations of the flow over a semi-circular cylinder at Re= 50000. Comput. Fluid 228, 105054. https://doi.org/10.1016/j.compfluid.2021.105054.

Lysenko, D.A., Ertesvåg, I.S., 2021. Assessment of algebraic subgrid scale models for the flow over a triangular cylinder at Re= 45000. Ocean Eng. 222, 108559. https://doi.org/10.1016/j.oceaneng.2020.108559.

Lysenko, D.A., Ertesvåg, I.S., Rian, K.E., 2012. Large-eddy simulation of the flow over a circular cylinder at Reynolds number 3900 using the OpenFOAM toolbox. Flow, Turbul. Combust. 89 (4), 491–518. https://doi.org/10.1007/s10494-012-9405-0.

Lysenko, D.A., Ertesvåg, I.S., Rian, K.E., 2014. Large-eddy simulation of the flow over a circular cylinder at Reynolds number 2×10^4. Flow, Turbul. Combust. 92 (3), 673–698. https://doi.org/10.1007/s10494-013-9509-1.

Ma, L., Lin, K., Fan, D., Wang, J., Triantafyllou, M.S., 2022. Flexible cylinder flow-induced vibration. Phys. Fluids 34 (1). https://doi.org/10.1063/5.0078418, 011302.

Ma, X., Karamanos, G.S., Karniadakis, G.E., 2000. Dynamics and low-dimensionality of a turbulent near wake. J. Fluid Mech. 410, 29–65. https://doi.org/10.1017/S0022112099007934.

Mahesh, K., Constantinescu, G., Moin, P., 2004. A numerical method for large-eddy simulation in complex geometries. J. Comput. Phys. 197 (1), 215–240. https://doi.org/10.1016/j.jcp.2003.11.031.

Mani, A., Moin, P., Wang, M., 2009. Computational study of optical distortions by separated shear layers and turbulent wakes. J. Fluid Mech. 625, 273. https://doi.org/10.1017/S0022112008005697.

Matz, D., Baars, A., 2012. Vortex Structures behind a Harbor Seal Vibrissa—A Numerical Study. The XIII Bilateral Czech/German Symposium. University Centre Telč, Telč, Czech Republic, pp. 103–106.

Meyer, M., Hickel, S., Adams, N.A., 2010. Assessment of implicit large-eddy simulation with a conservative immersed interface method for turbulent cylinder flow. Int. J. Heat Fluid Flow 31 (3), 368–377. https://doi.org/10.1016/j.ijheatfluidflow.2010.02.026.

Miersch, L., Hanke, W., Wieskotten, S., Hanke, F.D., Oeffner, J., Leder, A., Brede, M., Witte, M., Dehnhardt, G., 2011. Flow sensing by pinniped whiskers. Phil. Trans. Biol. Sci. 366 (1581), 3077–3084. https://doi.org/10.1098/rstb.2011.0155.

Miklosovic, D.S., Murray, M.M., Howle, L.E., Fish, F.E., 2004. Leading-edge tubercles delay stall on humpback whale (Megaptera novaeangliae) flippers. Phys. Fluids 16 (5), L39–L42. https://doi.org/10.1063/1.1688341.

Miller, G.D., Williamson, C.H.K., 1994. Control of three-dimensional phase dynamics in a cylinder wake. Exp. Fluid 18, 26–35. https://doi.org/10.1007/BF00209358.

Mittal, R., Balachandar, S., 1996. Direct numerical simulation of flow past elliptic cylinders. J. Comput. Phys. 124 (2), 351–367. https://doi.org/10.1006/jcph.1996.0065.

Mittal, R., Balachandar, S., 1997. On the inclusion of three-dimensional effects in simulations of two-dimensional bluff-body wake flows. Asme Fluids Eng. Div. Summer Meeting 1–6.

Mittal, S., 2013. Free vibrations of a cylinder: 3-D computations at Re=1000. J. Fluid Struct. 41, 109–118. https://doi.org/10.1016/j.jfluidstructs.2013.02.017.

Molochnikov, V.M., Mikheev, N.I., Mikheev, A.N., Paereliy, A.A., Dushin, N.S., Dushina, O.A., 2019. SIV measurements of flow structure in the near wake of a circular cylinder at Re= 3900. Fluid Dynam. Res. 51 (5) https://doi.org/10.1088/1873-7005/ab2c27, 055505.

Moon, J., Yoon, H.S., 2020. Effect of variable pitch on flow around a helically twisted elliptic cylinder. AIP Adv. 10 (9), 095215 https://doi.org/10.1063/5.0013735.

Moon, J., Yoon, H.S., Kim, H.J., Kim, M.I., 2019. Forced convection heat transfer from an asymmetric wavy cylinder at a subcritical Reynolds number. Int. J. Heat Mass Tran. 129, 707–720. https://doi.org/10.1016/j.ijheatmasstransfer.2018.10.029.

Moussaed, C., Salvetti, M.V., Wornom, S., Koobus, B., Dervieux, A., 2014. Simulation of the flow past a circular cylinder in the supercritical regime by blending RANS and variational-multiscale LES models. J. Fluid Struct. 47, 114–123. https://doi.org/10.1016/j.jfluidstructs.2013.11.006.

Munir, A., Zhao, M., Wu, H., Lu, L., Ning, D., 2018. Three-dimensional numerical investigation of vortex-induced vibration of a rotating circular cylinder in uniform flow. Phys. Fluids 30 (5), 053602. https://doi.org/10.1063/1.5025238.

Murphy, C.T., Eberhardt, W.C., Calhoun, B.H., Mann, K.A., Mann, D.A., 2013. Effect of angle on flow-induced vibrations of pinniped vibrissae. PLoS One 8 (7), e69872. https://doi.org/10.1371/journal. pone. 0069872.

Murray, M.M., Miklosovic, D.S., Fish, F.E., Howle, L.E., 2005. Effects of leading-edge tubercles on a representative whale flipper model at various sweep angles. In: In Durham, NH: Conference Proceedings of the 14th International Symposium on Unmanned Untethered Submersible Technology.

Naik, S.N., Vengadesan, S., Prakash, K.A., 2017. Numerical study of fluid flow past a rotating elliptic cylinder. J. Fluid Struct. 68, 15–31. https://doi.org/10.1016/j. jfluidstructs. 2016.09.011.

Naik, S.N., Vengadesan, S., Prakash, K.A., 2018. Linear shear flow past a rotating elliptic cylinder. J. Fluid Eng. 140 (12) https://doi.org/10.1115/1.4040365.

Nair, M.T., Sengupta, T.K., 1996. Onset of asymmetry: flow past circular and elliptic cylinders. Int. J. Numer. Methods Fluid. 23 (12), 1327–1345. https://doi.org/10.1002/(SICI)1097-0363(19961230)23:12<1327::AID-FLD476>3.0.CO;2-Q.

Nam, S.H., Yoon, H.S., 2022. Effect of the wavy geometric disturbance on the flow over elliptic cylinders with different aspect ratios. Ocean Eng. 243, 110287. https://doi.org/10.1016/j.oceaneng.2021.110287.

Naudascher, E., Rockwell, D., 2012. Flow-induced Vibrations: an Engineering Guide. Courier Corporation.

Nebres, J., Batill, S., 1992. Flow about cylinders with helical surface protrusions. 30th Aerospace Sci. Meeting Exhibit 540. https://doi.org/10.2514/6.1992-540.

Nguyen, A.T., Jee, S., 2004. Experimental investigation on wake behind a sinusoidal cylinder. In: The Proceedings of the Proceeding of Tenth Asian Congress of Fluid Mechanics.

Nguyen, V.T., Nguyen, H.H., 2016. Detached eddy simulations of flow-induced vibrations of circular cylinders at high Reynolds numbers. J. Fluid Struct. 63, 103–119. https://doi.org/10.1016/j. jfluidstructs.2016.02.004.

Norberg, C., 1987. Effects of Reynolds number and a low-intensity freestream turbulence on the flow around a circular cylinder. Chalmers University, 87. Technological Publications, Goteborg, Sweden, pp. 1–55, 2.

Norberg, C., 1994. An experimental investigation of the flow around a circular cylinder: influence of aspect ratio. J. Fluid Mech. 258, 287–316. https://doi.org/10.1017/S0022112094003332.

Norberg, C., 2001. Flow around a circular cylinder: aspects of fluctuating lift. J. Fluid Struct. 15 (3–4), 459–469. https://doi.org/10.1006/jfls.2000.0367.

Norberg, C., 2003. Fluctuating lift on a circular cylinder: review and new measurements. J. Fluid Struct. 17 (1), 57–96. https://doi.org/10.1016/S0889-9746(02)00099-3.

Ong, L., Wallace, J., 1996. The velocity field of the turbulent very near wake of a circular cylinder. Exp. Fluid 20 (6), 441–453. https://doi.org/10.1007/BF00189383.

Ong, M.C., Utnes, T., Holmedal, L.E., Myrhaug, D., Pettersen, B., 2009. Numerical simulation of flow around a smooth circular cylinder at very high Reynolds numbers. Mar. Struct. 22 (2), 142–153. https://doi.org/10.1016/j.marstruc.2008.09.001.

Ong, M.C., Utnes, T., Holmedal, L.E., Myrhaug, D., Pettersen, B., 2010. Numerical simulation of flow around a circular cylinder close to a flat seabed at high Reynolds numbers using a k–ε model. Coast. Eng. 57 (10), 931–947. https://doi.org/10.1016/j.coastaleng.2010.05.008.

Oruc, V., 2017. Strategies for the applications of flow control downstream of a bluff body. Flow Meas. Instrum. 53, 204–214. https://doi.org/10.1016/j.flowmeasinst.2016.08.008.

Ouvrard, H., Koobus, B., Dervieux, A., Salvetti, M.V., 2010. Classical and variational multiscale LES of the flow around a circular cylinder on unstructured grids. Comput. Fluid 39 (7), 1083–1094. https://doi.org/10.1016/j.compfluid.2010.01.017.

Owen, J.C., Bearman, P.W., Szewczyk, A.A., 2001. Passive control of VIV with drag reduction. J. Fluid Struct. 15 (3–4), 597–605. https://doi.org/10.1006/jfls.2000.0358.

Owen, J.C., Szewczyk, A.A., Bearman, P.W., 2000. Suppression of Karman vortex shedding. Phys. Fluids 12 (9). https://doi.org/10.1063/1.4739170. S9-S9.

Parnaudeau, P., Carlier, J., Heitz, D., Lamballais, E., 2008. Experimental and numerical studies of the flow over a circular cylinder at Reynolds number 3900. Phys. Fluids 20 (8), 085101. https://doi.org/10.1063/1. 2957018.

Paul, I., Prakash, K.A., Vengadesan, S., 2014. Onset of laminar separation and vortex shedding in flow past unconfined elliptic cylinders. Phys. Fluids 26 (2), 023601. https://doi.org/10.1063/1.4866454.

Paul, I., Prakash, K.A., Vengadesan, S., Pulletikurthi, V., 2016. Analysis and characterization of momentum and thermal wakes of elliptic cylinders. J. Fluid Mech. 807, 303–323. https://doi.org/10.1017/jfm.2016.625.

Perrin, R., Mockett, C., Braza, M., Cid, E., Cazin, S., Sevrain, A., Chassaing, P., Thiele, F., 2007. Joint numerical and experimental investigation of the flow around a circular cylinder at high Reynolds number. Particle Image Velocim. 223–244. https://doi.org/10.1007/978-3-540-73528-1_11.

Perumal, D.A., Kumar, G.V., Dass, A.K., 2012. Lattice Boltzmann simulation of viscous flow past elliptical cylinder. CFD Lett. 4 (3), 127–139.

Posdziech, O., Grundmann, R., 2001. Numerical simulation of the flow around an infinitely long circular cylinder in the transition regime. Theor. Comput. Fluid Dynam. 15, 121–141. https://doi.org/10.1007/s001 6201 00046.

Prasanth, T.K., Mittal, S., 2008. Vortex-induced vibrations of a circular cylinder at low Reynolds numbers. J. Fluid Mech. 594, 463–491. https://doi.org/10.1017/S0022112007009202.

Prsic, M.A., Ong, M.C., Pettersen, B., Myrhaug, D., 2014. Large Eddy Simulations of flow around a smooth circular cylinder in a uniform current in the subcritical flow regime. Ocean Eng. 77, 61–73. https://doi.org/10.1016/j.oceaneng.2013.10.018.

Qiu, W., Lee, D.Y., Lie, H., Rousset, J.M., Mikami, T., Sphaier, S., Tao, L., Wang, X., Magarovskii, V., 2017. Numerical benchmark studies on drag and lift coefficients of a marine riser at high Reynolds numbers. Appl. Ocean Res. 69, 245–251. https://doi.org/10.1016/j.apor.2017.10.010.

Qu, L., Norberg, C., Davidson, L., Peng, S.H., Wang, F., 2013. Quantitative numerical analysis of flow past a circular cylinder at Reynolds number between 50 and 200. J. Fluid Struct. 39, 347–370. https://doi.org/10.1016/j.jfluidstructs.2013.02.007.

Radi, A., Thompson, M.C., Sheridan, J., Hourigan, K., 2013. From the circular cylinder to the flat plate wake: the variation of Strouhal number with Reynolds number for elliptical cylinders. Phys. Fluids 25 (10), 101706. https://doi.org/10.1063/1.4827521.

Rajagopalan, S., Antonia, R.A., 2005. Flow around a circular cylinder—structure of the near wake shear layer. Exp. Fluid 38 (4), 393–402. https://doi.org/10.1007/s00348-004-0913-0.

Raman, S.K., Arul Prakash, K., Vengadesan, S., 2013. Effect of axis ratio on fluid flow around an elliptic cylinder-a numerical study. J. Fluid Eng. 135 (11) https://doi.org/10.1115/1.4 024862.

Rao, A., Leontini, J., Thompson, M.C., Hourigan, K., 2013b. Three-dimensionality in the wake of a rotating cylinder in a uniform flow. J. Fluid Mech. 717, 1–29. https://doi.org/10.1017/jfm.2012.542.

Rao, A., Leontini, J.S., Thompson, M.C., Hourigan, K., 2017. Three-dimensionality of elliptical cylinder wakes at low angles of incidence. J. Fluid Mech. 825, 245. https://doi.org/10.1017/jfm.2017 .366.

Rao, A., Thompson, M.C., Leweke, T., Hourigan, K., 2013a. The flow past a circular cylinder translating at different heights above a wall. J. Fluid Struct. 41, 9–21. https://doi.org/10.1016/j.jfluidstructs.2012. 08.007.

Rawat, M.K., 2021. Simulation of turbulent flow with high Reynolds number over an elliptical cylinder. IOP Conference Series: Mater. Sci. Eng. IOP Publ. 1116 (1), 012091 https://doi.org/10.1088/1757-899X/1116/1/012091.

Renouf, D., Gaborko, L., 1982. Speed sensing in a Harbor seal. J. Mar. Biol. Assoc. U. K. 62 (1), 227–228. https://doi.org/10.1017/S0025315400002257.

Rinehart, A., Shyam, V., Zhang, W., 2017. Characterization of seal whisker morphology: implications for whisker-inspired flow control applications. Bioinspiration Biomimetics 12 (6), 066005. https://doi.org/10.1088/1748-3190/aa8885.

Rodríguez, I., Lehmkuhl, O., Chiva, J., Borrell, R., Oliva, A., 2015. On the flow past a circular cylinder from critical to super-critical Reynolds numbers: wake topology and vortex shedding. Int. J. Heat Fluid Flow 55, 91–103. https://doi.org/10.1016/j.ijheatfluidflow.2015.05.009.

Rosetti, G.F., Vaz, G., Fujarra, A.L., 2012. URANS calculations for smooth circular cylinder flow in a wide range of Reynolds numbers: solution verification and validation. J. Fluid Eng. 134 (12) https://doi.org/10.1115/1.4007571.

Roshko, A., 1954. On the Drag and Shedding Frequency of Two-Dimensional Bluff Bodies. California Institute of Technology, Washington, USA.

Ruifeng, H., 2015. Three-dimensional flow past rotating wing at low Reynolds number: a computational study. Fluid Dynam. Res. 47 (4), 045503 https://doi.org/10.1088/0169-5983/47/4/045503.

Saha, A.K., Biswas, G., Muralidhar, K., 2003. Three-dimensional study of flow past a square cylinder at low Reynolds numbers. Int. J. Heat Fluid Flow 24 (1), 54–66. https://doi.org/10.1016/S0142-727X(02)00208-4.

Salvatici, E., Salvetti, M.V., 2003. Large eddy simulations of the flow around a circular cylinder: effects of grid resolution and subgrid scale modeling. Wind Struct. 6 (6), 419–436. https://doi.org/10.12989/was.2003.6.6.419.

Sarkar, S., Sarkar, S., 2009. LES of Flow Past Circular and Elliptic Cylinders in Proximity to a Wall. 6th International Symposium on Turbulence and Shear Flow Phenomena. Begel House Inc.

Sarkar, S., Sarkar, S., 2010. Vortex dynamics of a cylinder wake in proximity to a wall. J. Fluid Struct. 26 (1), 19–40. https://doi.org/10.1016/j.jfluidstructs.2009.08.003.

Sarwar, W., Mellibovsky, F., 2020. Characterization of three-dimensional vortical structures in the wake past a circular cylinder in the transitional regime. Phys. Fluids 32 (7), 074104. https://doi.org/10.1063/5.0011311.

Schewe, G., 1983. On the force fluctuations acting on a circular cylinder in crossflow from subcritical up to transcritical Reynolds numbers. J. Fluid Mech. 133, 265–285. https://doi.org/10.1017/S002 2112083001913.

Schewe, G., 2001. Reynolds-number effects in flow around more-or-less bluff bodies. J. Wind Eng. Ind. Aerod. 89 (14–15), 1267–1289. https://doi.org/10.1016/S0167-6105(01) 00158-1.

Schulte-Pelkum, N., Wieskotten, S., Hanke, W., Dehnhardt, G., Mauck, B., 2007. Tracking of biogenic hydrodynamic trails in Harbor seals (Phoca vitulina). J. Exp. Biol. 210 (5), 781–787. https://doi.org/10.1242/jeb.02708.

Sen, S., Mittal, S., 2017. A study on the far wake of elliptic cylinders. Comput. Model. Eng. Sci. 113 (1), 35–55.

Sen, S., Mittal, S., Biswas, G., 2012. Steady separated flow past elliptic cylinders using a stabilized finite-element method. Comput. Model. Eng. Sci. 86 (1), 1.

Seyed-Aghazadeh, B., Modarres-Sadeghi, Y., 2015. An experimental investigation of vortex-induced vibration of a rotating circular cylinder in the crossflow direction. Phys. Fluids 27 (6), 067101. https://doi.org/10.1063/1.4921683.

Sheard, G.J., Thompson, M.C., Hourigan, K., 2003. A coupled Landau model describing the Strouhal–Reynolds number profile of a three-dimensional circular cylinder wake. Phys. Fluids 15, L68–L71. https://doi.org/10.1063/1.1597471.

Shi, X., Alam, M., Bai, H., 2020. Wakes of elliptical cylinders at low Reynolds number. Int. J. Heat Fluid Flow 82, 108553. https://doi.org/10.1016/j.ijheatfluidflow.2020.108553.

Shih, W.C.L., Wang, C., Coles, D., Roshko, A., 1993. Experiments on flow past rough circular cylinders at large Reynolds numbers. J. Wind Eng. Ind. Aerod. 49 (1–3), 351–368. https://doi.org/10.1016/0167-6105(93)90030-R.

Shu, C., Wang, Y., Teo, C.J., Wu, J., 2014. Development of lattice Boltzmann flux solver for simulation of incompressible flows. Adv. Appl. Math. Mech. 6 (4), 436–460. https://doi.org/10.4208/aamm.2014.4.s2.

Skillen, A., Revell, A., Pinelli, A., Piomelli, U., Favier, J., 2015. Flow over a wing with leading-edge undulations. AIAA J. 53 (2), 464–472. https://doi.org/10.2514/1.J053142.

Son, J.S., Hanratty, T.J., 1969. Velocity gradients at the wall for flow around a cylinder at Reynolds numbers from 5×10^3 to 10^5. J. Fluid Mech. 35 (2), 353–368. https://doi.org/10.1017/S002211 2069001157.

Sooraj, P., Agrawal, A., Sharma, A., 2018. Measurement of drag coefficient for an elliptical cylinder. J. Energy Environ. Sustain. 5, 1–7.

Soumya, S., Prakash, K.A., 2017. Effect of splitter plate on passive control and drag reduction for fluid flow past an elliptic cylinder. Ocean Eng. 141, 351–374. https://doi.org/10.1016/j.oceaneng. 2017.06.034.

Sourav, K., Sen, S., 2017. On the response of a freely vibrating thick elliptic cylinder of low mass ratio. J. Appl. Fluid Mech. 10 (3), 899–913.

Stojković, D., Breuer, M., Durst, F., 2002. Effect of high rotation rates on the laminar flow around a circular cylinder. Phys. Fluids 14 (9), 3160–3178. https://doi.org/10.1063/1.1492811.

Stringer, R.M., Zang, J., Hillis, A.J., 2014. Unsteady RANS computations of flow around a circular cylinder for a wide range of Reynolds numbers. Ocean Eng. 87, 1–9. https://doi.org/10.1016/j.oceaneng.2014.04 .017.

Subburaj, R., Khandelwal, P., Vengadesan, S., 2018. Numerical study of flow past an elliptic cylinder near a free surface. Phys. Fluids 30 (10), 103603. https://doi.org/10.1063/1.5046745.

Sumner, D., 2010. Two circular cylinders in cross-flow: a review. J. Fluid Struct. 26 (6), 849–899. https://doi.org/10.1016/j.jfluidstructs.2010.07.001.

Sumner, D., Akosile, O.O., 2003. On uniform planar shear flow around a circular cylinder at subcritical Reynolds number. J. Fluid Struct. 18 (3–4), 441–454. https://doi.org/10.1016/j.jfluidstructs.2003. 08.004.

Sun, R., Chwang, A.T., 1999. Interaction between rotating elliptic cylinder and fixed circular cylinder. J. Eng. Mech. 125 (7), 761–767. https://doi.org/10.1061/(ASCE)0733-9399(1999)125:7(761).

Szepessy, S., Bearman, P.W., 1992. Aspect ratio and end plate effects on vortex shedding from a circular cylinder. J. Fluid Mech. 234, 191–217. https://doi.org/10.1017/S0022112092000752.

Tham, D.M.Y., Gurugubelli, P.S., Li, Z., Jaiman, R.K., 2015. Freely vibrating circular cylinder in the vicinity of a stationary wall. J. Fluid Struct. 59, 103–128. https://doi.org/10.1016/j.jfluidstructs. 2015.09.003.

Thom, A., 1933. The flow past circular cylinders at low speeds. Proc. R. Soc. Lond. - Ser. A Contain. Pap. a Math. Phys. Character 141 (845), 651–669. https://doi.org/10.1098/rspa.1933.0146.

Thompson, M.C., Radi, A., Rao, A., Sheridan, J., Hourigan, K., 2014. Low-Reynolds-number wakes of elliptical cylinders: from the circular cylinder to the normal flat plate. J. Fluid Mech. 751, 570–600. https://doi.org/10.1017/jfm.2014.314.

Tian, G., Xiao, Z., 2020. New insight on large-eddy simulation of flow past a circular cylinder at subcritical Reynolds number 3900. AIP Adv. 10 (8), 085321 https://doi.org/10.1063/5.0012358.

Travin, A., Shur, M., Strelets, M., Spalart, P., 2000. Detached-eddy simulations past a circular cylinder. Flow, Turbul. Combust. 63 (1), 293–313. https://doi.org/10.1023/A:1009901401183.

Triantafyllou, M.S., Weymouth, G.D., Miao, J., 2016. Biomimetic survival hydrodynamics and flow sensing. Annu. Rev. Fluid Mech. 48, 1–24. https://doi.org/10.1146/annurev-fluid-122414-034329.

Tritton, D.J., 1959. Experiments on the flow past a circular cylinder at low Reynolds numbers. J. Fluid Mech. 6 (4), 547–567. https://doi.org/10.1017/S0022112059000829.

Verma, A., Mittal, S., 2011. A new unstable mode in the wake of a circular cylinder. Phys. Fluids 23 (12), 121701. https://doi.org/10.1063/1.3664869.

Vijay, K., Srinil, N., Zhu, H., Bao, Y., Zhou, D., Han, Z., 2020. Flow-induced transverse vibration of an elliptical cylinder with different aspect ratios. Ocean Eng. 214, 107831. https://doi.org/10.1016/j.oceaneng.2020.107831.

Wan, H., DesRoches, J.A., Palazotto, A.N., Patnaik, S.S., 2021. Vortex-induced vibration of elliptic cylinders and the suppression using mixed-convection. J. Fluid Struct. 103, 103297. https://doi.org/10.1016/j.jfluidstructs.2021.103297.

Wang, G., Tian, Y., Kinnas, S.A., 2018a. Particle image velocimetry experiment and computational fluid dynamics simulation of flow around rigid cylinder. J. Offshore Mech. Arctic Eng. 140 (5) https://doi.org/10.1115/1.4039948.

Wang, H., Zhai, Q., Chen, K., 2019a. Vortex-induced vibrations of an elliptic cylinder with both transverse and rotational degrees of freedom. J. Fluid Struct. 84, 36–55. https://doi.org/10.1016/j.jfluidstructs.2018.10.004.

Wang, R., Bao, Y., Zhou, D., Zhu, H., Ping, H., Han, Z., Serson, D., Xu, H., 2019b. Flow instabilities in the wake of a circular cylinder with parallel dual splitter plates attached. J. Fluid Mech. 874, 299–338. https://doi.org/10.1017/jfm.2019.439.

Wang, J., Zheng, H., Tian, Z., 2015. Numerical simulation with a TVD–FVM method for circular cylinder wake control by a fairing. J. Fluid Struct. 57, 15–31. https://doi.org/10.1016/j.jfluidstructs .2015.05.008.

Wang, J.S., Fan, D., Lin, K., 2020. A review on flow-induced vibration of offshore circular cylinders. J. Hydrodyn. 32 (3), 415–440. https://doi.org/10.1007/s42241-020-0032-2.

Wang, L., Guo, C., Su, Y., 2018b. Numerical analysis of flow past an elliptic cylinder near a moving wall. Ocean Eng. 169, 253–269. https://doi.org/10.1016/j.oceaneng.2018.09.033.

Wang, S., Liu, Y., 2016. Wake dynamics behind a seal-vibrissa-shaped cylinder: a comparative study by time-resolved particle velocimetry measurements. Exp. Fluid 57 (3), 32. https://doi.org/10.1007/s00348-016-2117-9.

Wang, X.K., Hao, Z., Tan, S.K., 2013. Vortex-induced vibrations of a neutrally buoyant circular cylinder near a plane wall. J. Fluid Struct. 39, 188–204. https://doi.org/10.1016/j.jfluidstructs. 2013.02.012.

Wang, X.K., Tan, S.K., 2008. Comparison of flow patterns in the near wake of a circular cylinder and a square cylinder placed near a plane wall. Ocean Eng. 35 (5–6), 458–472. https://doi.org/10.1016/j. oceaneng.2008.01.005.

Wei, D.J., Yoon, H.S., Jung, J.H., 2016. Characteristics of aerodynamic forces exerted on a twisted cylinder at a low Reynolds number of 100. Comput. Fluid 136, 456–466. https://doi.org/10.1016/j .compfluid. 2016.07.002.

Wei, Z., New, T.H., Cui, Y.D., 2015. An experimental study on flow separation control of hydrofoils with leading-edge tubercles at low Reynolds number. Ocean Eng. 108, 336–349. https://doi.org/10.1016/j.oceaneng.2015.08.004.

Wen, P., Qiu, W., 2017. Investigation of drag crisis phenomenon using CFD methods. Appl. Ocean Res. 67, 306–321. https://doi.org/10.1016/j.apor.2017.07.012.

West, G.S., Apelt, C.J., 1993. Measurements of fluctuating pressures and forces on a circular cylinder in the Reynolds number range 104 to 2.5×105. J. Fluid Struct. 7 (3), 227–244. https://doi.org/10.1006/jfls.1993.1014.

Witte, M., Hanke, W., Wieskotten, S., Miersch, L., Brede, M., Dehnhardt, G., Leder, A., 2012. On the Wake Flow Dynamics behind Harbor Seal Vibrissae–A Fluid Mechanical Explanation for an Extraordinary Capability. Nature-Inspired Fluid Mechanics. Springer, Berlin, Heidelberg, pp. 271–289. https://doi.org/10.1007/978-3-642-28302-4_17.

Williamson, C.H.K., 1988. The existence of two stages in the transition to three-dimensionality of a cylinder wake. Phys. Fluids 31, 3165–3168. https://doi.org/10.1063/1.866925.

Williamson, C.H.K., 1989. Oblique and parallel modes of vortex shedding in the wake of a circular cylinder at low Reynolds numbers. J. Fluid Mech. 206, 579–627. https://doi.org/10.1017/S0022112089002429.

Williamson, C.H.K., 1996a. Vortex dynamics in the cylinder wake. Annu. Rev. Fluid Mech. 28 (1), 477–539. https://doi.org/10.1146/annurev.fl.28.010196.002401.

Williamson, C.H.K., 1996b. Three-dimensional wake transition. J. Fluid Mech. 328, 345–407. https://doi.org/10.1017/S0022112096008750.

Williamson, C.H.K., Roshko, A., 1988. Vortex formation in the wake of an oscillating cylinder. J. Fluid Struct. 2 (4), 355–381. https://doi.org/10.1016/S0889-9746(88)90058-8.

Wissink, J.G., Rodi, W., 2008. Numerical study of the near wake of a circular cylinder. Int. J. Heat Fluid Flow 29 (4), 1060–1070. https://doi.org/10.1016/j.ijheatfluidflow.2008.04.001.

Wong, E.W.C., Kim, D.K., 2018. A simplified method to predict fatigue damage of TTR subjected to short-term VIV using artificial neural network. Adv. Eng. Software 126, 100–109. https://doi.org/10.1016/j.advengsoft.2018.09.011.

Wong, K.W.L., Zhao, J., Jacono, D.L., Thompson, M.C., Sheridan, J., 2017. Experimental investigation of flow-induced vibration of a rotating circular cylinder. J. Fluid Mech. 829, 486–511. https://doi.org/10.1017/jfm.2017.540.

Wornom, S., Ouvrard, H., Salvetti, M.V., Koobus, B., Dervieux, A., 2011. Variational multiscale large-eddy simulations of the flow past a circular cylinder: Reynolds number effects. Comput. Fluid 47 (1), 44–50. https://doi.org/10.1016/j.compfluid.2011.02.011.

Wu, M.H., Wen, C.Y., Yen, R.H., Weng, M.C., Wang, A.B., 2004. Experimental and numerical study of the separation angle for flow around a circular cylinder at low Reynolds number. J. Fluid Mech. 515, 233. https://doi.org/10.1017/S0022112004000436.

Wu, T.Y., 2011. Fish swimming and bird/insect flight. Annu. Rev. Fluid Mech. 43, 25–58. https://doi.org/10.1146/annurev-fluid-122109-160648.

Wu, X., Ge, F., Hong, Y., 2012. A review of recent studies on vortex-induced vibrations of long slender cylinders. J. Fluid Struct. 28, 292–308. https://doi.org/10.1016/j.jfluidstructs.2011. 11.010.

Wu, X., Li, Y., Zhou, S., 2021. Flow-induced vibration on isolated and tandem elliptic cylinders with varying reduced velocities: a lattice Boltzmann flux solver study with immersed boundary method. Eur. J. Mech. B Fluid 89, 45–63. https://doi.org/10.1016/j. euromechflu.2021. 04.012.

Xu, C.Y., Chen, L.W., Lu, X.Y., 2007. Large-eddy and detached-eddy simulations of the separated flow around a circular cylinder. J. Hydrodyn. 19 (5), 559–563. https://doi.org/10.1016/S1001-6058(07)60153-X.

Xu, C.Y., Chen, L.W., Lu, X.Y., 2010. Large-eddy simulation of the compressible flow past a wavy cylinder. J. Fluid Mech. 665 (1), 238–273. https://doi.org/10.1017/S0022112010000927.

Xu, S.J., Zhang, W.G., Gan, L., Li, M.G., Zhou, Y., 2017. Experimental study of flow around polygonal cylinders. J. Fluid Mech. 812, 251–278. https://doi.org/10.1017/jfm.2016.801.

Yang, F., An, H., Cheng, L., 2018. Drag crisis of a circular cylinder near a plane boundary. Ocean Eng. 154, 133–142. https://doi.org/10.1016/j.oceaneng.2018.01.011.

Yazdi, M.J.E., Khoshnevis, A.B., 2018. Wake-boundary layer interaction behind an elliptic cylinder at different Reynolds numbers. J. Turbul. 19 (7), 529–552. https://doi.org/10.1080/14685248. 2018. 1472 382.

Yazdi, M.J.E., Khoshnevis, A.B., 2020. A Comparing the wake behind circular and elliptical cylinders in a uniform current. SN Appl. Sci. 2 (5), 1–13. https://doi.org/10.1007/s42452-020-2698-z.

Ye, H., Wan, D., 2017. Benchmark computations for flows around a stationary cylinder with high Reynolds numbers by RANS-overset grid approach. Appl. Ocean Res. 65, 315–326. https://doi.org/10.1016/j.apor.2016.10.010.

Yeon, S.M., Yang, J., Stern, F., 2016. Large-eddy simulation of the flow past a circular cylinder at sub-to super-critical Reynolds numbers. Appl. Ocean Res. 59, 663–675. https://doi.org/10.1016/j.apor.2015.11. 013.

Yogeswaran, V., Sen, S., Mittal, S., 2014. Free vibrations of an elliptic cylinder at low Reynolds numbers. J. Fluid Struct. 51, 55–67. https://doi.org/10.1016/j.jfluidstructs .2014.07. 012.

Yokuda, S., Ramaprian, B.R., 1990. The dynamics of flow around a cylinder at subcritical Reynolds numbers. Phys. Fluid. Fluid Dynam. 2 (5), 784–791. https://doi.org/10.1063/1.857732.

Yoon, H.S., Kim, H.J., Wei, D.J., 2018. Forced convection heat transfer from the helically twisted elliptic cylinder inspired by a daffodil stem. Int. J. Heat Mass Tran. 119, 105–116. https://doi.org/10.1016/j.ijheatmasstransfer.2017.11.107.

Yoon, H.S., Kim, M.I., Kim, H.J., 2019. Reynolds number effects on the flow over a twisted cylinder. Phys. Fluids 31 (2), 025119. https://doi.org/10.1063/1.5079913.

Yoon, H.S., Lee, J.B., Seo, J.H., Park, H.S., 2010. Characteristics for flow and heat transfer around a circular cylinder near a moving wall in wide range of low Reynolds number. Int. J. Heat Mass Tran. 53 (23–24), 5111–5120. https://doi.org/10.1016/j.ijheatmasstransfer.2010.07.054.

Yoon, H.S., Moon, J., 2021. Effect of variable pitch on forced convection heat transfer around a helically twisted elliptic cylinder. Int. J. Heat Mass Tran. 173, 121205. https://doi.org/10.1016/j.ijheatmasstransfer.2021.121205.

Yoon, H.S., Oh, K.J., Kim, H.J., Kim, M.I., Moon, J., 2020. Double wavy geometric disturbance to the bluff body flow at a subcritical Reynolds number. Ocean Eng. 195, 106713. https://doi.org/10.1016/j.oceaneng.2019.106713.

Yoon, H.S., Shin, H., Kim, H., 2017. Asymmetric disturbance effect on the flow over a wavy cylinder at a subcritical Reynolds number. Phys. Fluids 29 (9), 095102. https://doi.org/10.1063/1.5001968.

Yoon, H.S., Yin, J., Choi, C., Balachandar, S., Ha, M.Y., 2016. Bifurcation of laminar flow around an elliptic cylinder at incidence for low Reynolds numbers. Prog. Comput. Fluid Dyn. Int. J. 16 (3), 163–178. https://doi.org/10.1504/PCFD.2016.076235.

Zdravkovich, M.M., 1981. Review and classification of various aerodynamic and hydrodynamic means for suppressing vortex shedding. J. Wind Eng. Ind. Aerod. 7 (2), 145–189. https://doi.org/10.1016/0167-6105(81)90036-2.

Zdravkovich, M.M., 1990. Conceptual overview of laminar and turbulent flows past smooth and rough circular cylinders. J. Wind Eng. Ind. Aerod. 33 (1–2), 53–62. https://doi.org/10.1016/0167-6105(90)90020-D.

Zhai, H., Wang, Z., Li, Q., 2018. Numerical investigation of laminar separation in flow across elliptic cylinders. IOP Conference Series: Mater. Sci. Eng. IOP Publ. 452 (4), 042037 https://doi.org/10.1088/1757-899X/452/4/042037.

Zhang, H., Shi, W., 2016. Numerical simulation of flow over a circular cylinder with a splitter plate near a moving wall. Ocean Eng. 122, 162–171. https://doi.org/10.1016/j.oceaneng.2016.06.026.

Zhang, W., Dai, C., Lee, S.J., 2005. PIV measurements of the near-wake behind a sinusoidal cylinder. Exp. Fluid 38, 824–832. https://doi.org/10.1007/s00348-005-0981-9.

Zhang, Z., Ji, C., Chen, W., Hua, Y., Srinil, N., 2021. Influence of boundary layer thickness and gap ratios on three-dimensional flow characteristics around a circular cylinder in proximity to a bottom plane. Ocean Eng. 226, 108858. https://doi.org/10.1016/j.oceaneng.2021.108858.

Zhao, J., Hourigan, K., Thompson, M.C., 2019. Dynamic response of elliptical cylinders undergoing transverse flow-induced vibration. J. Fluid Struct. 89, 123–131. https://doi.org/10.1016/j.jfluidstructs.2019.01.011.

Zhao, M., 2020. Flow-induced by an oscillating circular cylinder close to a plane boundary in quiescent fluid. J. Fluid Mech. 897 https://doi.org/10.1017/jfm.2020.355.

Zhao, M., Cheng, L., 2011. Numerical simulation of two-degree-of-freedom vortex-induced vibration of a circular cylinder close to a plane boundary. J. Fluid Struct. 27 (7), 1097–1110. https://doi.org/10.1016/j.jfluidstructs.2011.07.001.

Zhao, M., Cheng, L., 2014. Vortex-induced vibration of a circular cylinder of finite length. Phys. Fluids 26 (1), 015111. https://doi.org/10.1063/1.4862548.

Zhao, M., Cheng, L., Lu, L., 2014. Vortex induced vibrations of a rotating circular cylinder at low Reynolds number. Phys. Fluids 26 (7), 073602. https://doi.org/10.1063/1.4886196.

Zheng, H., Wang, J., 2021. A numerical study on the flow-induced vibrations of flexible cylinders attached with fixed short fairings. Ocean Eng. 229, 108904. https://doi.org/10.1016/j.oceaneng.2021.108904.

Zhou, J., Qiu, X., Li, J., Liu, Y., 2021. The gap ratio effects on vortex evolution behind a circular cylinder placed near a wall. Phys. Fluids 33 (3), 037112. https://doi.org/10.1063/5.0039611.

Zhu, J., Holmedal, L.E., Myrhaug, D., Wang, H., 2020. Near-wall effect on flow around an elliptic cylinder translating above a plane wall. Phys. Fluids 32 (9), 093607. https://doi.org/10.1063/5.0020818.

Zhu, J., Jiang, F., Holmedal, L.E., 2021. Three-dimensional wake transition behind an elliptic cylinder near a moving wall. Phys. Fluids 33 (4), 043606. https://doi.org/10.1063/5.0048219.